Politecnico di Milano
Department of Energy
Doctoral Programme in
Energy and Nuclear Science and Technology

Experimental and theoretical studies on ultraintense laser-driven ion acceleration

Doctoral Dissertation of:
Alessandro Zani

Supervisor:
Dr. Matteo Passoni

Tutor:
Prof. Stefano L. M. Giulini Castiglioni Agosteo

The Chair of the Doctoral Program:
Prof. Carlo E. Bottani

Year 2013 – Cycle XXV

Science is organized knowledge.
Wisdom is organized life.
— Immanuel Kant

To my parents

Abstract

Since the discovery of CPA, allowing the production of ultraintense and ultrashort laser pulses, the quest for new regimes of laser-matter interaction led to the observation of several intriguing phenomena including the emission of radiation and the acceleration of particles. The latter in particular allowed to produce ion bunches to multi-MeV energies owning very peculiar properties, which can be exploited for a number of possible applications in radiotherapy, advanced diagnostics and inertial confinement nuclear fusion. Every application of laser accelerated ions requires the optimization of one or more beam parameter. To optimize a quantity a general procedure would be to get a fundamental theoretical understanding of the system, combined with novel experimental approaches. In this PhD work we focus the attention on the optimization of one of the beam parameters, that is to say the maximum energy an ion can gain in the acceleration process. The goal is achieved by a two-steps methodology: first a theoretical study of maximum proton energy dependencies on laser properties has been performed. The second part of the project has dealt with an experimental activity aimed to improve laser-driven ion acceleration in a smarter fashion, i.e. not by demanding further laser performances but by properly engineering the target properties at the nanoscale. To this end the production, characterization and testing of innovative targets for ion acceleration has been carried on.

Premessa

Dall' invenzione della tecnica CPA per la produzione di impulsi laser ultraintensi e ultrabrevi, è stato possibile investigare nuovi regimi di interazione laser-materia che hanno portato alla scoperta di fenomeni di estremo interesse come l'emissione di radiazione elettromagnetica e l'accelerazione di particelle cariche. In particolare, quest'ultima ha consentito di produrre fasci di ioni con energie di decine di MeV e diverse proprietà molto peculiari, che hanno portato a studi per il loro utilizzo in applicazioni di interesse per la radioterapia, sistemi diagnostici avanzati e fusione nucleare a confinamento inerziale. Ciascune di queste applicazioni richiede l'ottimizzazione di uno o più parametri caratteristici del fascio di ioni. In generale l'ottimizzazione di una quantità richiede una conoscenza teorica approfondita del sistema in analisi combinata con approcci sperimentali innovativi. In questo lavoro di Dottorato si è rivolta l'attenzione sull'ottimizzazione di uno dei parametri che descrivono il fascio di ioni accelerati, ovvero la loro energia massima. Per raggiungere l'obiettivo è stata adottata una metodologia a due stadi: il primo ha portato ad uno studio teorico delle dipendenze dell'energia massima degli ioni dai parametri del sistema laser. Nella seconda parte del progetto è stato svolto un'attività sperimentale dedita all'ottimizzazione del processo di accelerazione di ioni non attraverso il miglioramento delle prestazioni del sistema laser, ma tramite l'ingegnerizzazione alla nanoscala delle proprietà del bersaglio. A tal scopo è stata condotta la produzione, caratterizzazione e test su laser facility dei target innovativi prodotti.

Contents

Abstract (English/Italian) **i**

Introduction **1**

I Laser-ion acceleration: experimental and theoretical state of the art **11**

1 Interaction of intense radiation with matter **13**
1.1 Plasma characteristics 13
1.2 Ionization mechanisms 16
1.3 Laser-plasma interaction 19
1.3.1 Underdense plasmas 21
1.3.2 Overdense plasmas 25

2 Ion acceleration driven by intense laser pulses **31**
2.1 Characteristics of ion emission 32
2.1.1 Dependence on laser properties 35
2.1.2 Dependence on target properties 37
2.2 Acceleration mechanisms 38
2.2.1 Target Normal Sheath Acceleration (TNSA) . . . 38
2.2.2 Radiation Pressure Acceleration (RPA) 40

II Theoretical modeling of Target Normal Sheath Acceleration **43**

3 Comparison among Target Normal Sheath Acceleration theoretical models **45**
3.1 TNSA analytical modeling 46
3.1.1 General approach to TNSA modeling 46
3.1.2 Fluid models 50
3.1.3 Quasi-static models 52
3.1.4 Hybrid models 53
3.2 Quantitative comparison 55
3.2.1 Assessment of the parameters needed in the models 55
3.2.2 Assessment of the experimental database 56
3.2.3 Results and discussion 57

4 Quasi-static modeling of Target Normal Sheath Acceleration **61**
4.1 The exact relativistic solution of Passoni-Lontano model 62
4.2 TNSA scalings: theoretical interpretation of experimental and numerical data 66
4.2.1 Comparison with experiments 67
4.2.2 Comparison with Particle-In-Cell simulations . . . 70

III Nanoengineered targets for laser-driven ion acceleration **75**

5 Towards enhanced laser-driven ion acceleration **77**
5.1 Ion acceleration in the near-critical regime 78
5.2 Ion acceleration with foam-attached targets 81

6 Production of foam-attached targets **89**
6.1 From nanoporous materials to foams 90
6.2 Nuclear-based density measurement techniques 91
6.2.1 Rutherford Backscattering Spectroscopy (RBS) . . 92
6.2.2 Nuclear Reaction Analysis (NRA) 93
6.3 Methods to produce foam-attached targets for laser-ion acceleration 94
6.3.1 Production of foams by Pulsed Laser Deposition . 94
6.3.2 Quartz-Crystal Microbalance (QCM) 95
6.3.3 Energy Dispersive X-ray Spectroscopy (EDSX) . . 97

7 Characterization of foam-attached targets **101**
7.1 Process parameters for foam production 101
7.2 Results of carbon foams characterizations 102
7.2.1 Carbon foam structural properties 102
7.2.2 Carbon foam morphology 104
7.2.3 Carbon foam density measurements 111
7.3 Foam-attached target assembling 113

8 Test of foam-attached targets for laser-driven ion acceleration **117**
8.1 Experimental setup 117
8.2 Ion acceleration results 119
8.3 Preliminary interpretation of experimental results 122

9 Conclusions and perspectives **125**

A Experimental **129**
A.1 foams production and characterization 129
A.1.1 Pulsed Laser Deposition (PLD) 129
A.1.2 Quartz Crystal Microbalance (QCM) 133
A.1.3 Scanning Electron Microscopy (SEM) and Energy Dispersive X-ray Spectrometer (EDXS) 134
A.1.4 Raman spectroscopy 137
A.2 Ion acceleration using foam attached targets 139
A.2.1 The UHI100 laser facility 139
A.2.2 Diagnostic systems 141

Bibliography **160**

Introduction

Since the first conception of the laser in 1960 [1], investigation of light-matter interactions has become a challenging and increasing field of research. During the decades following this extraordinary result, the intensity regime being explored has got broader, owing to the enormous advances in laser technology. Continuous wave operation has been soon overcome by the introduction of new techniques, such as Q-switching [2] and mode-locking [3], which allowed to store the laser energy in short pulses, having durations from nanoseconds down to tens of femtoseconds with present-day large bandwidth gain materials. During the 1970s an upper limit of focussed intensity seemed to be reached, since in order to gain more amplification volume, laser beams with increasing diameter were required not to overcome the damage threshold of active media. Systems having such huge dimensions were accessible only by few military facilities, hence limiting the scientific research in this direction. After the invention of chirped pulse amplification (CPA) in 1985 by Strickland and Mourou [4], the "spatial stretching" of the laser pulse prior to the amplification phase has been replaced by a temporal stretching, making it possible to introduce nowadays compact Terawatt to Petawatt class laser systems which have become commercially available since a couple of years [5,6]. The ultrahigh intensity regime of laser-matter interaction has become then accessible by many laboratories all around the world. The laser pulses are delivered with durations between few picoseconds and few femtoseconds, energies from mJ to kJ, powers from 1 TW to few PW,

focalized over μm^2 areas, giving power densities on target (or intensities) in excess of 10^{18} W/cm^2: the associated laser electric fields are such ($> 10^{10}$ V/m) that an electron can gain under its action relativistic energies. When such a laser pulse interacts with matter, an almost complete ionization of the medium takes place already during the first laser cycles, giving rise to a relativistic and nonlinear plasma interacting with the rest of the pulse. Several unconventional physical processes, known as laser-plasma "secondary sources", have been experimentally observed as a consequence of the interaction process. Among all a vivid interest has arisen mostly around particle acceleration (electrons and ion) and the generation of X radiation. The quest for efficient coherent short-wavelength radiation sources, for their use mainly in biology, plasma diagnostics, medicine and photolitography, has found in laser generated high-order harmonics a very accessible and low expensive road if compared to the traditional ones, i.e. X-ray lasers and free-electron lasers. The process of high-harmonic generation (HHG) from femtosecond laser pulses allows to generate radiation in the extreme ultraviolet spectral range (wavelength 1-100 nm), due to a strong high-order nonlinear optical response of the laser generated plasma in the high intensity regime [7, 8].

The acceleration of particles from laser-created plasmas, represents one of the prime interests in this fields. In 1979 Tajima and Dawson [9] first proposed to accelerate electrons using the relativistic plasma waves created in the wake of an intense laser pulse passing through the medium [10]. Electrons in the laser wakefield are directly accelerated to relativistic energies at intensities $> 10^{18}$ W/cm^2. During the years prior to 2004 laser-plasma accelerator experiments have demonstrated [11–13] accelerating fields > 100 GV/m, giving rise to electron bunches having broad exponential energy distributions with long tails which extended out to high energies (> 100 MeV). After 2004, as a result of an improved control of laser and plasma parameters, diagnostic techniques and comprehension of the underlying physics, some groups reported the acceleration of electron bunches characterized by a significant charge > 100 pC, high mean energy (~ 100 MeV), low divergence (few milliradians) and very small energy spread down to few percent [14–16]. Nowadays high quality electron bunches with mean energies up to 1 GeV can be accelerated over distances of 3.3 cm, by exploiting a plasma-channel-guided laser [17]. In order to drive a relativistic proton dynamics in the wake of a laser pulse, a larger laser intensity should be delivered, at least in excess of 10^{24} W/cm^2. At

such intensities light-matter interaction would have to take into account also radiation reaction-effects and the creation of particles and anti-particles in the laser field [18]. Present laser technology allows to reach peak intensities up to 10^{22} W/cm^2, so that laser energy cannot be transferred directly to protons, but the electrons act as a mediator [19]. In fact once the laser pulse impinge onto the target, electrons efficiently absorb electromagnetic field energy and expand, setting up a strong charge separation. The huge electric fields that follow charge separation might be felt by heavier particles, being then accelerated (see illustrative picture in Fig. 1(a)). This mechanism is known as Target Normal Sheath Acceleration (TNSA) and represents the most commonly observed ion acceleration process in the experiments carried on so far, where mainly solid density foils were used as targets, with thicknesses ranging from few tens of nanometers to few tens of microns for linearly polarized pulses ranging in intensity from 10^{18} to 10^{21} W/cm^2. Here, the first cycles of the pulse create a blow-off plasma (so-called "pre-plasma") where part of the total pulse energy is transferred to a population of target electrons via some collisionless absorption mechanisms, giving them an average energy of the order of MeV. These electrons are able to travel through the target reaching the non-irradiated side and, expanding in vacuum for a Debye length (order of μm for these energies), they set up a longitudinal electric field of the order of MV/μm. This field is maximum around the solid-vacuum interface: hence it promptly ionizes and accelerates the hydrocarbon and H_2O contaminants located on the surface (see a schematic picture of TNSA in Fig. 1(b)). Protons, being the particles with the most favorable charge-to-mass ratio, gain most of the field energy while heavier ions feel a reduced accelerating voltage. It has been demon-

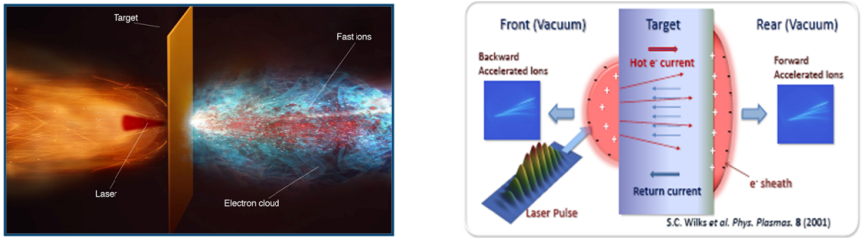

(a) (b)

Figure 1: *Illustrative pictures describing TNSA mechanism for laser-driven ion acceleration.*

strated that a removal of hydrogen from the rear surface is needed in order to accelerate heavier ions [20–22]. The typical recorded proton spectra are continuous and exponentially distributed with a cut-off energy. A TNSA quasi-monoenergetic spectrum has been demonstrated by reducing in size the "ion source" on the non irradiated surface to the area where the sheath field is homogeneous [20, 23]. So far the highest maximum proton energies ever obtained are around 60 MeV and have been obtained exploiting picosecond duration petawatt laser systems [24]. Moreover recent results have reported 40 MeV protons obtained exploiting the same intensity value $\sim 10^{21}$ W/cm^2 but with a femtosecond 200 TW laser pulse [25]. Apart from spectral properties, a laser-accelerated proton bunch has been observed to own high beam quality thanks to small transverse and longitudinal emittance, < 0.004 mm^{2}mrad and $< 10^{-4}$ eVs, respectively [26].

Laser-accelerated ion beams are being examined in the light of several possible applications. One of the most intuitive implementations regards the employment of such sources in proton radiography, a diagnostic technique which exploits a proton beam as a tool to probe density gradients and electromagnetic fields in extreme systems [27, 28]. Thanks to the beam properties, showing a micron source size and picosecond bunch duration, laser-plasma proton radiography is found to own a high spatial and time resolution [29]. Moreover, a broad TNSA

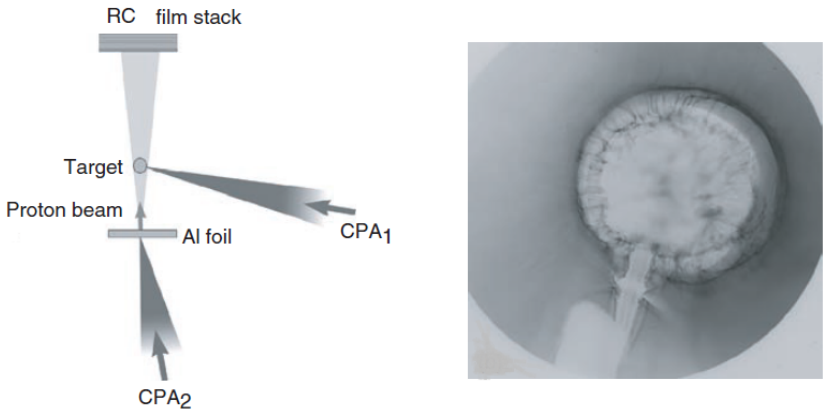

(a) Set-up for proton imaging of ultraintense interactions.

(b) Proton image taken with $E_p \sim$ 6-7 MeV and $\Delta t \sim$10 ps.

Figure 2: *Proton radiography of a 150μm glass micro-balloon after CPA irradiation [27].*

spectrum is in this sense very useful, since protons with different energies (i.e. velocities) are able to probe a dynamic system at different instants: a time-resolved series of images can then be achieved. Various ultrafast phenomena in laser plasma interactions have been investigated (see for example Fig. 2): the sheath fields responsible for TNSA ion acceleration [29], the dynamics of electromagnetic structures in the wake of ultraintense laser pulses propagating through a medium [30,31] and the propagation of laser-excited collisionless shocks in a low-density plasma [32].
A second important application for laser-accelerated ion bunches regards their employment in inertial confinement nuclear fusion (ICF). The first condition for a mixture of deuterium and tritium (DT) to undergo fusion reactions is a constraint on its temperature, which is forced to exceed 10 keV. The second condition is the Lawson criterion [33], which can in principle be realized in two complementary ways: to confine either a low density plasma ($n_e \sim 10^{15}$ cm^{-3}) for a rather long time ($\tau \sim 1$ s) or a high density plasma ($n_e \sim 10^{26}$ cm^{-3}) in nanosecond duration lapse of time. The former approach is achieved using tokamaks to confine magnetically the thermonuclear plasma, the latter only exploits the fuel inertia for the confinement of a compressed target. The compression is achieved by means of radiation pressure either directly or indirectly propelled by laser pulses. The direct compression is obtained by focussing many laser pulses onto the fuel pellet surface, driving a spherically symmetrical implosion, while the indirect approach exploits the X-rays generated by the walls of an hohlraum containing the DT pellet [34] when multiple laser pulses hit its internal walls. Therefore in both indirect and direct approaches, the compression and heating phases are achieved at the same time by the multiple laser pulses, giving rise to several hydrodynamic instabilities while the ablation pressure compresses the pellet. A possible trick to overcome this limitation is to separate compression and heating processes by compressing the fuel while it is still at low temperature and employing a particle beam to heat and ignite it at the moment of maximum compression [36]: this approach is known as fast-ignition scheme (FI-ICF). So far mostly electrons have been exploited for this goal, but recently the idea to make use of ions has been proposed to more efficiently deposit their energy in the pellet [35, 37, 38] (see the process illustration in Fig. 3(a)). In fact ion stopping power in matter shows for a quasi-monoenergetic bunch a favorable energy-dose distribution (see simulation results in Fig. 3(b)), allowing for a very localized energy

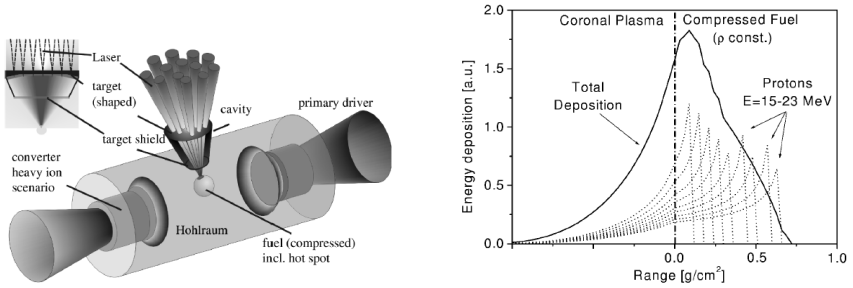

(a) Schematic view of indirectly driven fast ignition using a laser accelerated proton beam.

(b) Simulation of proton energy deposition in a compressed fuel pellet.

Figure 3: *Fast ignition using laser generated proton beams [35].*

deposit (Bragg peak) just before being stopped. For this reason ion bunches are good candidates to be exploited in the fast-ignitor scheme, but there are severe constraints such as the high laser-to-ion conversion efficiency that limited so far the test of TNSA accelerated ions.
Finally, a third widely studied application lies in ion beam therapy for tumors (IBT). During the last decades radiotherapy has been conducted mostly using X-rays and electrons which own a broad energy-depth distribution, depositing most of their energy in the tissues before reaching the target cells. Motivated by their more favorable energy loss properties, ions have started being used for cancer therapy and synchrotrons started to be implemented in hospitals with huge dimensions and costs for both the accelerator and the beam transport to the patient (gantry). In this sense laser-accelerated ions might be re-

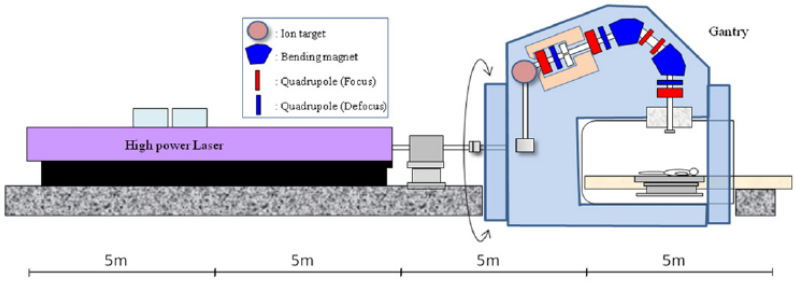

Figure 4: *Concept of a laser-accelerated ion transport line within a gantry [39].*

ally promising candidates since would reduce the systems dimensions thanks to huge accelerating fields in plasmas, and simplifying the beam

transport where the orientation optics would be aimed to curve the laser and not the ion beam (see Fig. 4). To really exploit laser-driven beams for clinical purposes and to make them truly competitive with respect to classical synchrotrons, an enhancement in spectrum narrowness, repetition rate and mostly in maximum ion energy are requested [39, 40], since e.g. 250 MeV protons and 430 MeV/u carbon ions are needed to destroy deep tumor cells.

Motivation and goal of PhD Thesis

Ions accelerated by laser pulses, as shown previously, are found to be very promising for different application fields. Every application requires the optimization of one or more beam parameter and in general these are different passing from one another. To exemplify in fact, in proton radiography spectrum broadness and short spatial/temporal bunch duration are needed; in the proton-driven fast-ignitor scheme of ICF a narrow energy spectrum and a sufficiently high laser-to-ion conversion efficiency are essential; in laser-driven IBT a tunable broadness spectrum is required as well as a sufficiently high cut-off energy (> 100 MeV) and a reasonable repetition rate (~ 1 Hz). To optimize a quantity a general procedure would be to get a fundamental theoretical understanding of the system, combined with novel experimental approaches. In the present work we focus our attention on one of proton beam parameters, that is to say the maximum energy. The goal is achieved by a two-steps methodology and illustrated below.

1. First we exploit the dependencies of proton cut-off energy on laser parameters in order to control maximum proton energy. An analytical analysis of TNSA process has been carried on and scaling laws with the principal laser parameters (pulse power, intensity, energy and focal spot) have been obtained. Moreover a further support on their prediction capabilities has been given by an extensive and systematic comparison with numerical Particle-In-Cell (PIC) simulations and literature data sets.

2. Besides the predictions involving an improvement of laser performances, we have then coped with the possibility to get a smarter experimental setup to enhance maximum proton energy only by manipulating target properties. In fact from the description reported above, it can be evinced how the energy gained by TNSA-accelerated ions is inherently limited by the fraction of laser energy absorbed by the target. The road followed in this work has been to improve the transfer of energy from laser pulse to target electrons, by means of a low-density coverage of the illuminated side of the solid target. In fact a larger EM energy absorption within the so-called "near-critical" regime has been recently demonstrated, that means to make the laser pulse interacting with a medium having densities around few mg/cm^3 for incident wavelengths $\lambda \sim 1\mu$m. Hence we have engineered a multi-layered target configuration

composed by an ordinary solid foil covered by a micrometric near-critical layer on the laser-illuminated surface, in order to enhance the laser absorption, fast electron generation and finally the TNSA accelerating fields. The experimental production of these targets has been tackled by means of pulsed laser deposition (PLD) which allows a fine control of density and thickness of the low-density film. Since density characterization constitutes a crucial point, a new technique exploiting energy dispersive X-ray spectroscopy (EDXS), alternative to the most common one of quartz-crystal microbalance (QCM), has been developed and implemented. This has allowed to obtain a more reliable estimate of multi-layered targets mean density within the regime of interest. These targets have been tested in the framework of a "Laserlab-Europe" experimental campaign in CEA/SLIC Saclay laser facility, in which clear enhancement of ion acceleration within the explored sub-relativistic intensity range has been revealed.

The present thesis work has been organized following the so far presented logical path. A brief description of the contents for each chapter is given below.

Part I: Laser-ion acceleration: experimental and theoretical state of the art

Chapter 1 In this first lapse of thesis the general theoretical background is presented. After an introduction on the principal plasma characteristic parameters, we focus our attention on ionization processes taking place in the high intensity regime of laser-matter interaction and on the energy absorption mechanisms happening in the invested media. Here an important distinction is given, depending on the density of interacting media: we analyze the cases of "underdense" and "overdense" plasmas.

Chapter 2 Here we report an up-to-date state of the art of ion acceleration following ultraintense laser-matter interaction: first all the relevant experimental studies carried on so far are presented, with particular attention to the dependence of accelerated ions on laser and target properties. Afterwards the principal proposed mechanisms, i.e. Target Normal Sheath Acceleration (TNSA) and Radiation Pressure Acceleration (RPA) are presented.

Part II: Theoretical modeling of Target Normal Sheath Acceleration

Chapter 3 In this chapter a classification of the most important TNSA analytical models published in literature is reported. Afterwards, the implementation and the comparison of their predicting capabilities are presented on the basis of the of maximum ion energies coming from an extended experimental database collected in literature.

Chapter 4 Here an analytical development of one of the models presented in the previous chapter is reported. A series of scaling laws linking maximum ion energy with laser properties are calculated exploiting the model and a comparison with the same trends coming both from experiments and numerical PIC simulations is performed.

Part III: Nanoengineered targets for laser-driven ion acceleration

Chapter 5 In this chapter the possible roads to enhance ordinary TNSA process are discussed. An emphasis is given to the use of multi-layered ("foam-attached") targets, predicting a more efficient laser energy absorption if a low-density coverage is attached on a solid foil.

Chapter 6 Here a literature report on low-density materials and typical nuclear density measurement techniques are presented. Moreover we present the production technique we have adopted for the production of our foam-attached targets and the density measurement techniques we have exploited.

Chapter 7 In this chapter the results coming from the characterization of multi-layered foam-attached targets are reported. In particular the morphological and structural characterizations plus the density measurements are discussed in detail. Finally the target assembling is presented.

Chapter 8 Here we report the results coming from the experimental test of the previously discussed multi-layered foam-attached targets. Ion maximum energies are observed to enhance with respect to ordinary TNSA case, as intensity decreases.

Part I

Laser-ion acceleration: experimental and theoretical state of the art

1

Interaction of intense radiation with matter

In this chapter we will approach the main topic of this thesis starting from the physics of intense radiation-matter interaction, since this constitutes the "boundary condition" for the study of any laser-plasma secondary radiation and hence for the acceleration of ions, principal topic of this work. We will start in Section 1.1 with the definition of a plasma and the most important parameters characterizing it, such as the Debye length, the plasma frequency and the critical density. Secondly in Section 1.2 we will briefly explore the ionization mechanisms acting on atoms hit by an intense EM radiation. After showing how a plasma is created, we study in Section 1.3 the behavior of a plasma in the presence of an incident EM radiation. First we deduce the ponderomotive potential, a capital quantity driving the interaction in the nonlinear regime. Then we discriminate two distinct laser-plasma interaction regimes: in Section 1.3.1 we will discuss the energy absorption mechanisms in *underdense* plasmas, while in Section 1.3.2 the interaction of a solid density or *overdense* plasma.

1.1 Plasma characteristics

We define as *plasma* any state of matter that contains enough free charged particles for its dynamics to be dominated by electromagnetic forces [41]. Even at relatively low ionization degrees a gas may exhibit electromagnetic properties, in fact already at 1% ionization the max-

imum value of electrical conductivity is reached. Much of the matter in the Universe exists in the plasma state, since the outer layers of the Sun and stars in general are made up of matter in an ionized state and from these regions winds blow through interstellar space contributing, along with stellar radiation, to the ionized state of the interstellar gas. Moreover a plasma may be created at the laboratory scale by the interaction of matter with intense electromagnetic radiation, as we will see in Section 1.2.
A more formal argument to define the plasma state deals with its ability to maintain charge neutrality as a consequence of the combination between the low electrons inertia and the strong electrostatic fields arisen from any charge unbalance in the plasma. The electrostatic field due to any charge unbalance is shielded hence the associated force does not extend to the whole plasma volume and its range is finite. For example by assuming that a charge q is placed at a certain point within an otherwise neutral plasma, the effect is that ions are repelled from that point, while electrons are attracted so yielding a "neutralizing cloud" around charge q. Ignoring ion motion (density Zn_i) and assuming that the non-relativistic number density of the electron cloud n_c is given by the Boltzmann distribution, $n_c = n_e \exp(e\phi/T_e)$, where T_e is the electron temperature, we solve Poisson's equation for the electrostatic potential $\phi(\mathbf{x})$ in the plasma, taking the charge q to be the origin

$$\Delta\phi(\mathbf{x}) = 4\pi e\,(n_c - Zn_i) - 4\pi q\delta(\mathbf{x}). \tag{1.1}$$

Since the equation is homogeneous everywhere except for the origin, we solve it without the inhomogeneous term $4\pi q\delta(r)$ for $r \to \infty$. Here we can linearize the exponential term since $\phi \to 0$ as $r \to \infty$, and fix global plasma neutrality $Zn_i = n_e$, so that equation (1.1) in spherical symmetry becomes

$$\frac{1}{r}\frac{\mathrm{d}^2}{\mathrm{d}r^2}\,(r\phi) = \frac{4\pi n_e e^2 \phi}{T_e}. \tag{1.2}$$

The homogeneous solution is $r\phi = b\exp(-r/\lambda_D)$ and, in order to correctly evaluate constant b, must match the solution at $r \to 0$ which is "Coulomb-like" $\phi(r) = q/r$. The shielded potential ("Yukawa-like") then reads:

$$\phi(r) = \frac{q}{r}\exp\left(-\frac{r}{\lambda_D}\right). \tag{1.3}$$

We have defined the quantity $\lambda_D \equiv (4\pi n_e e^2/T_e)^{1/2}$ known as *Debye length*, which represents the maximum charge separation a plasma is

able to sustain before being neutralized. Since we used Boltzmann statistics, there must be a large number of electrons inside a Debye sphere, i.e. $n_e\lambda_D^3 \ggg 1$. If we consider the inverse of this number, which is defined as the *plasma parameter* g, it finds itself proportional to the ratio between the potential energy of short range Coulombian collisions between particles and the particles mean kinetic energy:

$$g \equiv \frac{1}{n_e\lambda_D^3} \propto \frac{e^2/n_e^{-1/3}}{T_e} \lll 1. \tag{1.4}$$

Hence the more particles there are in the Debye sphere, the less important are the collisions to describe plasma dynamics in favor of collective interactions. This condition is achieved by considering a dense and hot plasma (high T_e, i.e. mean kinetic energy). The most important of these collective interactions are the plasma oscillations compensating any charge unbalance larger than λ_D. The electrostatic fields which restore the charge separations cause oscillations at a characteristic frequency known as *plasma frequency* ω_p. Since the unbalance occurs over a distance λ_D and the electrons thermal velocity is $(T_e/m_e)^{1/2}$, the electron plasma frequency in non-relativistic approximation may be expressed by:

$$\omega_{pe} = \frac{(T_e/m_e)^{1/2}}{\lambda_D} = \left(\frac{4\pi n_e e^2}{m_e}\right)^{1/2}. \tag{1.5}$$

Any external fields with frequencies less than the electron plasma frequency are prevented from penetrating the plasma by the more rapid electron response which neutralizes the field. Thus a plasma is opaque to electromagnetic radiation with frequency $\omega < \omega_{pe}$. The threshold condition $\omega = \omega_{pe}$ may be written in terms of a critical plasma density n_c by exploiting (1.5): n_{cr} as a function of incident frequency ω reads

$$n_{cr}(\omega) = \frac{m_e\omega^2}{4\pi e^2} \simeq 1.1 \times 10^{21} \left(\frac{\lambda}{\mu\mathrm{m}}\right)^{-2} \ \mathrm{cm}^{-3} \tag{1.6}$$

A plasma with density $n_e < n_{cr}(\omega)$ is transparent to incident radiation of frequency ω and is referred to as *underdense*. While a plasma having density $n_e > n_{cr}(\omega)$ is opaque to radiation with frequency ω and is called *overdense*. This difference constitutes an important demarcation line between two regimes of radiation matter interaction, so assuming a relevant role in the following discussion.

1.2 Ionization mechanisms

After a brief introduction on the main parameters characterizing the plasma state, we now address our attention to the ionization mechanisms occurring in a medium after being invested by an intense electromagnetic radiation, bringing it to plasma state. We firstly review the principal field ionization mechanisms occurring on single atoms, then we extend these considerations to the case of a material.
An electron invested by an electromagnetic radiation is ejected from an atom if it receives a sufficiently large energy amount to promote itself from a bound state to a free continuum level. This may happen either by absorbing a single high-frequency photon as in the photoelectric effect, or several lower frequency photons. The latter case is known as *multiphoton ionization* and strongly depends on the incident light intensity (see Fig. 1.1(a)). As explained in the Introduction, for the process of interest in this work high radiation intensities are required, so in order to define an electromagnetic radiation as "intense", some benchmark quantities are taken from the hydrogen atom. In the Bohr model the electric field found at a Bohr radius distance ($a_B = \hbar^2/m_e e^2$) from the nucleus reads

$$E_a = \frac{e}{a_B^2} \simeq 5.1 \times 10^9 \text{ Vm}^{-1}. \tag{1.7}$$

As a consequence it is possible to get the intensity at which the laser field matches the binding strength of the electron to the atom [42], known as *atomic intensity*:

$$I_a = \frac{cE_a^2}{8\pi} \simeq 3.51 \times 10^{16} \text{ Wcm}^{-2}. \tag{1.8}$$

A laser intensity $I_L > I_a$ would guarantee ionization for any target material, although it can occur already well below this threshold value via multiphoton effects. To evaluate the n-photon ionization rate, a perturbative approach is needed, hence giving:

$$\Gamma_n = \sigma_n I_L^n. \tag{1.9}$$

Provided the intensity is sufficiently high ($> 10^{10}$ Wcm^{-2}) the process can occur despite the cross-section σ_n decreases with n. As intensity increases an effect known as *above-threshold ionization* has been observed to take place. Electrons may absorb more photons than strictly necessary to escape the atomic potential and the electrons energy spectra show peaks beyond the ionization energy separated by the photon

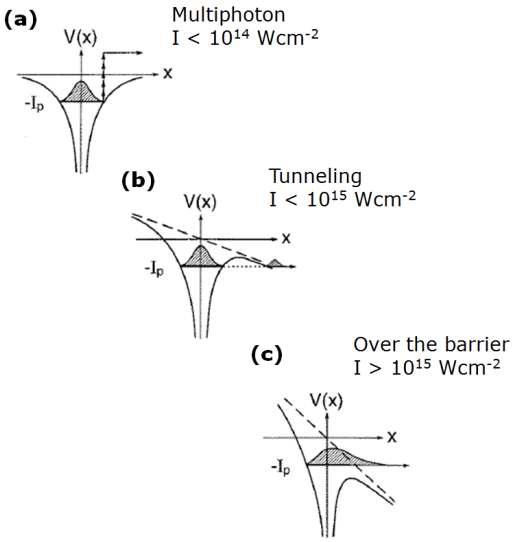

Figure 1.1: *Schematic picture showing the possible ionization mechanisms. (a) At $I_L < 10^{14}$ Wcm^{-2} multiphoton ionization dominates. (b) As intensity increases the atomic potential is distorted and tunneling ionization becomes possible. (c) At even higher intensities the barrier becomes smaller than the bound level, allowing the electron to escape (font: [43]).*

energy. This effect cannot be efficiently modeled by a perturbative approach since the external field becomes comparable with the atomic field (i.e. as I_L approaches I_a). In this regime the field is able to distort the atomic potential so that a barrier is formed through which the electron can tunnel, allowing a new ionization mechanism known as *Tunneling ionization* to take place (see Fig. 1.1(b)). Multiphoton and tunneling regimes are separated qualitatively by a quantity γ_k known as Keldysh parameter [43]:

$$\gamma_k = \omega_L \sqrt{\frac{2W_f}{I_L}}, \tag{1.10}$$

where W_f is the ionization potential and ω_L the frequency of the incident light. For $\gamma_k < 1$, i.e. at high intensity and sufficiently long wavelength radiation, tunneling dynamics dominates. When intensity increases further the barrier becomes smaller until the ground state is no longer bound (see Fig. 1.1(c)). This scenario is known as *over-the-barrier ionization* and the critical field is obtained by equating the top of the induced potential barrier to the binding energy. The corre-

sponding critical intensity reads:

$$I_{app} = 4 \times 10^9 \left(\frac{W_f}{\mathrm{eV}}\right)^4 Z^{-2} \ \mathrm{Wcm}^{-2}. \tag{1.11}$$

This value lowers by some orders of magnitude the atomic intensity, reason why an atom can be completely ionized well before light intensity reaches inter-atomic binding levels. For example in hydrogen ($Z = 1$) one obtains from (1.11) that $I_{app} = I_a/256$. For the regime of laser-matter interaction treated in this work, i.e. subpicosecond laser pulses, tunneling and over-the-barrier ionization are likely to take place if we are dealing with a gas or a rarified medium. On the other hand for solid targets collisional ionization rates will usually take over from field ionization once enough electrons have been released. Short pulse lasers produce optically thin plasmas where radiative and absorptive processes do not balance and the charge distribution may be obtained only by solving time-dependent atomic-rate equations taking the form:

$$\frac{\mathrm{d}n_Z}{\mathrm{d}t} = n_e n_{Z-1} S(Z-1) - n_e n_Z [S(Z) + \alpha(Z)] + n_e n_{Z+1} \alpha(Z+1) \tag{1.12}$$

with the constraints:

$$\sum n_Z = n_0; \quad \sum Z n_Z = n_e \tag{1.13}$$

where n_0 is the medium density and $S(Z)$ and $\alpha(Z)$ are the ionization and recombination rates of the ion charge state Z, respectively. Nevertheless the determination of charge distribution in a solid medium invested by an intense and short laser pulse is not straightforward at all, being a still ongoing research field. From the contents above, the main difficulties can be sketched as follows:

- Problems in computing the coefficients $S(Z)$ and $\alpha(Z)$, except for using mixed models [42].
- In our case of very intense and short laser pulses, field ionization (mainly tunneling and over-the-barrier) will take place together with collisional one governed by equations (1.12)-(1.13).
- Atoms in a solid medium have their binding potentials modified both by the laser field and by the neighbouring ions.

In conclusion for our purpose we consider a scenario in which tunneling, over-the-barrier and contact ionization coexist. The rates of the

former will saturate for each charge state after the critical intensity value indicated by (1.11), while the latter becomes more important the more medium density increases. This oversimplified picture addresses our attention mainly on two important process parameter in the interaction: laser intensity and medium density, which assume important roles in the analysis carried on in this thesis. In the following of this chapter a brief review on laser absorption by the plasma is reported, discriminating the underdense and overdense regimes, introduced in Section 1.1.

1.3 Laser-plasma interaction

In this section we discuss the interaction of a medium in the plasma state with a short intense laser pulse. The wavelengths of interest for such a class of lasers fall in the IR spectral range. Since we are dealing with subpicosecond pulses, the interaction takes place on the electron dynamics time scale, so electrons are directly excited by the laser field. Their dynamics is nonlinear due to the large amplitude owned by the laser field and a physical quantity characterizing the interaction process is the so-called *ponderomotive force*. We first derive it for the case of a single particle, before extending the result to the case of a plasma. Given a particle of mass m and charge q subject to an oscillating electric field $\mathbf{E}(\mathbf{x},t) = \mathbf{E}_0(\mathbf{x})\cos(\phi)$, with $\phi = \omega t - \mathbf{k}\cdot\mathbf{x}$, the equation of motion can be written as:

$$\frac{\mathrm{d}^2\mathbf{x}}{\mathrm{d}t^2} = \frac{q}{m}\left(\mathbf{E} + \frac{\dot{\mathbf{x}}}{c}\wedge\mathbf{B}\right). \tag{1.14}$$

Due to its strong nonlinearity we adopt a first order perturbative approach with

$$\mathbf{E}(\mathbf{x}) = \mathbf{E}(\mathbf{x}_c) + \left[(\mathbf{x}-\mathbf{x}_c)\cdot\nabla\right]\mathbf{E}|_{\mathbf{x}_c} \tag{1.15a}$$

$$\mathbf{x} = \mathbf{x}^{(0)} + \mathbf{x}^{(1)} \tag{1.15b}$$

where $\mathbf{x}_c$ is the initial position of the particle. Then equation (1.14) may be split into two equations: the zeroth order one reads

$$\begin{aligned} &\frac{\mathrm{d}^2\mathbf{x}^{(0)}}{\mathrm{d}t^2} = \frac{q}{m}\mathbf{E}(\mathbf{x}_c) \\ &\longrightarrow\ \mathbf{x}^{(0)} = \mathbf{x}_c - \frac{q\mathbf{E}_0}{m\omega^2}\cos(\phi) \end{aligned} \tag{1.16}$$

while the first order one is:

$$\frac{\mathrm{d}^2(\mathbf{x}^{(0)}+\mathbf{x}^{(1)})}{\mathrm{d}t^2} = \frac{q}{m}\left\{\mathbf{E}(\mathbf{x}_c) + [(\mathbf{x}^{(0)}-\mathbf{x}_c)\cdot\nabla]\mathbf{E}(\mathbf{x}_c) + \dot{\mathbf{x}}^{(0)}\wedge\mathbf{B}\right\}. \tag{1.17}$$

Now we subtract equation (1.16) from (1.17) and substitute $(\mathbf{x}^{(0)} - \mathbf{x}_c)$ and $\dot{\mathbf{x}}^{(0)}$ from zeroth order solution in (1.16). Moreover we use Faraday equation to write the magnetic field in terms of the electric field obtaining the equation of motion for the first-order correction:

$$\begin{aligned}\frac{\mathrm{d}^2\mathbf{x}^{(1)}}{\mathrm{d}t^2} = &-\left(\frac{q}{m\omega}\right)^2\Big[(\mathbf{E}_0\cdot\nabla)\,\mathbf{E}_0\cos^2(\phi) + \mathbf{E}_0\wedge(\nabla\wedge\mathbf{E}_0)\sin^2(\phi) + \\ &+\frac{1}{2}\,\mathbf{E}_0\wedge(\mathbf{k}\wedge\mathbf{E}_0)\sin(2\phi)\Big].\end{aligned} \tag{1.18}$$

If we now take the average over one oscillation period of the field, the 2ω oscillating term vanishes and equation (1.18) becomes:

$$\frac{\mathrm{d}^2\langle\mathbf{x}^{(1)}\rangle}{\mathrm{d}t^2} = -\frac{1}{2}\left(\frac{q}{m\omega}\right)^2\left[(\mathbf{E}_0\cdot\nabla)\,\mathbf{E}_0 + \mathbf{E}_0\wedge(\nabla\wedge\mathbf{E}_0)\right], \tag{1.19}$$

which can be further simplified exploiting a vector identity resulting in the final form:

$$m\frac{\mathrm{d}^2\langle\mathbf{x}^{(1)}\rangle}{\mathrm{d}t^2} = -\left(\frac{q^2}{4m\omega^2}\right)\nabla|\mathbf{E}_0|^2 = -\nabla U_p. \tag{1.20}$$

With the average operation the zeroth order dynamical component has been elided, hence isolating the first order dynamics which is driven

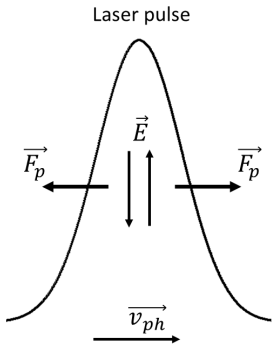

Figure 1.2: *Sketch representing a laser pulse propagating with phase velocity v_{ph} at the ponderomotive force directed opposite to the intensity gradient.*

by the term $F_p = -\nabla U_p$, known as the ponderomotive force. U_p is the ponderomotive potential, proportional to the symmetric component of the electromagnetic stress tensor, i.e. to the radiation pressure. The averaged ponderomotive force comes from spatial inhomogeneities of the radiation pressure and is directed towards regions of decreasing intensity. As show in Fig. 1.2 the particle is kicked forward as the wave is approaching, while is pushed backward as the wave is passed through.
It is possible to extend this result to the case of a plasma by considering an electronic fluid having density n_e. In this case, starting from (1.20), we obtain a ponderomotive force density by adding a factor n_e:

$$\mathbf{f_p} = -\frac{q^2 n_e}{4m\omega^2}\nabla\langle|\mathbf{E}_0|^2\rangle = -\frac{\omega_{pe}^2}{\omega^2}\nabla\langle\left|\frac{\mathbf{E}_0}{8\pi}\right|^2\rangle, \tag{1.21}$$

where ω_{pe} is the electronic plasma frequency defined in (1.5). RHS of equation (1.21) can be proved being proportional to $(1/2)n_e m_e\langle v_{osc}^2\rangle$ which is associated to the ordered motion of the electronic fluid element and generating the radiation pressure. In analogy with thermal pressure, which is due to the disordered thermal motion.

1.3.1 Underdense plasmas

Owing to the properties reported in Section 1.1 a laser pulse incident on an underdense plasma will be able to propagate through it. As the pulse drills the plasma, the ponderomotive force tends to separate electrons from ions, leaving in its wake local charge separations (see Fig. 1.3). These charge separations will likely trigger plasma oscillations. Such a wake is most effectively generated if the duration of the electromagnetic wave packet is half the period of the plasma waves in the wake $\tau_L = \pi/\omega_p$ [9]. This resonant situation will be discussed at the end of the present section. The more straightforward way to quantitatively describe the laser energy absorption via the excitation of plasma waves in an underdense plasma deals with the relativistic fluid theory of a cold plasma by Akhiezer and Polovin [44]. The system of equations to be solved considering only the collisionless (since we are dealing with hot plasmas) electron dynamics in a neutralized

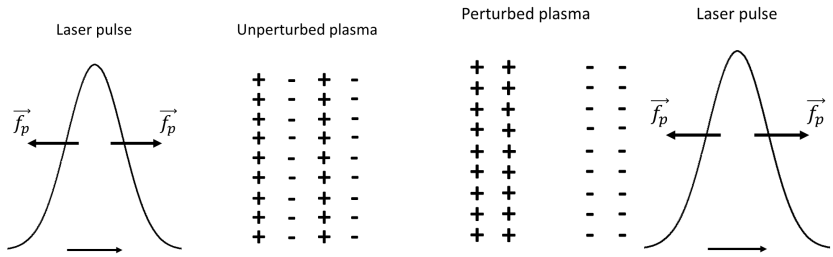

(a) Picture before the laser pulse crosses the plasma slab.

(b) Picture after the laser has passed: local charge separations have been formed.

Figure 1.3: *Schematic view of the nonlinear effect on plasma species due to the ponderomotive force.*

ionic fluid with density n_0 is the following:

$$\frac{\partial}{\partial t}\left(\gamma n_e\right) + \nabla \cdot \left(n_e \mathbf{u}\gamma\right) = 0 \tag{1.22a}$$

$$\frac{\partial \mathbf{p}}{\partial t} + \left(\mathbf{u}\cdot\nabla\right)\mathbf{p} = -e\left(\mathbf{E} + \frac{\mathbf{u}}{c}\wedge\mathbf{B}\right) \tag{1.22b}$$

$$\nabla\cdot\mathbf{E} = 4\pi e(n_0 - n_e) \tag{1.22c}$$

$$\nabla\wedge\mathbf{E} = -\frac{1}{c}\frac{\partial\mathbf{B}}{\partial t} \tag{1.22d}$$

$$\nabla\cdot\mathbf{B} = 0 \tag{1.22e}$$

$$\nabla\wedge\mathbf{B} = -\frac{4\pi}{c}en_e\mathbf{u} + \frac{1}{c}\frac{\partial\mathbf{E}}{\partial t} \tag{1.22f}$$

where n_e is the electron density, $\mathbf{u}$ the electron velocity field, $\mathbf{p} = m_e\gamma\mathbf{u}$ the electron momentum and $(\mathbf{E},\mathbf{B})$ the electric and magnetic fields of the incident wave propagating along the z-axis. To solve the system in the nonlinear regime let us consider the propagation of a plane wave, i.e. assuming a constant phase velocity, so that the spatiotemporal dependence of every quantity becomes $f(\omega\tau)$, where $\tau = \mathbf{e}_k\cdot\mathbf{x}/v_{ph}$, being $v_{ph} = \omega/k$ the phase velocity. After few steps, the equations of the system become EDOs that allow calculating the plasma velocity field: two (identical) equations for the transverse modes and one for the longitudinal component:

$$\frac{\mathrm{d}^2 p_{x,y}}{\mathrm{d}\tau^2} + \frac{\omega_p^2\beta_{ph}^2}{\beta_{ph}^2 - 1}\cdot\frac{\beta_{ph}u_{x,y}}{\beta_{ph} - u_z} = 0 \tag{1.23a}$$

$$\frac{\mathrm{d}}{\mathrm{d}\tau}\left[\left(u_z - \beta_{ph}\right)\frac{\mathrm{d}p_z}{\mathrm{d}\tau} - u_x\frac{\mathrm{d}p_x}{\mathrm{d}\tau} - u_y\frac{\mathrm{d}p_y}{\mathrm{d}\tau}\right] - \frac{\omega_p^2\beta_{ph}^2 u_z}{\beta_{ph} - u_z} = 0, \tag{1.23b}$$

where the quantity $\beta_{ph} = v_{ph}/c$ has been introduced and the normalizations $n_e/n_0 \to n$, $\mathbf{u}/c \to \mathbf{u}$, $\mathbf{p}/c \to \mathbf{p}$ and $\mathbf{E}, \mathbf{B}/(m_e\omega_p c/e) \to \mathbf{E}, \mathbf{B}$ have been performed. Once the velocity field is known then, density reads:

$$n = \frac{\beta_{ph}}{\beta_{ph} - u_z}. \tag{1.24}$$

So does the fields:

$$B_{x,y} = \mp \frac{1}{\beta_{ph}\omega_p} \frac{\mathrm{d}p_{x,y}}{\mathrm{d}\tau} \tag{1.25a}$$

$$B_z = 0 \tag{1.25b}$$

$$E_{x,y} = -\frac{1}{\omega_p} \frac{\mathrm{d}p_{x,y}}{\mathrm{d}\tau} \tag{1.25c}$$

$$E_z = -\frac{1}{\beta_{ph}\omega_p} \frac{\mathrm{d}}{\mathrm{d}\tau} \left[\beta_{ph} p_z - \left(1 + p^2\right)^{1/2} \right]. \tag{1.25d}$$

Now we have the system of equations, let us solve it for the case of weak nonlinearity, i.e. without consider relativistic effects ($p \simeq u \ll 1$). We assume the pump wave being linearly polarized along y-axis, so that a transverse y dynamics is induced. Equation (1.23b) for the longitudinal dynamics reduces to

$$\frac{\mathrm{d}^2 u_z}{\mathrm{d}\tau^2} + \omega_p^2 u_z = \frac{1}{2\beta_{ph}} \frac{\mathrm{d}^2 u_y^2}{\mathrm{d}\tau^2}. \tag{1.26}$$

A more physical picture is given by considering the longitudinal charge displacement δn as a variable instead of u_z: $\delta n \equiv (n_e - n_0)/n_0 = u_z/(\beta_{ph} - u_z) \simeq u_z/\beta_{ph}$, where equation (1.24) and the weak nonlinearity assumption have been used. Thus equation (1.26) for the charge displacement reads

$$\frac{\mathrm{d}^2 \delta n}{\mathrm{d}\tau^2} + \omega_p^2 \delta n = \frac{1}{\beta_{ph}^2} \frac{\mathrm{d}^2}{\mathrm{d}\tau^2} \left(\frac{u_y^2}{2} \right). \tag{1.27}$$

While the homogeneous solution of (1.27) gives the well known longitudinal electrostatic modes $\omega = \omega_p$, in the weakly nonlinear case a traveling transverse wave in the plasma generates a longitudinal charge oscillation. To better understand the nature of the inhomogeneous term we recall a perturbative approach in solving equation (1.27): the zeroth-order response of a y-axis polarized pump wave is $u_y^{(0)} = a$, where we have defined the normalized vector potential $a \equiv eA/m_e c$.

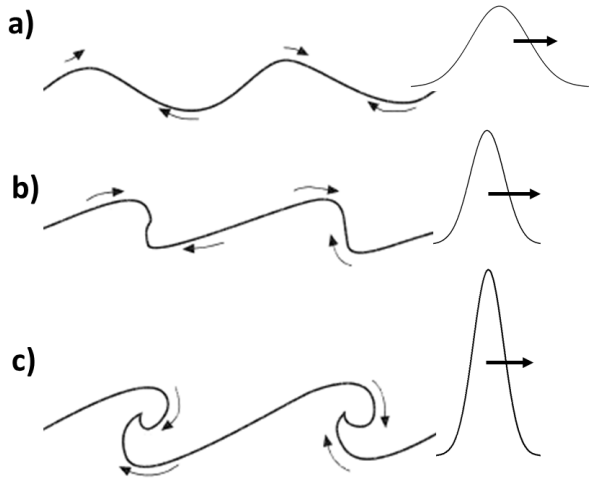

Figure 1.4: *Schematic representation of the wakefield generation after the propagation of lasers having different intensities. (a): weakly nonlinear case $a \ll 1$. (b): Relativistic intensity $a \sim 1$. (c): Wave-breaking at $a > 1$.*

Now we substitute the zeroth-order solution in the inhomogeneous term and, by going back to spatiotemporal coordinates $(\mathbf{x}, t)$, we obtain:

$$\frac{\partial^2 \delta n}{\partial t^2} + \omega_p^2 \delta n = c^2 \frac{\partial^2}{\partial z^2} \left(\frac{a^2}{2} \right). \tag{1.28}$$

The pump term is linked to the spatial inhomogeneity of the laser field, i.e. to the poderomotive potential we have calculated at the same approximate order in equation (1.20). Hence even with a weakly nonlinear treatment, we can clearly show how a laser pulse propagating in an underdense plasma transfers its energy by exciting longitudinal plasma waves (followed by electrostatic modes). This important effect is called *wakefield generation*. The picture describing the effect for weak nonlinearity ($a \ll 1$) is reported in Fig. 1.4(a). When the laser intensity increases and the condition $a \sim 1$ is approached, the effect shows a more peaked density profile (see Fig. 1.4(b)). In this case the fully nonlinear solution of equation (1.23b) is needed for a quantitative description. If a increases further, the particle propagation velocity u_z may reach the wave phase velocity v_{ph}: in this singular case the wave may break its spatial coherence and part of it overcomes the remaining, making groups of electrons be trapped (see Fig. 1.4(c)). This phenomenon is referred to as *wave breaking* and might be exploited for particle acceleration. In fact the trapped particles may feel the

longitudinal electric field generated after plasma oscillations, which is given by equation (1.25d) after equation (1.23b) is solved exactly for arbitrary amplitude oscillations. The maximum value reached by this field is:

$$E_{max} = \sqrt{2}\,\frac{m_e c\omega_p}{e}\,(\gamma_{ph}-1)^{1/2} \simeq \left(\frac{n_e[\mathrm{cm}^{-3}]}{10^{18}}\right)^{1/2} f(v_{ph})\ \mathrm{GVcm}^{-1} \tag{1.29}$$

being $\gamma_{ph} = (1-\beta_{ph}^2)^{1/2}$. This field is more than 3 orders of magnitude higher than the ones generated by radiofrequency cavities in conventional accelerators. Moreover it is evident from (1.29) that the electron acceleration process may be optimized by increasing plasma density, since the maximum field increases as n_e approaches the critical value n_{cr} (see Section 1.1).
In conclusion we have shown in the simplest way how the first nonlinear effect following the propagation of a laser pulse in an underdense plasma is the excitation of plasma waves, which are able to drive highly nonlinear phenomena (seen only implicitly in our treatment) like electron acceleration and, for example, other effects with resonant behavior known as *parametric instabilities*. A pump EM wave triggers plasma oscillations and they may scatter each other generating a third wave.

1.3.2 Overdense plasmas

In the case of a solid invested by a laser pulse one cannot study the response of the matter to the light passing through it as we have done for an underdense plasma. The plasma created by the first laser cycles through field ionization (see Section 1.2), known as *pre-plasma*, will blow off from the front of the target at approximately the sound speed c_s. Assuming the plasma expands isothermally, the density profile will assume an exponentially decreasing form with a scale length $L = c_s\tau_L$, being τ_L the laser pulse duration. The remaining part of the laser pulse will then interact either with a low density expanding plasma or a high density mirror-like wall of of plasma, depending on the pulse duration. As pointed out in the Introduction, the pulse durations of interest in this work fall in the femtosecond range, so the situation we are facing with is the second one, where the plasma interface shows a steep gradient which drops to densities higher than the critical value, hence avoiding the penetration of the remaining part of the laser pulse (see Section 1.1), except for an evanescent component inside a characteristic *skin depth* $l_s = c/\omega_p = (\lambda/2\pi)\sqrt{n_{cr}/n_e}$. This of course supposes that

the contrast ratio[1] of the laser system is sufficiently high that the surface remains unperturbed until the main pulse arrives. On the contrary the main pulse will interact with a pre-plasma having an exponentially decreasing density profile created by the pre-pulse. The laser propagates until the critical surface is reached, exciting plasma waves as seen in the previous section. These waves grow over a number of laser periods and are eventually damped either by collisions or by particle trapping and wave breaking. For rather long density scale lengths, defined by $kL \gg 1$ ($k = 2\pi/\lambda$ is the laser wave vector and L the density profile scale length), the energy absorption fraction depends on the parameter $\xi = (kL)^{1/2} \sin\theta$, where θ is the angle of incidence of the laser pulse:

$$\eta \simeq 2\xi^2 \exp\left(-4\xi^3/3\right). \tag{1.30}$$

This behavior does depend on the damping mechanism, but a maximum absorption rate of 60% may be obtained in the long scale length limit at an optimal angle of incidence θ_{opt} such that $\sin\theta_{opt} = 0.8(kL)^{-1/3}$ [42]. Nevertheless, despite it may lead to high absorption rates, the control of the density profile of the pre-plasma created by the laser pedestal is not straightforward, reason why it is often suppressed using high contrast ratio laser systems. In the presence of steep density gradients the so-called *resonance absorption* ceases to work, since the oscillation amplitude of the plasma waves would likely exceed the density scale length and no energy may be transferred from the laser to the plasma if the latter is not able to support charge oscillations. On the other hand electrons near the edge of a steep plasma-vacuum interface will be direct exposed to the laser field. An electron arriving at the right moment in the laser cycle may be dragged out into the vacuum. As the field reverses its direction, the same electron will be accelerated back into the plasma. Being the latter highly overdense, the electric field cannot propagate further than a skin depth and the electron can propagate in the target until is is moderated or absorbed through collisions. This "not-so-resonant resonant absorption" has been modeled by Brunel [45] neglecting the magnetic field of the incident wave and assuming the laser electric field E_L, incident with an angle θ, has some component normal to the target surface $E_d = 2E_d \sin\theta$ able to put the electrons back and forth around their equilibrium positions (see Fig. 1.5). This effect is known as *Brunel mechanism*. Supposing the field puts the electrons at a distance Δx from the surface (having a step-

[1] The contrast ratio is defined as the level of the main pulse intensity to the pedestal or "pre-pulse" created by amplified spontaneous emission (ASE).

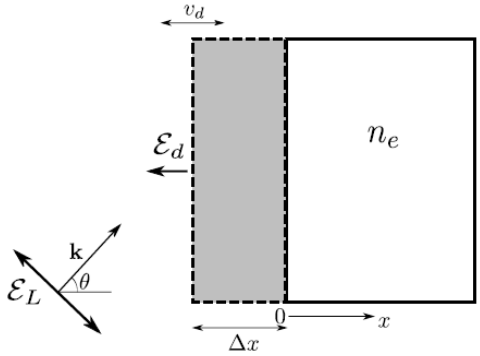

Figure 1.5: *Simplest version of the Brunel mechanism: the capacitive model.*

like profile) and calculating the restoring electric field, one obtains the fractional absorption rate by taking the ratio of the laser power lost to the solid and the initial laser power. In order to take into account even the relativistic velocities electrons may gain in an intense laser field and the imperfect reflectivity of the target surface, a refined result of Brunel's model is also available [45]. The latter result predicts a maximum absorption rate near unity at a quasi-grazing incidence angle (80-90°). By considering a more realistic picture where finite gradient density profile have been studied [46], the results obtained with numerical simulations give a totally different picture where the maximum absorption takes place around 45°. In Fig. 1.6 we reported the dependence of fractional absorption on laser irradiance and pofile scale length, where it saturates around 15-10% for $I_L\lambda^2 > 10^{16} - 10^{17}$ $\mathrm{Wcm}^{-2}\mu\mathrm{m}^2$. The huge difference from the Brunel electrostatic model from the numerical simulations are due mainly to the important role played by induced currents on the surface, which generate magnetic fields affecting the oscillation dynamics of the stripped electrons.

A third effect taking place in laser-solid interaction at high intensity is physically very similar to the Brunel mechanism. In fact electrons are directly accelerated by the laser field impinging on a step-like density profile. The main difference is that the driving term is somehow linked to the $\mathbf{v}\wedge\mathbf{B}$ term of the Lorentz force, reason why it is known as $\mathbf{j}\wedge\mathbf{B}$ heating. To give a quantitative description of this term let us recall the first-order equation of motion (1.18) calculated at the beginning of Section 1.3. If we consider an elliptically polarized wave propagating

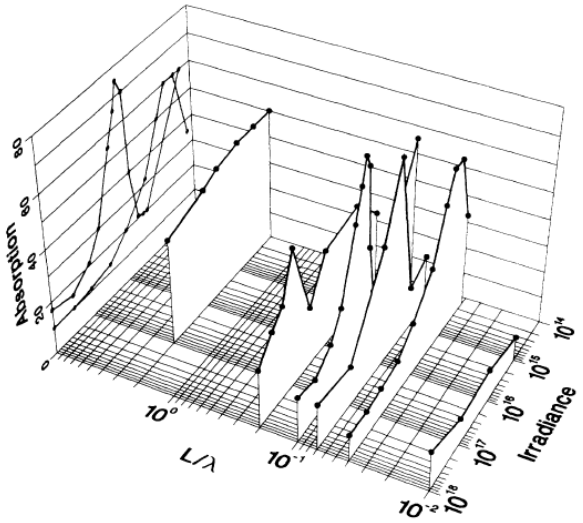

Figure 1.6: *Absorption percentage in the $I\lambda^2$-L/λ plane for a 45° angle of incidence (font: [46]).*

along z having a vector potential $\mathbf{A}(\mathbf{x}, t)$ of the form:

$$\mathbf{A}(\mathbf{x}, t) = \frac{A(0)}{\sqrt{1+\epsilon^2}} \mathrm{e}^{-z/d_p} \left(\hat{x} \cos \omega t + \epsilon \hat{y} \cos \omega t\right) \tag{1.31}$$

incident on an overdense plasma with a step-like electron density $n_e(z) = n_0 H(z)$, where $0 < \epsilon < 1$ is the ellipticity and $d_p = c/(\omega_p - \omega)^{1/2}$ is the skin depth. By substituting in equation (1.18), one obtains a first-order equation of motion for the electrons whose longitudinal component along z reads:

$$m_e \frac{\mathrm{d}^2 z^{(1)}}{\mathrm{d}t^2} = -F_0 \mathrm{e}^{-2z/d_p} \left(1 + \frac{1-\epsilon^2}{1+\epsilon^2} \cos 2\omega t\right). \tag{1.32}$$

where $F_0 = e^2 A(0)^2 / 2 d_p m_e c^2$. In addition to secular radiation pressure discussed at the beginning of Section 1.3, without averaging over a laser period there appears a high frequency component. By solving the equation (1.32) we obtain the electric field and the electron density perturbation, reading as

$$E_z = \frac{F_0}{e} \mathrm{e}^{-2z/d_p} \left(1 + \frac{1-\epsilon^2}{1+\epsilon^2} \frac{\cos 2\omega t}{1 - 4\omega^2/\omega_p^2}\right) \tag{1.33a}$$

$$\delta n_e = -\frac{1}{4\pi e} \frac{\partial E_z}{\partial z} \tag{1.33b}$$

For linearly polarized waves ($\epsilon = 0$) the oscillating term is larger than the secular one and may drag some electrons out into the vacuum side (i.e. crossing the $z = 0$ surface). This mechanism is followed by the self-intersection of electron trajectories in vacuum leading to heating and appearance of fast electron jets twice per laser cycle. For circularly polarized waves ($\epsilon = 1$), the oscillating term in (1.33b) vanishes, the electric force on electrons (1.33a) balances the ponderomotive force (1.32) ($F_z - E_z = 0$) and no electron heating occurs.
For laser intensities larger than 10^{18} Wcm^{-2} the interaction of sub-picosecond pulses with solid target is dominated by Brunel mechanism and $\mathbf{j} \wedge \mathbf{B}$ heating. As we have shown above, for linear polarized laser pulses the energy absorption leads to the generation of a population of energetic electrons, often referred to as "hot electrons", having mean energies in the keV-MeV regime, which expand isotropically through the medium. To determine their mean kinetic energy, or temperature, there exist several scaling with laser irradiance $I\lambda^2$. One of the most reliable lies on the assumption that the ponderomotive potential may be seen as an effective temperature whose gradient gives the radiation pressure, in analogy with the respective thermal quantities. The exact expression for the ponderomotive potential is:

$$U_p = m_e c^2 \left[\left(1 + a^2\right)^{1/2} - 1 \right]. \tag{1.34}$$

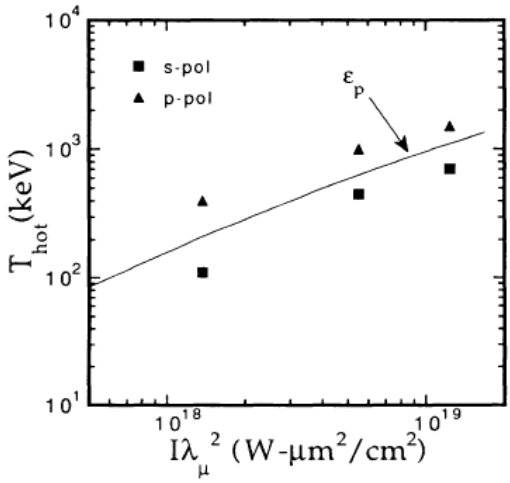

Figure 1.7: *Hot electron temperature vs. laser irradiance: within this intensity range the ponderomotive scaling well reproduces the experimental data (font: [47]).*

Since the normalized vector potential might be estimated as $a^2 \sim I\lambda^2/1.38 \times 10^{18}$, by imposing $U_p \simeq T_e$, one obtains:

$$T_e \simeq m_e c^2 \left[\left(1 + \frac{I\lambda^2[\mathrm{Wcm}^{-2}\mu\mathrm{m}^2]}{1.38 \times 10^{18}} \right)^{1/2} - 1 \right] \tag{1.35}$$

which is known as ponderomotive scaling first introduced by Wilks et al [47] and has been found well in agreement with the experimental data taken at intensities $> 10^{18}$ Wcm^{-2} (see Fig. 1.7).
The hot electron population plays a key role in the physics of laser-driven ion acceleration, which will be tackled in the next chapter.

2

Ion acceleration driven by intense laser pulses

This chapter exploits the review on laser-matter interaction at high intensity carried on previously, in order to focus the attention on the secondary laser-plasma source constituting the main topic of this work: the acceleration of ion beams. To recall what already said in the Introduction, the results coming from two parallel experiments, published in 2000 [24, 48], showed the emission of multi-MeV ion beams after an ultraintense and ultrashort laser pulse hit a thin solid film. The typical laser parameters include pulse energies between 0.1 and 1000 J, durations of 10-1000 fs and intensities spanning from 10^{18} to 10^{21} Wcm^{-2}. Regarding the target, both insulating and conductive materials have been used with thicknesses in the 0.01-100 μm range. In Section 2.1 a characterization of the accelerated ions is reported on the basis of the so far performed experiments. The direction of emission (front or rear), the nature of accelerated species, the dependencies on target and laser properties will be discussed. Afterwards in Section 2.2 an insight into the physics of laser-driven acceleration will be performed, by briefly explaining the Target Normal Sheath Acceleration (TNSA) mechanism which explains most of the experimental data and a second mechanism known as Radiation Pressure Acceleration (RPA) requiring certain laser performances to be observed, which have been obtained only recently.

2.1 Characteristics of ion emission

The ultraintense laser pulse is usually directed to oblique incidence on the target. This is due both to a practical reason (not to damage any optical component with the reflected light) and to a more physical reason related to the laser absorption mechanisms, discussed in Section 1.3.2, which are dominant in this intensity range (Brunel mechanism and $\mathbf{j} \wedge \mathbf{B}$ heating). The proton signal have been usually recorded either using a stack of radiochromic films (RCF) or a Thomson parabola ion spectrometer, both coupled with CR39 plastic nuclear track detectors. The former diagnostic exemplified in Figs. 2.1(a) and 2.1(d), is a RCF/CR39 sandwich track detector providing spatial and energetic information of protons emitted during the interaction. The latter, reported in Figs. 2.1(b) and 2.1(c), is a velocity selector able to deflect ions according to their charge-to-mass ratio and a CR39 film is placed behind to collect the ions tracks and to record their energy

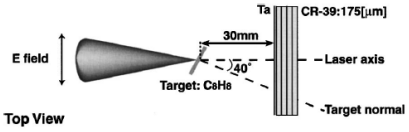

(a) RCF/CR39 stacks installed to detect protons signal from the rear side of the target (from [49]).

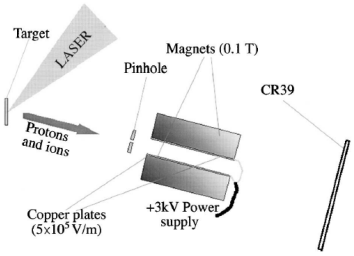

(b) Thomson parabola with a CR39 film behind to get proton signal emitted from the front surface (from [50]

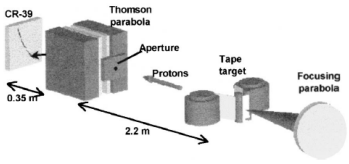

(c) Thomson parabola with a CR39 film behind to get proton signal emitted from the rear surface (from [51]

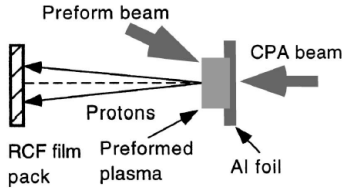

(d) Generation of a pre-plasma on the rear side in order to perturb the surface and inhibit proton acceleration. (from [52]

Figure 2.1: *Examples of possible experimental setups adopted in laser-driven ion acceleration.*

spectra with a higher resolution (for more details see Appendix A.2). Another adopted technique to record protons may exploit ad-hoc nuclear reactions to relate the production of radionuclides to the original signal. The proton signal may be measured either from the irradiated "front" side (as for example in [50,54,55]) or from the "rear" side of the target (see for example [49, 51, 52]). Fuchs et al [56] observed under the same laser conditions that while rear-side acceleration produces a collimated (<20°) beam of energetic protons >16 MeV, front-side acceleration produces a high-divergence, low-energy (<6 MeV) beam and accounts for less than 3% to the total proton energy. This is because the plasma generated on the front side by the laser pre-pulse plays a crucial role in the front-side acceleration. Mackinnon et al [52] observed that even rear side emission is strongly attenuated after the perturbation induced by a proper pulse reproducing pre-pulse intensity (see Fig. 2.1(d)). Some years later Ceccotti et al [59] proved that by enhancing the contrast ratio from the typical value of $\sim 10^6$ to $\sim 10^{10}$, ion acceleration can be obtained symmetrically at the front and the rear side of the target. In usual experimental conditions energetic ions come from the target surfaces and not from the bulk and protons are the dominant accelerated species irrespective of the target material [60], indicating that they belong to the hydrocarbon contam-

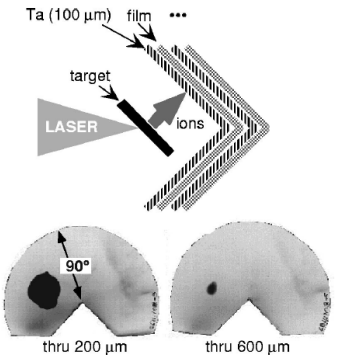

(a) Schematic view of a RCF detection system to show ions are emitted along the target normal (from [53]).

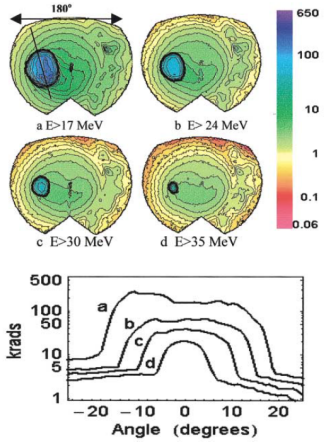

(b) Top: contour plots of dose as a function of angle. Bottom: plot of beam profile (from [24]

Figure 2.2: *Experimental results showing ions are emitted along the target normal with a rather uniform intensity profile.*

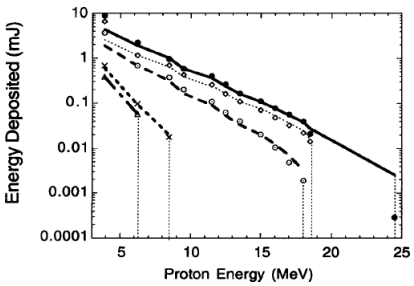

(a) Typical ion energy spectrum exponentially decreasing with a sharp cutoff (from [57]).

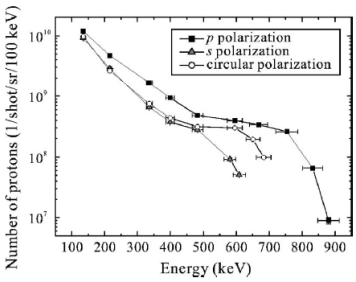

(b) Ion energy spectrum having an exponential decrease followed by a plateau and a sharp cutoff (from [58]).

Figure 2.3: *Examples of possible observed laser-accelerated ion energy spectra.*

inants deposited on the surfaces. A pilot experiment demonstrating this evidence is the one performed by Allen et al [60], in which a drastic negative drop in proton yield is observed after selectively removing the contaminants from rear surface using an Ar-ion sputter gun.
The spatial properties of rear side emitted protons have been first characterized in the experiment at laser Nova in 1999 [24, 53], where the preferred acceleration direction has been observed to be normal to the rear surface of the target as shown in Fig. 2.2(a) Moreover the beam has $\sim 10^\circ$ half-angle divergence and a rather uniform intensity profile with near circular sharp boundaries (see Fig. 2.2(b)) and an emittance less than 0.004 mm mrad, mainly due to the fact that protons co-propagate with lower energy electrons in a neutral plasma cloud [26].
The energetic spectra of the accelerated protons show typically an exponential decrease characterized by an effective temperature, followed by a sharp cutoff (see Fig. 2.3(a)) which is often referred to as *maximum ion energy*. Sometimes, as reported in Fig. 2.3(b), before the cutoff a plateau appears (see [50, 58, 61]), probably a sign that a two-temperature hot electron population might have been created in the interaction [62]. The estimated conversion efficiency from laser to hot electrons generated in the interaction with overdense plasmas is around 40%, while the fraction of laser energy that goes to protons is lower than 10%.
All the properties reported above show a strong dependence on laser and target properties. In the following, to remark their relevance, we will resume both dependencies in two distinct subsections.

2.1.1 Dependence on laser properties

A large number of experiments have been performed in order to study the dependence of the accelerated ion properties on the laser parameters: mainly laser intensity, energy and duration in addition to contrast-ratio and polarization. Proton energy spectrum and the maximum energy depend strongly on laser intensity. A collection of experimental data of ion peak energy plotted as a function of laser irradiance $I\lambda^2$ is showed in the work by Krushelnick et al [63] and reported in Fig. 2.4(a). Six orders of magnitude irradiance are spanned, but of interest is the regime where electron dynamics in the laser field becomes relativistic, i.e. above 10^{18} Wcm^{-2}. Here the maximum ion energy scales as $(I\lambda^2)^{0.5}$, which is similar to the observed trend for hot electron temperature in this regime via the ponderomotive scaling (1.35). In Fig. 2.4(b) a similar collection of data is reported but belonging to a narrower irradiance range, above the relativistic threshold. The same scaling $\sim I^{0.5}$ of peak energy with irradiance is found for pulse durations between 300 fs and 1 ps, while for shorter laser pulses a non-trivial linear scaling $\sim I$ is observed. Since intensity is not independent from the other laser properties, in order to extrapolate scalings with intensity it is more convenient to adopt configurations where only one parameter at time is varied. To this end there have been performed systematic experiments where intensity has been varied by means of either energy or duration keeping the remaining parameter fixed. The first configuration with intensity variable with laser energy and pulse

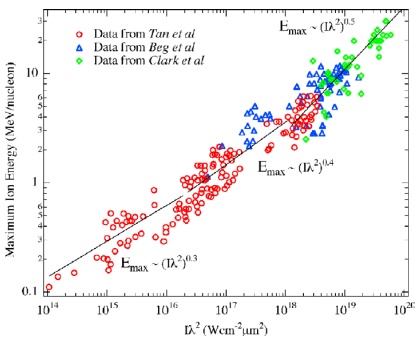

(a) Image from [63].

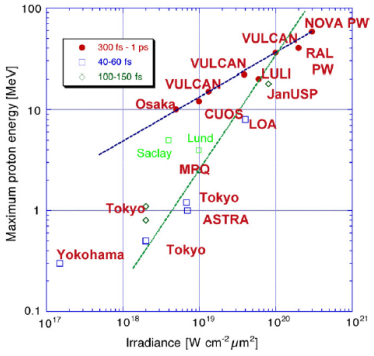

(b) Image from [64].

Figure 2.4: *Maximum ion energy experimental data plotted as a function of laser irradiance.*

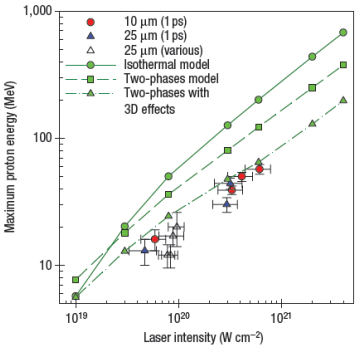

(a) Maximum proton energy detected as a function of laser intensity, by variation of the laser energy and with a constant pulse duration [65].

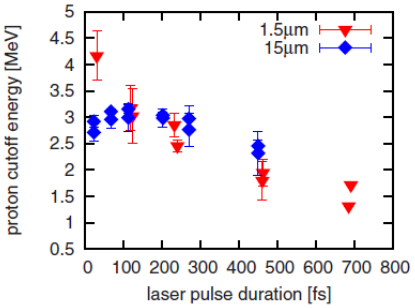

(b) Proton cutoff energies at different pulse durations (with fixed laser energy) [68].

Figure 2.5: *Examples of maximum proton energy experimental scalings with intensity.*

duration fixed is well represented by the results in [22, 65, 66]. The second configuration, with measurements of proton peak energy as a function of pulse duration with pulse energy fixed, finds good examples in [67–69]. As a general remark, the existence of proper scaling laws would be of paramount importance to predict the acceleration regimes reachable with forthcoming laser technologies.

The total number of accelerated ions does depend on laser energy and pulse duration. The more energetic and long pulse, the more ions there are in the accelerated beam. Nevertheless short pulse durations may be exploited as well to increase the ion-per-bunch number, since they can achieve higher repetition rates ($\sim$ Hz).

Proton acceleration from very short pulse interactions is also heavily influenced by laser contrast and the level of pre-plasma [70]. In fact, target charging effects due to the escape of hot electrons from the target can also have a significant influence on the proton energy and angular emission [71]. Moreover it is observed to be strongly correlated to target thickness and this aspect will be discussed in the next section 2.1.2.

Finally there have been observed a dependence of the ion emission on the laser polarization [58]. A linear polarization may be either p or s-type: the former has a field component along the target normal, while the latter has not. From the arguments exposed in section 1.3.2, a p polarized pulse is favored in heating electrons during the interaction,

hence giving much more energy to accelerated protons. While a circularly polarized pulse tends to attenuate the oscillating component of the ponderomotive force, which is responsible of the creation of a hot electron population. Hence, as we are going to discuss in section 2.2, the change of laser polarization may appear as one of the effects that allow to switch from one acceleration mechanism to another.

2.1.2 Dependence on target properties

Ion acceleration by intense laser pulses have been observed by using targets of any material in a broad range of thicknesses. Fuchs et al [72] have found protons emitted from conducting materials having a better beam quality with respect to that from insulating materials. This is due to the improved electron flow through the target allowed by the conductors. Ion energy spectrum is strongly dependent on target thickness, in fact an optimal value exists for every combination of laser parameters. In Fig. 2.6(a) we report an example of the proton peak energy dependence on target thickness evidencing the optimal thickness [51], which is not dependent explicitly on laser intensity [70]. As run over in section 2.1.1, the optimal thickness is influenced by the laser pre-pulse: the smaller its duration the smaller the optimal thickness, even remaining larger than the laser wavelength say ∼10-20 μm [70]. Moreover by enhancing the contrast-ratio, the observed trend does not show any optimal value but a constant increase at decreasing target

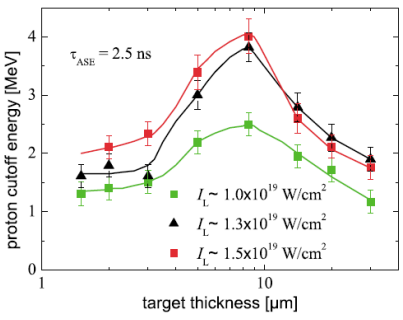

(a) Appearance of an optimal thickness larger than the laser wavelength for shots at low contrast-ratio [70].

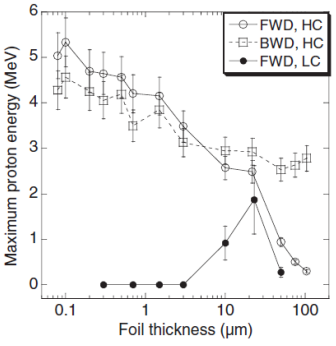

(b) Proton energy increases at decreasing thickness for high contrast-ratio (from [59]).

Figure 2.6: *Maximum proton energy dependence on target thickness in two laser contrast-ratio regimes.*

thickness [59], as shown in Fig. 2.6(b) In the work by Henig et al [73] the adopted thicknesses have reached an optimal value at 30 nm before dropping the proton signal down at 10 nm.
During the last years some efforts in optimizing ion acceleration have dealt with the control of target structure. Schwoerer et al [23] adopted targets micro-structured on the rear surface, obtaining a narrower proton spectrum. On the other hand Willingale et al [74] reported proton acceleration with enhanced energies by adopting low-density targets. In fact a near-critical target may be relativistically transparent at high intensity allowing the laser pulse to propagate through and transfer more energy to electrons. Finally Buffechoux et al [75] used targets with a limited surface area, which force the hot electrons to reflux transversally avoiding their dispersion through the target and giving higher proton energies.

2.2 Acceleration mechanisms

After a brief review on the most relevant experimental observations on laser-accelerated ions, we introduce in this section the physical mechanisms that allowed to explain and predict the results. First let us recall the physics of laser-matter interaction at high intensity discussed in chapter 1. From the expression of the ponderomotive force in equation (1.34) two terms appear: a secular and an oscillating one, the latter contributing to create a hot electron population in the target. We have also observed that for circular polarization and normal incidence the high frequency oscillating term vanishes, so inhibiting the generation of fast electrons. On this basis two distinct acceleration mechanisms may be introduced. The first one, discussed in section 2.2.1, exploits hot electrons as "energy carriers" from the laser to the protons by creating a "sheath" field at the rear surface and is known as Target Normal Sheath Acceleration (TNSA). The second is called Radiation Pressure Acceleration (RPA) and relies on the direct laser-acceleration of ions by means of the secular term in the ponderomotive force. This mechanism will be treated in section 2.2.2.

2.2.1 Target Normal Sheath Acceleration (TNSA)

The TNSA mechanism was introduced for the first time by Wilks et al [76] and nowadays has been explaining most of the ion emission ex-

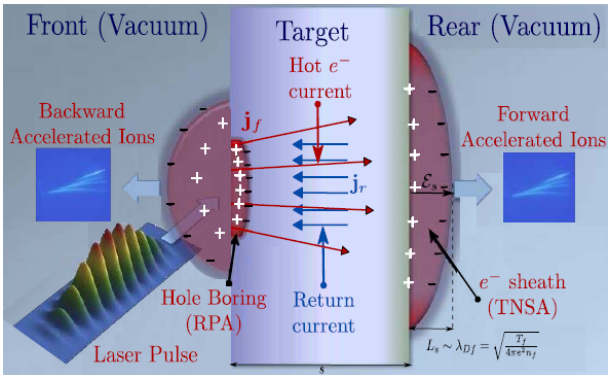

Figure 2.7: *Schematic view of TNSA and RPA mechanisms.*

periments from laser-solid target interaction so far performed within the parameter domain where intensities span 10^{19}-10^{21} Wcm^{-2} and target thicknesses 1-20 μm. As we have seen in detail in section 1.3.2, the interaction of a linearly polarized intense laser pulse with a solid generates a population of energetic *hot* electrons. These electrons are capable to penetrate the target and propagate through it. As they enter the solid, the associated current density $\mathbf{j}_h = -en_h\mathbf{v}_h$ might reach values up to $\sim 10^{12}$ Acm^{-2}. This current must be locally neutralized by a return current $\mathbf{j}_r$ such that $\mathbf{j}_h + \mathbf{j}_r = 0$ (see Fig. 2.7), otherwise charge unbalance would generate electric fields strong enough to stop the hot electrons. In metallic targets the return current is supplied by electrons in the conduction band which are kicked by local field generated by hot electrons. In insulators materials there is not a free electron population as in the metals, but it may be generated by field or collisional ionization as the hot electrons pass through [77]. At such high intensities the hot electrons may acquire mean energies in the MeV regime, then they can easily pass through the target and expand in the vacuum up to distances of the order of λ_D. Since λ_D for such energies extends to some μm, the charge separation at the target rear surface gives rise to longitudinal electric fields in excess of TVm^{-1}. The field depends on the parameters characterizing the hot electron population, namely temperature, number of electrons and divergence [76] and the rear surface density profile [78]. By construction it is maximum in the vicinity of the rear surface so the contaminant layers (water vapor and hydrocarbons) are ionized and accelerated within a few picosecond time. Moreover the longitudinal field is directed along the target normal, allowing the acceleration to happen perpendicular to the rear

surface and with a good collimation. Beam spatial and angular properties depend on the spatial distribution owned by the electron sheath at the rear surface and by target physical properties (resistivity, surface roughness, etc.) which influence hot electron propagation. Protons have the most favorable charge-to-mass ratio, hence can feel the maximum field, while the heavier species start feeling it when it has already been depleted in energy. The sheath nature of the accelerating field is able to justify the exponential shape of the spectrum with a cutoff as it has been observed in most experiments (see Fig. 2.3(a)). Also the observed low conversion efficiency relies on the "three-step process" of energy transfer, i.e. laser-to-electrons and electrons-to-field and field-to-protons. Moreover the presence of an optimal thickness is well explained in the framework of TNSA physics. In fact if target thickness decreases the hot electrons become more and more confined, raising their temperature and hence enhancing proton energy. Therefore when it decreases too much the pre-pulse perturbation is able to reach the rear surface so inhibiting the acceleration process. Improving the contrast the optimal thicknes becomes smaller, till the physical limit demonstrated by Henig et al [73].
There appear possible ways to increase the maximum energy protons acquire in TNSA. One relies on the reduction of target thickness. It has been shown that it allows the penetration of the laser pulse in the relativistic transparency regime, leading to a volumetric energy absorption and a better energy confinement [73]. Another road consists in exploiting the scaling laws of the peak energy with laser properties, in order to enhance energy in a controlled and reproducible way. Finally a third way requires the enhancement of laser absorption by the target, since the more energetic the electrons, the more effective the acceleration process.

2.2.2 Radiation Pressure Acceleration (RPA)

In ultraintense laser-solid interaction an ion acceleration mechanism different from TNSA might be achieved by exploiting directly the pulse radiation pressure, entering in the so-called Radiation Pressure Acceleration (RPA) regime. This can happen either as the intensity raises up to 10^{22} Wcm^{-2} where numerical simulations have showed RPA becomes competitive with TNSA [79,80] or when the hot electron heating mechanism is "switched off" by suppressing TNSA and leaving only RPA as effective mechanism. Following the arguments reported in sec-

tion 1.3.2, the latter case takes place when circular polarization and normal incidence are adopted, so that only the secular term of the ponderomotive force survives [81].
The process can be easily sketch up by a monodimensional representation reported in Fig. 2.8 of ionic ($n_i(x)$) and electronic density profiles ($n_e(x)$) and the accelerating field ($E(x)$). As the laser pulse impinges

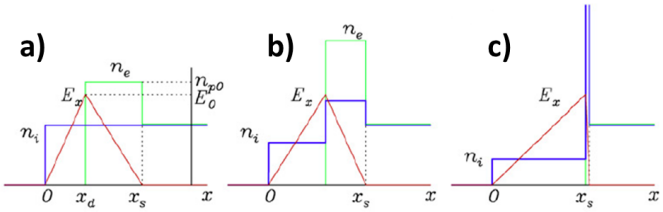

Figure 2.8: *Sketch of the three phases characterizing the monodimensional treatment of hole-boring RPA [82]*

on the surface of an overdense plasma, electrons are pushed forward by the radiation pressure, leaving back a charge depleted region (a). This charge separation generates an electrostatic field which balances exactly the ponderomotive force (b), accelerating than the ions in the compression layer (c). In principle this process may achieve a high laser-to-proton conversion efficiency and monoenergetic spectra. When thick targets are considered the compression layer inject the ions in the solid and the process is known as *hole-boring RPA*. The maximum achievable ion energies are estimated by equating the radiation pressure to plasma momentum flux [83]:

$$\varepsilon_{i,max} = 2m_i c^2 \frac{\Pi}{1 + 2\sqrt{\Pi}} \tag{2.1}$$

where $\Pi = I/\rho c$ is the *pistoning parameter*. For solid densities the process is scarcely effective since only few MeV ions are obtained, which hardly can even cross the target. Thanks to the density dependence shown in equation 2.1, hole-boring becomes more effective in the preplasma where a low density plasma is present. When we are dealing with ultrathin targets, i.e. in the nm range, so that thickness becomes comparable with the compression layer, the electrons are promptly accelerated and the compressed ion layer follows them. The target is then accelerated as a whole and this mechanism is known as *light-sail RPA*. The simplest model describing the light-sail process rely

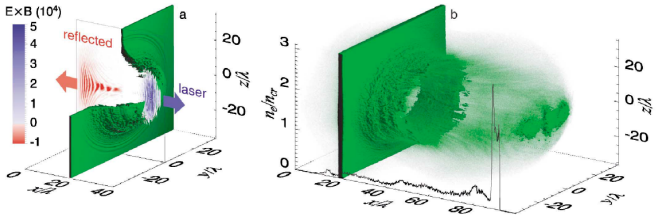

Figure 2.9: *3D visualization of numerical simulations describing the RPDA regime [79].*

on a perfectly reflecting rigid mirror boosted by a light wave [84]. If the laser intensity drops up to $> 10^{23}$ Wcm^{-2}, simulations have revealed that RPA becomes the dominant ion acceleration mechanism and this regime is called *Radiation Pressure Dominated Acceleration (RPDA)* [79, 80]. Here the pulse acts a relativistic piston efficiently accelerating ions and new physical phenomena, such as Rayleigh-Taylor instability and Radiation reaction effects, must be taken into account (see Fig. 2.9).
So far only few experimental observations of RPA process have been reported. Light-Sail acceleration is shown in the work by Henig et al [85] by using 5nm DLC foils. Moreover Palmer et al [86] observed the hole-boring regime by adopting thick H gas-jets.

Part II

Theoretical modeling of Target Normal Sheath Acceleration

3

Comparison among Target Normal Sheath Acceleration theoretical models

In Part I we have discussed the physics of laser-matter interaction at high intensities (Chapter 1) and introduced the topic of laser-driven ion acceleration (Chapter 2). In Part II we are going to cope with the theoretical modeling of the Target Normal Sheath Acceleration mechanism. As we have already seen in Chapter 2, TNSA has been found to well account for most of experimental results so far obtained in laser-ion acceleration. Nonetheless it represents a very complex system to be modeled. In fact there exist strong nonlinearities originating from the large electric fields associated to the considered laser pulses, which force the dynamics of target electrons to be relativistic. Moreover different spatial and temporal scales must be resolved in order to take into account the whole physics of the process. In principle the possibilities to describe theoretically TNSA are two, one relying on (*i*) *numerical simulations*, while the other on a simplified (*ii*) *analytical modeling*.

i The most suitable numerical method to describe plasma dynamics is called Particle-In-Cell (PIC) [87]. The real particles of the system (electrons and ions) are grouped into statistical ensembles called macro-particles. Their dynamics evolves under the influence of self-generated electromagnetic fields, and is determined by the fully relativistic Maxwell-Vlasov system over a space domain divided into discrete cells. The cell size, corresponding to the spatial resolution and the time step of the code are chosen in order to

fit with the spatial and temporal scales characterizing the physical process under study. In many situations values of the order of $\sim c/\omega_p$ and $\sim \omega_p^{-1}$ are adopted, respectively. With PIC simulations a realistic description of the physical behavior of the system under analysis might be achieved if a set of realistic parameters and a good enough resolution can be adopted, regarding for example densities, temperatures and the dimensionality. On the other hand the drawback is that the computational demand of these codes can be really high, especially considering 2 and 3 dimensional geometries. In the last case in particular, the code can be run only exploiting supercomputers which can supply a huge number of operations per second ($>10^{12}$ flop/s).

ii Analytical models are not suitable to give a complete physical description of the system as PIC codes, since the whole process is usually unfolded into separated simplified and more straightforward problems, which can be implemented without involving too expensive numerical computations.

To extensively study TNSA with proper scaling laws describing the external dependencies of system parameters by means of PIC simulations is problematic for the reasons discussed above. Since this represents the goal of the first part of the PhD work the theoretical approach we follow is the analytical modeling. In this Chapter we are going to perform a comparative study involving different models that have been proposed in literature. As a first step we present in Section 3.1 the most significative TNSA models so far reported in the literature and propose a classification ("fluid", "quasi-static" or "hybrid") based on the different time scales treated in each model. Then in Section 3.2 a quantitative comparison among those models will be discussed.

3.1 TNSA analytical modeling

3.1.1 General approach to TNSA modeling

To tackle TNSA mechanism analytically one has to unfold the physical process into simpler subtasks: laser-matter interaction and fast electron generation, fast electron transport, electric field generation and ion acceleration. In order to study the features of the ion beam, the most reasonable step is to focus the attention only on field generation

and ion acceleration process. With this assumption all the other preceding processes might be treated as "boundary conditions", i.e. as a black-box whose output is a plasma with charge state Z and a hot electron population having a well determined temperature and density (see section 1.3.2). A second simplification comes from the choice of the model geometry. Usually the 1-dimensional case is considered, hence assuming the system being homogeneous in the transverse directions (x, y) with respect to target normal z. This corresponds to the study of the electrostatic response of the system without considering any magnetic effect. The modeling concerns a preformed plasma where in general two ionic populations can be considered. The *heavy* one, n_H, is related to the target ions, while the *light* one, n_L, to the accelerated ions, like the surface impurities. Also the electrons are typically divided in two populations: the *hot* n_h and the *cold* one n_c. The former includes the electron fraction which absorb the laser energy and expands through the target as explained in section 1.3.2, having typically $n_h \sim n_{cr} \sim 10^{21}$ cm^{-3}, while the latter includes the target electrons contributing to the return current neutralizing hot electrons expansion inside the target ($n_e = n_h + n_c$). As pointed out in Section 1.3.2, the cold electrons might belong either to the free electron band or to field ionized electrons, depending the target material is a metal or an insulator respectively. Since they have a density of the order of that of solids ($n_c \gg n_h$), the required velocity for current neutralization is small and their temperature is much lower than that of the hot electrons $T_c \ll T_h$, being of the order of MeV. Hence it is reasonable to neglect their dynamics, assuming them as a neutralizing background. The relation for the accelerating potential $\phi(z, t)$ is given then by the Poisson equation:

$$\frac{\partial^2 \phi}{\partial z^2} = 4\pi e \left(n_e - Z n_H - Z n_L\right) \tag{3.1}$$

Electron and ion dynamics might be described either with a kinetic approach, i.e. by the Vlasov equation for the distribution function $f_i(z, t)$ of the i-th species ($i = c, h, H, L$):

$$\frac{\partial f_i}{\partial t} + \frac{\tilde{p}_i}{\tilde{\gamma}_i m_i} \frac{\partial f_i}{\partial z} - q_i \frac{\partial \phi}{\partial z} \frac{\partial f_i}{\partial \tilde{p}_i} = 0, \tag{3.2}$$

where $\tilde{p}_i$ is the kinetic momentum and $\tilde{\gamma}_i = (1 + \tilde{p}_i^2 / m_i^2 c^2)^{1/2}$ the kinetic relativistic factor, or by a fluid approach, i.e. by the momentum $p_i(z, t)$

and mass $n_i(z,t)$ continuity equations:

$$\left(\frac{\partial}{\partial t} + u_i \frac{\partial}{\partial z}\right) p_i = -q_i \frac{\partial \phi}{\partial z} \tag{3.3a}$$

$$\frac{\partial n_i}{\partial t} + \frac{\partial}{\partial z}\left(n_i u_i\right) = 0, \tag{3.3b}$$

where $p_i = m_i \gamma_i u_i$ is the fluid momentum, u_i the fluid velocity field and $\gamma_i = (1 + p_i^2/m_i^2 c^2)^{1/2}$ the kinetic relativistic factor of the i-th species. In order to get the chance to analytically solve the system of equations (3.1)-(3.2) (or (3.1)-(3.3)), one has to take into account the typical time scales of the process. In TNSA in fact there exist at least two main characteristic times, as sketched in Fig. 3.1: the (hot) electron dynamics scale given by $\tau_e \sim \omega_{pe}^{-1} \sim$ fs and the (heavy) ionic dynamic scale identified by $\tau_i \sim \omega_{pi}^{-1} \sim$ ps. Now, there appear two possible ways to approach the modeling [88, 89]. The first takes into account the time interval (a) in Fig. 3.1, i.e. it describes the system for times larger than the ionic dynamics scale ($t \gg \tau_i$). In this way the electron populations and the ions expand as a whole and equations (3.1)-(3.3) are solved for every species. Such models are referred to as "fluid models". The second possible approach is to describe the system within the time interval (b) in Fig. 3.1, i.e. for times larger than the electron dynamics scale but smaller than the ionic one ($\tau_e \ll t \ll \tau_i$). Hence the electron dynamics is active (equations (3.3) for $i = e$), while the heavy ions still remain frozen in the target ($n_H = n_0$, where n_0 is the bulk density). The light ions might then be seen as test charges on the rear surface, feeling the electrostatic field which is calculated by solving the Poisson equation (3.1). This modeling approach is definitely stationary, since the electron cloud is assumed neither to be affected by the ions (light or heavy) flowing through it nor to evolve during the acceleration process. The first condition in particular requires that the number of the ions which are accelerated be much smaller than that of the hot electrons, $N_i \ll N_h$, and that the characteristic time scale of the heavy ion expansion is longer than the light ion acceleration time. Nonetheless, since it is reasonable to believe that the most energetic particles are accelerated during the very first phase of the dynamics, the approach can provide a good simplified description to estimate E_{max}. Such a modeling approach is referred to as "quasi-static". A mixed approach is also possible, where some aspect of the fluid and quasi-static approach are properly combined. These models are classified as "hybrid", since the system is described

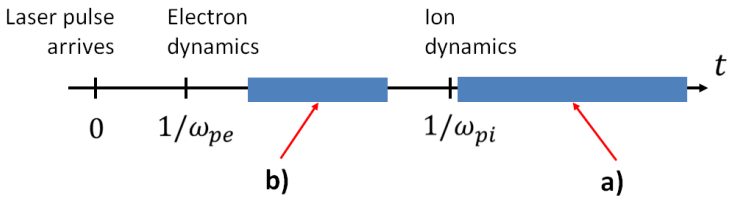

Figure 3.1: *Schematic illustration of the important time scales in the TNSA mechanism. Two time intervals are identified: a) where $t \gg \tau_i$ and b) where $\tau_e \ll t \ll \tau_i$.*

within the time interval (b), but taking somehow into account the effect of the accelerated light (or heavy) ions on the electrostatic field. An important remark is to note that all the possible approaches consider time intervals much larger than τ_e, hence electron dynamics has already developed in such a way to be approximated as they have reached a quasi-equilibrium, with a well defined effective temperature T_h. Then a common simplification to the three approaches comes from describing the hot electron dynamics at equilibrium, hence replacing equations (3.3) for $i = e$ with the Boltzmann model for the self-consistent electron response:

$$n_h(z,t) = n_e \exp\left(\frac{e\phi(z,t)}{T_h}\right), \tag{3.4}$$

where the hot electron density $n_h(z,t)$ is related to the self-consistent electrostatic potential $\phi(z,t)$. Nevertheless this system closure leads the problem to a mathematical singularity, in fact the hot electron density vanishes only when the electrostatic potential goes to $-\infty$. This implies that the ions are accelerated "forever" after the interaction, which means in principle that they might gain an infinite amount of energy running down the potential slope. Of course the experimental observations say that ions are accelerated up to a cutoff energy (see section 2.1) and some reliefs have been adopted to fix this inconsistency. In order to account for the limited maximum energy of ions two paths have been explored in most of the models:

1. To introduce a parameter by assigning a *finite acceleration time* for the ions.

2. To fix a *limit in the hot electrons energy spectrum.*

3. To introduce a *finite spatial extension* for the hot electron cloud.

The reliability of these so-called "truncation mechanisms" will be discussed later on in this Chapter.
In literature several models have been proposed for each one of the categories discussed above and will be discussed in Sections 3.1.2, 3.1.3 and 3.1.4. Since a new generation of laser facilities will be soon available, and it will be possible to investigate a wider range of experimental parameters, the predicting capability of each theoretical model is extremely important to be tested, in order to extrapolate guidelines for the future experiments. Hence in Section 3.2 a comparison between the described models will be performed on the basis of their prediction of an important beam parameter such the maximum ion energy.

3.1.2 Fluid models

As explained in the last Section, in fluid models the solid target is depicted as an expanding plasma. The dynamics of the hot electrons, expanding into vacuum, drives the motion of the ion population. Such a system can be described coupling the fluid equations with the electrostatic equations. Two fluid models have been considered here, the first one is the so-called "Isothermal Expansion Model" by Mora (see Ref. [90] and references therein), and it is widely used to support and interpret experimental data [91]. The target dynamics is described as that of a semi-infinite, single Z-charged ion component plasma expanding into vacuum. The ions are assumed immobile at $t = 0$ with a step-like density distribution centered at the foil-vacuum interface. The electron density follows a Boltzmann distribution (3.4). "Isothermal" means that, while the expansion takes place, T_h remains fixed. The dynamics is governed by electrostatic (3.1) and fluid equations (3.3) (with only one ionic population). A Lagrangian code has been developed to solve the hydrodynamic problem so formulated, and a scaling law for the ion maximum energy is obtained by fitting the numerical results of the simulation:

$$E_{max} = 2ZT_h \ln^2 \left(\tau + \sqrt{\tau^2 + 1}\right) \tag{3.5}$$

with $\tau = \omega_{pi} t_{acc}/\sqrt{2e}$[1], being t_{acc} the ion acceleration time. It is interesting to point out that E_{max} scales as $\ln^2(t_{acc})$, being thus divergent for $t_{acc} \to \infty$ (see dotted line in Fig. 3.2). This aspect is due to the use of Boltzmann relation for hot electrons, as discussed at the end of

[1]Only in this situation the symbol e stands for the Neper number and not for the elementary charge.

previous section. In order to find a finite E_{max}, a truncation criterium is required and according to the present scaling one should provide an estimate for the duration of the acceleration process. In the literature t_{acc} is usually chosen equal to the laser pulse length τ_L or of the same order. For example in Refs. [91, 92] the following value has been proposed:

$$t_{acc} = 1.3\tau_L\,(+78\,\mathrm{fs}), \tag{3.6}$$

where the offset is introduced just for τ_L <150 fs, in order not to underestimate t_{acc} for ultra-short pulses.

The second fluid model we have studied is the so-called "Adiabatic

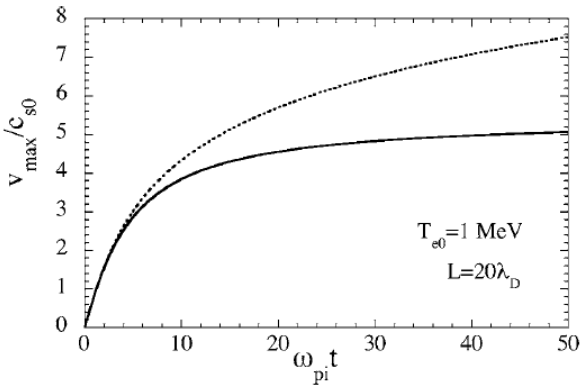

Figure 3.2: *Fastest ion velocity as a function of time. Dotted line corresponds to the prediction of Isothermal model (eq.* (3.5)*). Solid line represents the prediction of Adiabatic Model (eq.* (3.8)*).*

Expansion Model", again by Mora [93]. In this case the target is a finite-thickness L foil of plasma, and the electrons cool down adiabatically during the expansion [93, 94]. In order to consider the evolution of T_h, the energy conservation relation

$$\frac{\mathrm{d}U_e}{\mathrm{d}t} = -\frac{\mathrm{d}U_{ions}}{\mathrm{d}t} - \frac{\mathrm{d}U_{field}}{\mathrm{d}t} \tag{3.7}$$

is coupled with the equations of the previous model (3.1)-(3.3)-(3.4), where U_{ions} is the kinetic energy of the ions, U_{field} is the electrostatic energy of the field and U_e is the thermal energy of the electrons. As in the Isothermal model, the hydrodynamic system is solved with a Lagrangian code, and the resulting ion maximum energy has been fitted

by a scaling law:

$$E_{max} = 2ZT_h \ln^2 \left(0.49 \frac{L}{\lambda_{De}} + 5.4 \right). \tag{3.8}$$

In this case there is no need for an external truncation constraint as in the Isothermal Model, in fact the energy scales as $\ln^2(L)$, in which L is the assumed plasma thickness. Hence, as an effect of the finite energy content in the system, the acceleration is turned off (see solid line in Fig. 3.2).

3.1.3 Quasi-static models

In the quasi-static framework, the electric field setup by the electron sheath is assumed static, and the target ions are divided into two populations. As introduced in section 3.1, the accelerated light ions are studied as test particles under the influence of the electric potential, and the substrate heavy ions are supposed being immobile and maintaining the charge separation.
As representatives of the quasi-static approach Schreiber's [95] and Passoni-Lontano's [96] models have been considered.
In Ref. [95] the expanding hot electron population creates a cylindrical quasi-static cloud in the vacuum, behind the target foil, the dimensions of which are estimated from experimental parameters. The presence of this negatively charged cloud sets up a circular positive surface charge on the rear face of the target, which provides the ion acceleration by means of Coulomb repulsion. The generated electrostatic potential is evaluated on the axis normal at the center of the circular charge distribution, where the most energetic ions are assumed to arise. The resulting ϕ is limited for large distances so in principle the description does not need a truncation criterium. However, in order to integrate the ions' equation of motion with the known potential and to evaluate the maximum energy E_{max} one needs to impose a cutoff time, which is assumed being equal to the laser pulse duration τ_L. The maximum ion energy is then evaluated analytically by inverting the relation:

$$\frac{\tau_L}{\tau_0} = X \left(1 + \frac{1}{2} \frac{1}{1 - X^2} \right) + \frac{1}{4} \ln \left(\frac{1 + X}{1 - X} \right), \tag{3.9}$$

in which $X = \sqrt{E_{max}/E_{i,\infty}}$. $E_{i,\infty}$ is the energy an ion would gain for $t \to \infty$, while τ_0 is a characteristic time. Both can be evaluated directly from the system parameters.

The other quasi-static description, presented in Ref. [96], introduces the idea that the most energetic fraction of the fast electrons can overcome the self-consistent potential barrier and escape the system. Such an assumption introduces a physical truncation mechanism for the acceleration process, the self-consistent potential being now limited so that the model does not require a temporal cutoff. Moreover experimental proofs of the "splitting" of hot electron population into bound and escaping components have been observed in [97, 98], since the interaction produces a maximum value for electron energy. However in order to select the electrons depending on their energy, the Boltzmann relation is not suitable anymore, and the electronic population is described kinetically, assuming a 1D equilibrium distribution function. The electron density can be obtained by integrating it over negative total energies. In such a system E_{max} can be evaluated by means of Poisson equation, but an external parameter, namely the normalized electrostatic potential well inside the target, corresponding to the normalized maximum electron energy φ^*, is required to close its integration. The solution to this merely electrostatic problem has been obtained in the case of a non relativistic electron Maxwell-Boltzmann distribution [99] and by exploiting an ultra-relativistic Maxwell-Jüttner distribution [96]. The development of an exact relativistic solution is among the goals of this thesis and will be discussed more in detail in Chapter 4. We report here only the ion maximum energy scaling which reads:

$$E_{max} = ZT_h \frac{e^{\varphi^*} I(\varphi^*)(\varphi^* - 1) + e^{-mc^2/T_h}\beta(\varphi^*)}{e^{\varphi^*} I(\varphi^*)}. \tag{3.10}$$

φ^* is empirically related with the energy of the laser pulse E_L by means of a scaling law based on experimental data [96]:

$$\varphi^* = 4.8 + 0.8 \ln(E_L). \tag{3.11}$$

Functions β and I depend on the temperature T_h and can be evaluated once φ^* is known (see chapter 4 for more details).

3.1.4 Hybrid models

Both the quasi-static and the fluid approaches turn out to be convenient frameworks to better include some process features better than others. For this reason few "hybrid" models, which try to properly combine the features of fluid and quasi-static descriptions, have been

proposed.
Albright's [100] and Robinson's [101] descriptions are considered.

In Ref. [100] a first approximated inclusion of the ion dynamics effect on the accelerating field is given. The accelerated light ions form a layer assumed of negligible thickness, in which the charge is distributed as a delta-function (see Fig. 3.3(a)). The numerical integration of the Poisson equation (3.1) provides the electrostatic field as a function of the layer position x_L (see Fig. 3.3(b)). Subsequently the median force acting on the layer can be numerically integrated to obtain E_{max}. The electron density is still given by Boltzmann distribution (3.4), and the quasi-static potential is divergent at large distances, but the computed energy converges. The fluid dynamics of the substrate ions ((3.3) with $i = H$), which expand self-similarly for later times, is included in the description as well. Then a scaling law for E_{max} as a function of the light ion layer superficial charge Q_i is obtained:

$$E_{max} = ZT_h \left(3.4q - 2.66\ln(q) - 0.182\ln^2(q)\right) \tag{3.12}$$

in which $q = Q_i/en_{h0}\lambda_{De}$, where n_{h0} is the hot electron density inside the target. This relation is valid in the range $0.003 < q < 0.3$.
Bulk ions fluid dynamics is also a key feature in Robinson's model [101]. In such a description the light ions are treated as test particles, while the accelerating electric field evolves according to the fluid dynamics of substrate heavy ions. The latter are assumed to behave as in the Isothermal Expansion Model proposed in Ref. 3.5, which allow to calculate the position of the substrate z_{sub}. The electro-static field can

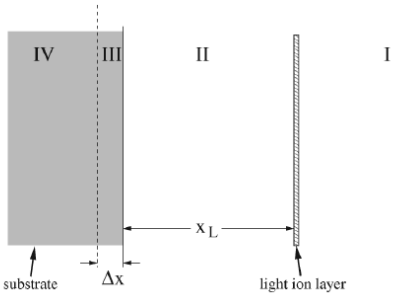

(a) Sketch of the rear of an expanding laser-driven target with a layer of light atoms initially deposited on a heavy substrate.

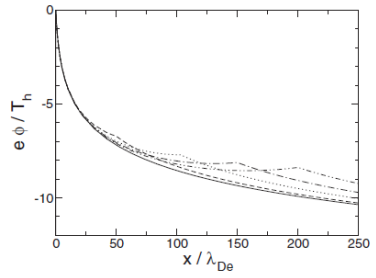

(b) Potential $\varphi = e\phi/T_h$ as a function of distance ξ (scaled to hot electron Debye length) for propagation of a thin ion layer from an infinite-mass substrate.

Figure 3.3: *Sketches illustrating the Albright's hybrid model.*

be calculated analytically depending on z_{sub} This scheme provides a time-dependent electric field that is inserted in the light ions' equation of motion to obtain a prediction of E_{max} via numerical integration.

3.2 Quantitative comparison

3.2.1 Assessment of the parameters needed in the models

For all the models introduced in the previous section, maximum ion energy can be evaluated once the characteristic parameters of the physical system are known. In fact an analytical model treats by definition (see the beginning of this chapter) only a part of the whole physical process. In the present analysis we recover such parameters from experimental papers and then we evaluate the different theoretical predictions in order to compare them with the reported measure of E_{max}. To understand the main features of this analysis all the parameters required for the calculation are now listed (generally speaking, a subset of them is required in a given model, see Table 3.1):

- Laser pulse properties on target, namely the mean intensity I in the focal spot area of radius $r_s = f_s/2$, the energy E_L, the power P_L, the wavelength λ_L and the duration τ_L.
- The target properties, hence the plasma thickness L, assumed equal to the foil thickness, the composition, the ionization features, the number density of substrate ions and the surface charge ${Q_i}^2$.
- The laser-target interaction features, i.e. the energy conversion efficiency η of laser light into hot electrons, and all the hot electron populations properties, the temperature T_h, the density inside the target n_{h0}, the maximum kinetic energy φ^* and the half divergence angle θ_{div} of the beam expanding through the target.
- The ion acceleration time t_{acc} (if required).

This list contains quantities which are not directly accessible in experiments so it is necessary to estimate them. Therefore the data required in order to predict E_{max} can be divided into two categories: *parameters*, which are provided by the papers, and *estimates*, which have to

[2]The charge associated to the light ion layer on the rear surface of the target, once it is completely ionized.

Table 3.1: *The table lists parameters and estimates required by each model in order to evaluate E_{max}. The detailed description of each estimate can be found in the respective reference, indicated in the table. There is no reference relative to Q_i which is evaluated starting from typical experimental quantities.*

Model	Parameters	Estimates
Isothermal Expansion	I, τ_L, λ_L	t_{acc} [91,92], n_{h0} [100], η [102], T_h [47]
Adiabatic Expansion	I, L, λ_L	n_{h0} [100], η [102], T_h [47]
Schreiber	I, P_L, L, τ_L, r_s	t_{acc} [95], θ_{div} [95], η [102]
Passoni-Lontano	I, E_L, λ_L	φ^* [96], T_h [47]
Albright	I, λ_L, Z_{sub}, n_{sub}	n_{h0} [100], Q_i, η [102], T_h [47]
Robinson	I, λ_L, Z_{sub}, n_{sub}, τ_L	n_{h0} [100], t_{acc} [91,92], η [102], T_h [47]

be evaluated from the previous ones by proper scaling laws. In Table 3.1 parameters and estimates relative to each of the theoretical models involved are shown. References about the techniques used to obtain the estimated quantities are given in the table as well. It is important to underline that the use of such estimates introduces some arbitrariness in our analysis, also because the theoretical behavior of quantities as n_{h0}, θ_{div}, T_h, η is still not completely understood, in addition to the fact that their measurement is usually extremely difficult. This inevitably imposes some limitations to the conclusions that one could draw on the basis of a quantitative comparison.

3.2.2 Assessment of the experimental database

To perform the comparison a database containing an extensive collection of published experimental parameters and results has been setup [20, 24, 48, 51, 55, 57, 59, 65, 66, 70, 103], [67, 104–109]. All the details of the experiments can be found in the references. A wide range of laser and target parameters has been considered: the laser intensity range is 3×10^{18}-6×10^{20} Wcm^{-2}, the laser energy range is 0.1-500 J and the pulse duration varies from 30 fs to 1 ps. The targets considered are either metal or insulator foils with thicknesses from 2 to 125 μm. The data contained in such a database have been processed by a Matlab script which implements the calculation of E_{max} for each of the considered models. In Fig. 3.4 such theoretical predictions are plotted against the laser irradiance, together with the experimentally detected energies. Almost all the considered data concern impurity layer proton acceleration. Nonetheless, in order to improve the completeness of

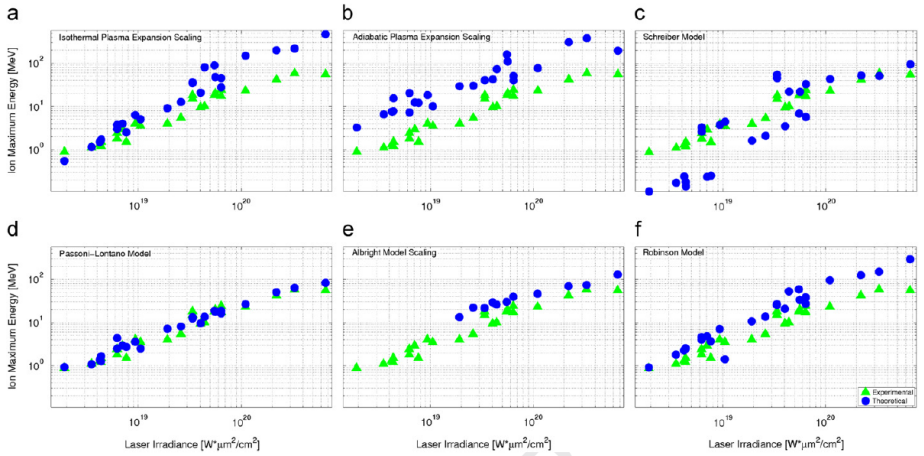

Figure 3.4: *Theoretical predictions of E_{max} for each model, compared to the experimental results. The energy is plotted against the laser pulse irradiance in double logarithmic scale. Some predictions relative to Albright's description are missing because the parameters fall outside the validity range of the scaling law* (3.12)

the database, also the C^{5+} ion acceleration reported in Ref. [20] has been included. In this case the value for E_{max} refers to the energy per nucleon of the accelerated ions.

3.2.3 Results and discussion

In order to give a quantitative support to the evidences in the figure, we report the values of $\langle \Delta_{\%} \rangle \equiv \langle |E_{theo} - E_{exp}|/E_{exp} \rangle$, namely the mean percentage difference between experimental and theoretical energies. For the Isothermal fluid model predictions we have computed $\langle \Delta_{\%} \rangle$ =175%, while for the Adiabatic Model $\langle \Delta_{\%} \rangle$ =441%. Regarding the quasi-static descriptions, Schreiber's model gives $\langle \Delta_{\%} \rangle$ =73% and Passoni-Lontano's $\langle \Delta_{\%} \rangle$ =26%. Finally, hybrid descriptions of Albright and Robinson provide predictions for which $\langle \Delta_{\%} \rangle$ =126% and $\langle \Delta_{\%} \rangle$ =134%, respectively.
In the light of the obtained results it is interesting to discuss some of the issues arising from the present analysis, in particular those related to the estimates listed in Table 3.1. The evaluation of t_{acc} (required by models [90, 95, 101]) represents a critical point in TNSA modeling. In fact the present theoretical understanding of the process does

not provide a firm way to evaluate this quantity. As we have already mentioned, in the literature t_{acc} is usually chosen proportional to laser pulse temporal length τ_L. For our calculation we estimated t_{acc} by means of eq. (3.6), except for Schreiber's description in which we adopted $t_{acc} = \tau_L$, as suggested in Ref. [95]. From a theoretical point of view, the idea that $t_{acc} \propto \tau_L$, is not completely justified, since the persistence of the electric field should be more directly related to the electron and ion properties, and the accelerating force is not supposed to turn off immediately after the laser pulse is reflected by the target. The consequences of such a choice for the acceleration truncation can be observed in Fig. 3.4(a), (c) and (f). As pointed out in Ref. [92], for laser pulses up to 100 fs, the acceleration time is longer than the pulse temporal length. An offset time is thus introduced in eq. (3.6) in order not to underestimate the duration of the process. In Fig. 3.4(c) most of the underestimated predictions have τ_L <100 fs. If we use eq. (3.6) also for this model this underestimate is reduced, but long pulse predictions are overestimated. In fact it seems reasonable that a large pulse duration (∼ps) corresponds to a time that is greater than the acceleration time of the most energetic ions. This statement is supported by Isothermal and Robinson's predictions for long pulses experiments (corresponding to $I\lambda^2 > 10^{20}$ Wμm^{2}cm^{-2} in Fig. 3.4), which overestimate E_{exp}. The results displayed in Fig. 3.4(a), (c) and (f) are thus strongly affected by t_{acc} calculation, and a more realistic approach to evaluate this quantity could improve the predicting capability of the models in Refs. [90, 95, 101]. As mentioned in section 3.1.2, the Adiabatic Model [93] avoids the problem of estimating t_{acc}, but it can be seen in Fig. 3.4(b) that it provides the worst predictions for E_{max}. This might show that the adiabatic cooling of the electron population does not represent the correct way to explain the turnoff of the acceleration in TNSA. In fact the thickness dependent scaling provided in eq. (3.8) does not agree with analogous experimental scalings reported in [51, 70]. We remark that in this case the thickness of the plasma L fixes the energy available for ion acceleration. In fact one can impose the balance between laser energy absorbed by the target and the hot electrons' mean kinetic energy in a relation involving the quantities T_h, n_{h0}, η and L (see Ref. [100]). If three of these parameters are known the remaining can be evaluated. So it is possible to calculate an effective plasma thickness starting from the estimates and parameters in Table 3.1. However, this effective thickness tends to be larger than the real target thickness and thus it leads to larger energy

estimates. We also underline that in the literature the mean kinetic energy $\langle K_e \rangle$ of the electrons in the balance relation just mentioned is taken equal to T_h [100]. Nonetheless, a relativistic form for $\langle K_e \rangle$ can be used (see Ref. [110]), and this can lead to more precise estimates.
The predictions of Passoni-Lontano's model show a remarkable agreement with a wide range of experimental results. This supports the validity of the scaling law proposed in Ref. [96] for bound electrons' maximum kinetic energy φ^* (3.11) as a connection between laser parameters and acceleration process. Giving a satisfactory theoretical explanation to this behavior represents an interesting challenge in TNSA theoretical study. Another problematic quantity is the divergence half-angle of the electron beam θ_{div}, which has been evaluated according to Ref. [95], on the basis of some experimental measurements. Electron divergence is in fact one of the most discussed topics in electron transport study for fast ignition and a reliable estimate of θ_{div} is not available yet [111]. The fact that Schreiber's model needs such an angle to provide E_{max} can affect its predicting capability in a number of cases.
On the basis of these results we can thus conclude that the quasi-static models are more suitable for the prediction of ion maximum energy. The hybrid approach, which in principle should lead to a more complete description of the TNSA, shows a worst predicting capability in both the considered models [100, 101]. This is probably due to the limits of the quasi-static aspects in these descriptions. The number and the uncertain reliability of the estimates on which theoretical predictions are based turn out to be a crucial factor. We can notice from Fig. 3.4 and Table 3.1 that the descriptions which rely on the fewest estimates provide the best agreement with experimental data. It would be thus recommendable to reduce the arbitrariness introduced in the analysis by the use of too many estimates. This can be achieved extending the present knowledge of some important aspects in TNSA physics as laser-electrons coupling or hot electron transport.
In Chapter 4 we will present a theoretical development in the framework of the quasi-static modeling, in order to predict simple scaling laws linking the maximum ion energy to some laser parameters, as the intensity.

4

Quasi-static modeling of Target Normal Sheath Acceleration

The overview and comparison between different models developed in Chapter 3 indicate which can be the most suitable approach to properly estimate an important ion beam parameter like the maximum ion energy. We have shown the quasi-static approach being the best one in modeling maximum ion energy, as it suitably focuses the attention only on the first stages of the acceleration process. The representative models we have discussed for the quasi-static category are Schreiber's and Passoni-Lontano's ones. While the former is not really kine in reproducing the experimental data mainly because it requires many input parameters not easy to estimate, the latter shows the best predicting capability with a relatively small number of inputs which are easier to be found experimentally (see Section 3.2). Moreover the Passoni-Lontano's approach adopts a more physical truncation criterium for the hot electron density, hence for the acceleration process, by fixing a maximum energy in the electron spectrum. This assumption has been also observed to hold experimentally as can be noticed in Fig. 4.1, reporting a typical measured hot electron spectrum. In the present chapter we aim to further investigate this modeling approach. First we present in Section 4.1 an analytical development leading to a relativistically correct solution of Passoni-Lontano's model, hence extending the approximated solutions published so far in literature. Then in Section 4.2.1 we will exploit its simplicity and reliable implementation to determine and interpret experimentally relevant scalings of maximum ion energy on laser parameters, as for example on the

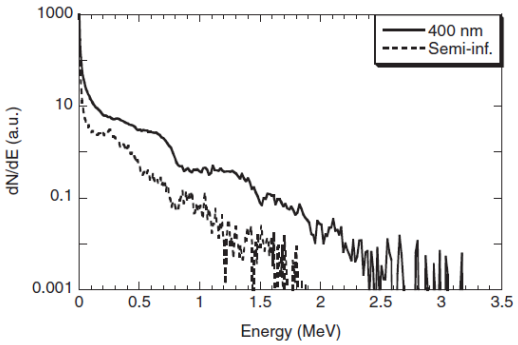

Figure 4.1: *Typical hot electron spectra measured during an ion acceleration experiment [59].*

different ways to obtain a change in laser intensity. In Section 4.2.2, we will also compare the scalings obtained with the model to those coming from 2D Particle-In-Cell numerical simulations.

4.1 The exact relativistic solution of Passoni-Lontano model

As briefly explained in Section 3.1.3, the Passoni-Lontano model adopts a quasi-static approach to tackle TNSA physics. The laser-target interaction is referred to as a boundary condition for the generation of a population of hot electrons expanding through the target. This electrons are described at equilibrium by a kinetic distribution function, allowing to discriminate the most energetic part of the spectrum from the other which contributes actively to the electrostatic field setting up (so-called *bound* electrons n_b). The effects of the cold electron population with a variable thermal energy have been investigated in several publications [112]. For the sake of simplicity, in the following, we will consider $n_c = n_{0c} = const$ (as discussed in Section 3.1). As far as the high energy part of the accelerated ion spectrum is concerned, this is a reasonable approximation. As explained in Section 3.1.3, the heavy ions are assumed immobile on the time scale of interest with constant density equal to the bulk n_0, while the light ions are considered sufficiently few to neglect their effect on the evolution of the electrostatic potential, which in this limit is given by specifying (3.1) as follows:

$$\frac{\partial^2 \phi}{\partial z^2} = 4\pi e \left[n_b + n_{0c} - Z n_0 H(-z) \right], \tag{4.1}$$

where H is the Heaviside function. In order to close the system, the electron density must be properly related to the self-consistent potential. Hot electrons, as said in Section 3.1.3, are assumed to follow a 1D, single temperature Maxwell-Jüttner relativistic electron distribution function (edf) in the self-consistent electrostatic potential $\phi(z)$ [113]:

$$f_h(z,p) = \frac{\tilde{n}}{2mcK_1(\xi)} \exp\left(-\frac{W+mc^2}{T_h}\right) \tag{4.2}$$

where $W = mc^2(\gamma-1) - e\phi$, T_h is the hot electron temperature, $K_1(\xi)$ the MacDonald function of first order and argument $\xi = mc^2/T_h$, where m is the rest electron mass, e the modulus of the electron charge, c the speed of light, $\gamma = (1+p^2/m^2c^2)^{1/2}$, and the edf has been normalized to the density $\tilde{n}$ by integrating over $-\infty < p < +\infty$. The negatively charged source in the Poisson equation is now given by the bound electron charge density:

$$n_b(z) = \int_{W<0} f_h(z,p)\mathrm{d}p \tag{4.3}$$

where the integration extends over the negative energies only. In terms of momentum variable the condition $W < 0$ reads:

$$\begin{aligned} &\frac{m^2c^4+p^2c^2}{T_h^2} < \left(\frac{e\phi}{T_h} + \frac{mc^2}{T_h}\right)^2 \\ &\Rightarrow |p| < \sqrt{(\varphi+\xi)^2 - \xi^2} \equiv \beta(\varphi), \end{aligned} \tag{4.4}$$

where the dimensionless variables $\varphi = e\phi/T_h$ and $p = pc/T_h$ have been defined. Substituting eq. (4.4) and (4.2) into (4.3) and taking into account the even parity of edf, one obtains the final expression for the bound electron density:

$$n_b = \frac{\tilde{n}T_h}{mc^2K_1(\xi)} e^{\varphi} \int_0^{\beta(\varphi)} e^{-\sqrt{\xi^2+p^2}}\mathrm{d}p. \tag{4.5}$$

After introducing the further dimensionless variable $\zeta = z/\lambda_D$, where $\lambda^2 = mc^2K_1/(4\pi\tilde{n}e^2)$, and using equations (4.1) and (4.5), the resulting equation for the self-consistent potential is

$$\frac{\mathrm{d}^2\varphi}{\mathrm{d}\zeta^2} = e^{\varphi} \int_0^{\beta(\varphi)} e^{-\sqrt{\xi^2+p^2}}\mathrm{d}p - \frac{(Z_H n_{0H} - n_{0c})}{\tilde{n}} \xi K_1(\xi) H(-\zeta) \tag{4.6}$$

Approximated versions of this equation have been considered in the literature, assuming the non-relativistic [99] and ultra-relativistic [96]

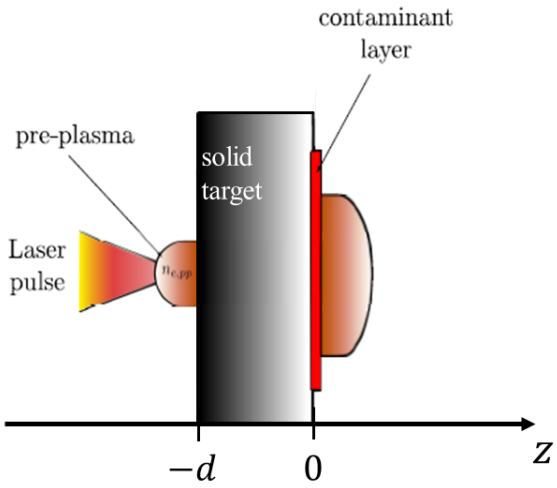

Figure 4.2: *Sketch of the monodimensional geometry exploited by the Passoni-Lontano model. The dependencies of all the quantities are collapsed on the z axis only.*

limits of eq. (4.2), respectively. In the following we will develop the exact solution of equation (4.6) [114].

Let us consider at first the solution in the region $\zeta > 0$ outside the target, i.e. in the vacuum behind its rear surface (see Fig. 4.2). Here eq. (4.6) reads

$$\frac{\mathrm{d}^2\varphi}{\mathrm{d}\zeta^2} = e^{\varphi} I(\varphi), \tag{4.7}$$

being $I(\varphi) = \int_0^{\beta(\varphi)} e^{-\sqrt{\xi^2+p^2}} \mathrm{d}p$. Now we take each member of (4.7) times the first space derivative of the potential $\dot{\varphi}$ and impose that a $\tilde{\zeta}$ exists such that $\varphi(\tilde{\zeta}) = \dot{\varphi}(\tilde{\zeta}) = \ddot{\varphi}(\tilde{\zeta}) = 0$. Hence (4.7) can be integrated once between $\tilde{\zeta}$ and ζ, obtaining the electric field outside the target:

$$\frac{\mathrm{d}\varphi}{\mathrm{d}\zeta} = -\sqrt{2}\left(e^{\varphi} I(\varphi) - e^{-\xi}\beta\right)^{1/2}. \tag{4.8}$$

After a second space integration between 0 and ζ the electrostatic potential $\phi(\zeta)$ in the vacuum is obtained implicitly

$$\int_{\varphi_0}^{\varphi(\zeta)} \frac{\mathrm{d}\hat{\varphi}}{\left(e^{\hat{\varphi}} I(\hat{\varphi}) - e^{-\xi}\beta\right)^{1/2}} = -\sqrt{2}\zeta \tag{4.9}$$

where $\varphi_0 = \varphi(0)$ is the potential at the solid-vacuum interface, on which the solution depends. This parameter might be calculated by

solving the electrostatic problem inside the target (i.e. for $\zeta < 0$) and then imposing the continuity of the electric field at $\zeta = 0$. The complete equation (4.6) inside the target reads

$$\frac{\mathrm{d}^2\varphi^<}{\mathrm{d}\zeta^2} = e^{\varphi^<} I(\varphi^<) - B, \tag{4.10}$$

where $B = [(Z_H n_0 - n_{0c})/\tilde{n}]\xi K_1(\xi)$. Let us assume that well inside the target the plasma to be locally quasi-neutral, hence that $B = e^{\varphi^<} I(\varphi^<)$ holds. Then at a position $-\zeta_d = -d/\lambda_D$ located well inside the target, with d of the same order of target thickness, $\dot{\varphi}^< = 0$ and $\varphi^<(-\zeta_d) \equiv \varphi^*$ hold, being φ^* the maximum potential. Adopting the same integration procedure and imposing the inner boundary condition we find the electric field

$$\begin{aligned}\frac{\mathrm{d}\varphi^<}{\mathrm{d}\zeta} = &-\sqrt{2}\Big(e^{\varphi^<} I(\varphi^<) - e^{-\xi}\beta - B\varphi^< - \\ &+ e^{\varphi^*} I(\varphi^*) + e^{-\xi}\beta^* + B\varphi^*\Big)\end{aligned} \tag{4.11}$$

where $\beta^* = \beta(\varphi^*)$. By imposing the continuity of the electric field at $\zeta = 0$, hence equating (4.8) and (4.11), we can obtain a relation between φ_0 and φ^* (already reported in eq. (3.10)):

$$\varphi_0 = \frac{e^{\varphi^*} I(\varphi^*)\,(\varphi^* - 1) + e^{-\xi}\beta^*}{e^{\varphi^*} I(\varphi^*)}. \tag{4.12}$$

The electrostatic potential is fully determined from eqs. (4.9) and (4.12) once φ^* is given. The quantity φ^*, already discussed in Section 3.1.3, represents the inner boundary condition of the normalized electrostatic potential (hence the maximum value). Furthermore by imposing the total relativistic energy W being negative, one obtains $K_e/T_h < \varphi\varphi^*$, and $\epsilon_{e,max} = K_{e,max}/T_h$, corresponding also to the maximum kinetic electron energy of the laser produced trapped electrons. It depends on the physics of the laser-solid coupling and it can be either related to experimental data, or taken from suitable numerical simulations, or determined on physical grounds. In this work, we are presenting results in which use is made of the scaling law proposed in [96] and reported already in eq. (3.11):

$$\varphi^* = \epsilon_{e,max} \approx 4.8 + 0.8 \ln\left[E_L\,(\mathrm{J})\right]$$

This scaling is suitable to investigate TNSA in most common experimental conditions, in particular, those in which targets with thickness

in the multi-μm range are used and the optimal thickness conditions with respect to laser contrast are achieved (see Section 2.1.2).
If a test ion of charge Z is placed at rest at $\zeta = 0$, it is accelerated up to a maximum kinetic energy $E_{max} = Ze\phi(0) = Z\varphi_0(\varphi^*)T_h$. By adopting the ponderomotive scaling (1.35) to estimate T_h and considering the scaling law (3.11) for φ^*, the TNSA maximum ion energy turns out to be a function of laser energy and intensity. In the general case, the integrals contained in eqs. (4.9) and (4.12) can be very easily solved either with any quadrature method or with the direct use of standard mathematical software. Besides the maximum ion energy, other interesting quantities, like the high-energy part of the ion energy spectrum and the extension of the hot electron cloud (or, equivalently, the extension of the accelerating field) can be obtained for comparison with experimental data. In this context, we note that the target properties, which can influence and modify the features of the laser-solid interaction (see Section 2.1.2), are here indirectly contained in the estimate of φ^*.
It has been proven in [115] that, by solving the equation of motion of a test charge Z in the electrostatic potential given by (4.9), the characteristic time scale of the heavy ion expansion is longer than the light ion acceleration time. In fact the typical proton ($Z = 1$) acceleration time has been found to be of few tens of femtoseconds, hence smaller than the heavy ions dynamics time scale. This constitutes a further confirmation the quasi-static approach is suitable for the assessment of maximum ion energy, being all its assumptions a posteriori confirmed.
In the next section we will exploit the results of this quasi-static model to interpret experimental scalings of maximum ion energy with laser parameters and to compare the predicting capability of such scalings on the basis of numerical simulations. In particular we will focus the attention on the non trivial issue of the maximum ion energy dependence on laser irradiance, already discussed in Section 2.1.1.

4.2 TNSA scalings: theoretical interpretation of experimental and numerical data

The effective dependence of the maximum ion energy on the laser irradiance in TNSA experiments represents one of the most interesting and challenging issues. In Fig. 2.4(b), as already discussed in Section 2.1.1, a collection of a large number of experimental data evidences

that different, non-obvious scalings of the maximum proton energy with the laser irradiance seem to emerge. In particular, an effective almost linear relation is evidenced as characterizing a significant number of results, achieved in various laser facilities. A further, very interesting point is that it has been clearly shown that different maximum ion energies have been produced so far using pulses with the same laser irradiance but with different pulse energy. So far no satisfactory explanations for these facts have been provided and the underlying physics does not clearly emerge. In the following we have used the TNSA theory discussed in detail in Section 4.1 to investigate this intriguing issue, both by interpreting experimental data sets (Section 4.2.1) and by drawing both analytical and numerical PIC scaling laws (Section 4.2.2). To implement the model we simulate the laser pulse as uniformly containing the amount of energy E_L in the spot f_s of a temporally rectangular-shaped pulse, so that $I_L = 4E_L/(\tau_L \pi f_s^2)$.

4.2.1 Comparison with experiments

In this section we tackle the issue of maximum ion energy dependence on laser intensity from experiments reported in the literature. First let us consider the data set reported in Fig. 4.3, where the maximum proton energy from laser-irradiated targets, for a number of experiments performed on different laser systems, is shown as a function of the pulse irradiance. The experimental values are indicated with blue squares. Also, the fitted effective dependence of the experimental proton energies on the irradiance is plotted (dashed green curve). Actually, the scaling is almost quasi-linear for these data, which refer to pulses with quite different properties: in particular, pulse durations and energies ranging from 40 fs to 1 ps and from 0.1 to 50 J are present, respectively. The corresponding theoretical expectations are indicated with red circles. It can be seen that the observed dependence can be nicely reproduced. We can then interpret the physical situation as the result of the combined, convoluted dependence of the maximum proton energy on both pulse irradiance and pulse energy. In order to draw clear conclusions about both the different possible scaling laws in TNSA and the corresponding underlying mechanisms, dedicated experimental parametric investigations using exactly the same controlled conditions would be greatly valuable. In this connection, it has to be realized that, when results coming from different experiments and performed on different laser facilities are compared, the main quantities

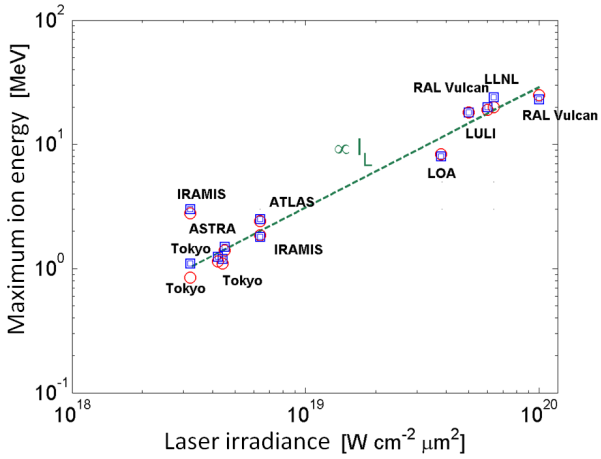

Figure 4.3: *Maximum proton energy from laser-irradiated targets for experiments on different laser systems as a function of the laser pulse irradiance. Experimental values are shown by blue squares, the corresponding theoretical expectations by red circles. Also, the fitted effective dependence of the experimental proton energies on the irradiance is plotted (dashed green curve).*

that characterize the laser pulse, namely its maximum energy E_L, minimum duration τ_L, focal spot f_s, irradiance $I\lambda^2$ and contrast can be very different from each other and, moreover, are not independent parameters.

The second case study jointly considers data from two experimental campaigns, one performed at CEA-IRAMIS Saclay ("Saclay" in the following) [59, 116] and one at Dresden-Rossendorf ("Dresden") [66]. Different motivations justify this choice. First of all the two data sets are consistent/comparable in the sense that they come from very similar laser systems (developed by Amplitude-Technologies [5], λ =0.8 μm) having ultra-short pulse duration (around 25-30 fs), multi-TW pulse power (100-150 TW) and incident angle on target of 45°. Furthermore many maximum proton energy experimental points are available from those sets, which are obtained through a well defined parametric scan where the combined dependence of maximum ion energy on laser energy and intensity is studied by varying laser energy while keeping other parameters fixed. More in detail, in Saclay experiment a double plasma mirror (DPM) is installed in order to improve the contrast till $\sim$ few 10^{13}. Thanks to this device protons have been accelerated in backward direction from the front surface of a very thick plastic target; in such ultra-high contrast conditions no significant differences

between forward and backward acceleration have been observed [59]. On the other hand DPM causes both a reduction of the effective power on target, from nominal 100 to 34 TW, and a not well-shaped focal spot on target. For this reason the correspondence between power and intensity on target has been estimated by the authors by assuming pulse energy being uniformly contained inside a plain surface area $S \sim 100\mu\text{m}^2$ [116], corresponding to a circular spot with a radius $r_s \sim 5.6\mu\text{m}$. In this case we shall speak about mean intensity, reaching at most 3×10^{19} Wcm^{-2}. In Dresden experiment, no DPM is present and contrast ratio is $\sim$ few 10^{10}. In this case protons have been detected in forward direction from rear surface. Targets consist of 2-5 μm thick metal foils, while intensity spatial profile of the pulse has a well defined, slightly ellipsoidal Gaussian shape with an average full-width half-maximum FWHM of 3 μm (corresponding to a waist $w = FWHM/\sqrt{2\ln 2}$ ~2.7 μm) and a peak value around 10^{21} Wcm^{-2}. In Fig. 4.4(a) the two data sets (blue dots from Saclay and red dots from Dresden) have been reported as a function of pulse power (from 1 to 100 TW). It is pretty clear that the experimental points show a common trend with respect to laser power (see Fig. 4.4(a). Taking into account the similarity between the two laser systems and maximum proton energy data, it is reasonable to assume also in Dresden experiment that pulse spatial profile can be reduced from a Gaussian shape to an effective uniform one with a diameter $f_s = 2r_s$ =11.3 μm. The

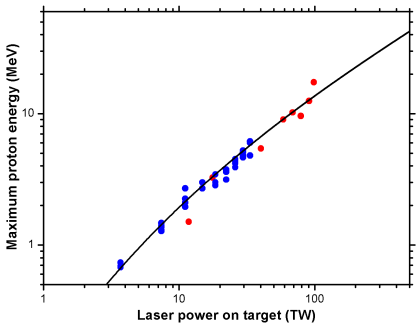

(a) Maximum proton energy in MeV as a function of laser pulse power.

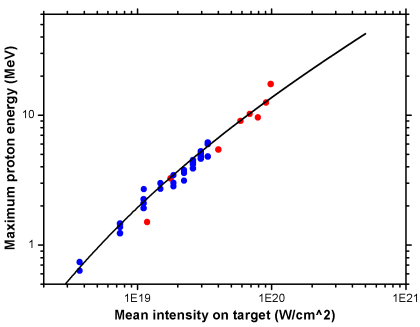

(b) Maximum proton energy in MeV as a function of laser pulse intensity.

Figure 4.4: *Solid line represents model prediction calculated with varying power and intensity, pulse duration and effective focal spot kept fixed at τ_L =25 fs and f_s =11.3 μm. Dots correspond to experimental measurements: in particular blue ones are obtained at Saclay facility [59, 116] while red ones at Dresden facility [66].*

combination of Saclay and Dresden data sets establishes a well defined ensemble of experimental points regarding ultra-short pulses (∼30 fs), where laser intensity changes uniquely because of a corresponding pulse energy content variation (see Fig. 4.4(b)). Furthermore this data ensemble covers with continuity power and mean intensity ranges 1-100 TW and $4 \times 10^{18} - 10^{20}$ Wcm^{-2}, respectively.
In order to obtain the theoretical scaling with the relativistic Passoni-Lontano model, pulse duration and diameter corresponding to an effective uniformly distributed intensity profile are fixed: coherently with experimental parameters we choose $\tau_L = 25$ fs and $f_s = 11.3$ μm, respectively. In Fig. 4.4 the two data sets and the model prediction (blue solid line) have been reported on the same plot. In the light of this result we can reasonably state that, at least in the ultra-short pulse duration regime (tens fs) and for the considered range of laser parameters, "universality" of the TNSA is experimentally demonstrated. Firstly we see that data obtained from the rear side with optimum thickness targets (depending on pre-pulse properties) follow the same scaling of data achieved in front-side acceleration with ultra-high contrast ratio. Furthermore, the scaling of maximum proton energy is quasi-linear with respect to pulse power in the whole 1-100 TW range (Fig. 4.4(a)). In the present case pulse power is directly proportional to intensity, focal spot and duration being fixed for each case, thus also scaling with intensity is quasi-linear (Fig. 4.4(b)). This is in agreement with previous results reported in Fig. 4.3 and Refs. [116, 117]. In Fig. 4.4(b) the capability of the model to reproduce experimental scalings is evident, thus confirming the fundamental role played by laser energy and intensity as key parameters to correlate maximum proton energy to pulse properties. The observed quasi-linear dependence can thus be interpreted as a result of the combined convoluted dependence of maximum proton energy on pulse intensity and pulse energy.

4.2.2 Comparison with Particle-In-Cell simulations

After the discussion on experimental data sets in previous section, it is interesting to consider in more detail the problem of evaluating the relative role of laser parameters in acceleration process. To achieve this goal we make use of a combined theoretical study, joining analytical and numerical approaches [118]. The former relies on the relativistic Passoni-Lontano model discussed in section 4.1, while the latter exploits the 2D-PIC code `ALaDyn` [119–121], a relativistic, fully self-

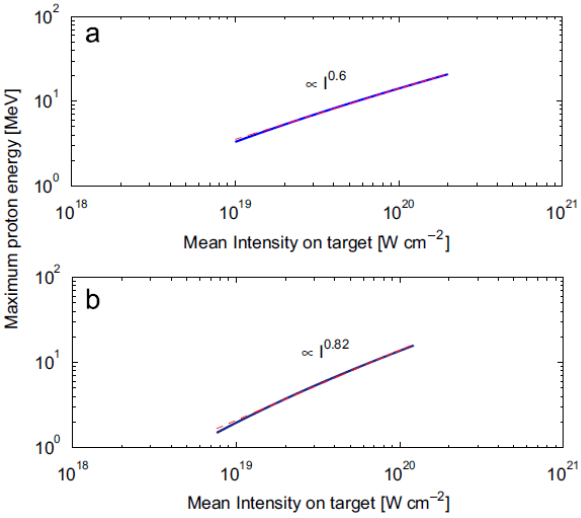

Figure 4.5: *Theoretical predictions of maximum ion energy dependencies on laser intensity for two different conditions. (a) Scaling obtained with fixed power and duration at 122 TW and τ_L=25 fs, and varying intensity between 10^{19} and 2×10^{20} Wcm^{-2}. (b) Scaling obtained with varying power in the range 7-122 TW and fixed duration and focal spot at τ_L=25 fs and f_s=11.3 μm. In both graphs scalings are fitted with the corresponding power law.*

consistent electromagnetic PIC code. Two possible configurations are considered (similar to those investigated in recent experiments, see for example in Refs. [22, 69] and the discussion in section 2.1.1). In the first case, pulse energy is kept fixed while variation in intensity is due to a corresponding change in focal spot. In the second case both pulse duration and focal spot are kept fixed: in these conditions, variation in intensity is due to a corresponding change in pulse energy. As a consequence, each simulated pulse corresponds to a specific and different combination of pulse energy and intensity: this is the situation already described with reference to experimental data previously discussed. In Fig. 4.5we report model predictions: in Fig. 4.5(a) pulse power and duration are kept equal to P_L=122 TW and τ_L=25 fs, intensity variation being due to a corresponding variation of the focal spot. In Fig. 4.5(b) pulse duration and focal spot are fixed to τ_L=25 fs and f_s=11.3 μm, respectively, while intensity is varying with pulse energy. The obtained theoretical scalings lead to different power laws in the two cases: quasi-radical in the former, quasi-linear in the latter. In Fig. 4.6 2D-PIC simulations referring to analogous configurations are pre-

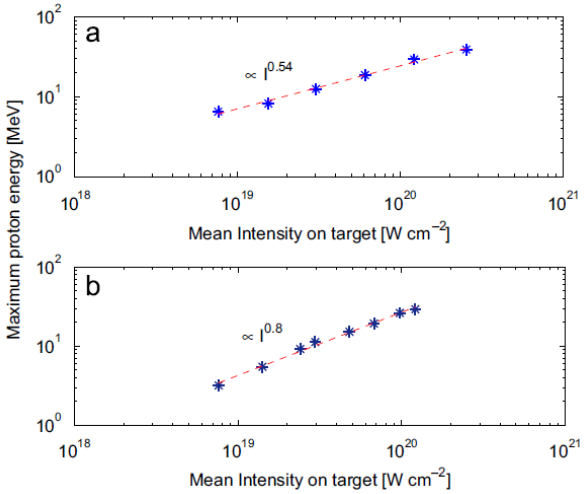

Figure 4.6: *Scalings of maximum proton energy with laser intensity obtained with 2D-PIC simulations. Intensity was varied in two alternative ways. (a) Pulse power and duration were kept fixed at P_L=122 TW and τ_L=25 fs, while intensity and the waist of Gaussian spot profile were varied simultaneously. (b) Pulse power was let to vary from point to point, keeping pulse spatial waist and duration fixed at w=3 μm and τ_L=25 fs. Both scalings are fitted with a power law (dashed line) whose strength is reported.*

sented. First of all it is worth noting that in our simulations maximum proton energies overestimate corresponding experimentally measured values. This fact could be expected for at least two reasons: one deals with the dimensionality of the PIC code, since a 2D description does not take into account electron expansion in the neglected dimension, leading to an underestimation of the attenuation rate of the accelerating field with respect to time. The second motivation is related to the fact that simulations are performed using a 0.5 μm thick target: this implies more energetic proton spectra (as shown in Ref. [59]). In our PIC simulations intensity is given by a, the normalized peak intensity of the Gaussian profile. In order to compare PIC scalings with model predictions over the same abscissa, it is necessary to estimate for each a a corresponding mean intensity. Given that, as explained in section 4.2.1, we associated to the spot of Dresden experiment (with waist w=2.7 μm) an effective uniform one with radius r_s=5.6 μm, it is reasonable to reduce PIC simulated spot (with waist w_0=3 μm) to the same uniform spatial profile as well. Peak intensities become "mean values" through the relation $I_m = \nu I_p$, where $\nu = w_0^2/2r_0^2$ is a fac-

tor relating uniform and Gaussian intensity profiles corresponding to same power and $I_p(\mathrm{Wcm}^{-2}) = (a/\lambda_{\mu\mathrm{m}})^2 \cdot 1.38 \times 10^{18}$. In Fig. 4.6(a) pulse power and duration were kept fixed at P_L=122 TW and τ_L=25 fs, while normalized intensity a and spot waist w were changed coherently in the ranges 10-20 and 3-6 μm, respectively. In Fig. 4.6(b) power was varied between 7 and 122 TW, keeping duration and spot waist equal to τ_L=25 fs and w=3 μm, respectively. Comparing the scalings predicted by model and simulations qualitative agreement in the considered range of parameters is remarkable. Quantitative agreement between the two predictions is influenced by the previously described overestimation affecting simulations. It is possible to extract an almost constant scale factor $\sim$2 between model and PIC scalings. These results strongly support the physical picture at the basis of TNSA.

Part III

Nanoengineered targets for laser-driven ion acceleration

5

Towards enhanced laser-driven ion acceleration

The optimization of laser-driven ion acceleration constitutes the leading thread of this PhD thesis. In Part II we have discussed the scaling laws relating the maximum energy of the accelerated ions to laser properties through a theoretical modeling of the TNSA. In particular the the dependence of maximum ion energy on laser irradiance has been handled in detail. These results might in principle be guidelines for the design of future experiments exploiting a further regime of laser performances. It is alternatively possible to improve the laser-matter interaction process through a proper control of the target properties. In fact, as explained in Section 2.2.1, in the TNSA mechanism laser energy is transferred to ions through the hot electrons. Hence a reasonable point would be to design target configurations able to improve this part of the process by enhancing the energy transfer from laser to hot electrons. Dealing with solids, as pointed out in Section 1.3.2, decreasing the density of the interacting material down to the critical density is the way to enhance laser absorption. This is the general aim of the experimental research described in Part III. The present Chapter is devoted to the introduction of those general ideas which have gone along the development of this work. In Section **??** we will discuss the recently published methodologies to move the interaction down to the so-called "near-critical" regime. Afterwards in Section 5.2 we will examine a particular multilayered target configuration combining the absorption advantages of low-density me-

dia integrated in the "common" TNSA setup, leading to an enhanced TNSA regime.

5.1 Ion acceleration in the near-critical regime

In this section we start from ultraintense laser-matter interaction physics, in order to understand the basis of the ion acceleration optimization criteria explored in this thesis work. As we have discussed in detail in Chapter 1, two interaction regimes may be reached either the plasma owns a density larger or smaller with respect to the critical value $n_{cr} = m_e\omega^2/4\pi e^2$, being ω the frequency of the incident laser light (see eq. (1.6)). In case of underdense plasmas ($n_e < n_{cr}$) an incident laser pulse can propagate through it according to the linear theory. Hence the interaction volume is the whole plasma itself. By considering also the nonlinear effects, the laser pulse may loose energy while passing through the plasma via collisionless mechanisms as excitation of plasma waves due to the wakefield generation, or other resonant processes as the parametric instabilities discussed in Section 1.3.1. If the incident laser is sufficiently intense these plasma waves may break their spatial coherence and transfer energy to electron bunches, whose maximum energy is proportional to the maximum longitudinal field in eq. (1.29). Hence it increases with *increasing* density. If we consider overdense plasmas ($n_e > n_{cr}$) the laser pulse is classically inhibited from penetrating and is reflected back except for an evanescent component inside the target. Thus the interaction volume is limited to the skin layer whose thickness is $\sim c/\omega_p = (\lambda/2\pi)\sqrt{n_{cr}/n_e}$. Here other collisionless (resonant or not-resonant) mechanisms lead to the excitation of surface plasma oscillations which may break and generate fast electrons (see section 1.3.2 for more details). In this regime usually the absorption fraction increases with *decreasing* density as far as the laser pulse can penetrate more deeply inside the plasma.
For usual experiments in the underdense and overdense regime, high intensity lasers with optical or near-infrared wavelengths ($\lambda = 0.8 - 1$ μm) are used and, by eq. (1.6), $n_{cr} \sim$ mg/cm^3. Hence these regimes correspond in practice to the use of gas targets with densities $n_e \ll n_{cr}$ and of solid targets with $n_e \gg n_{cr}$, respectively. From the above arguments and based on some published experimental and numerical results [122–124], the scaling with density suggests that a regime at the boundary between underdense and overdense plasma with $n_e \simeq n_{cr}$

may lead to efficient absorption of the laser energy and fast electron generation. Despite the interest in such conditions, they have not been accurately investigated with experiments, mostly because targets with such properties are not straightforward to produce. Actually, in real experiments the laser pre-pulse often leads to early plasma formation from the solid target, so that the short-pulse, high-intensity interaction occurs with an inhomogeneous plasma having both underdense and overdense regions separated by a near-critical zone. However, such conditions are often out of any experimental control, hence one can hardly think to try optimizing and actively controlling the energy absorption.

Some experiments aimed at improving ion acceleration by laser pulses are reported in the recent literature, where the near-critical interaction regime is achieved in a controlled way by different methods. Yogo et al [125] have used a 7.5 μm polyimide $[(C_{22}H_{10}O_4N_2)_n]$ target which has been converted into a near-critical plasma by a duration-controlled amplified spontaneous emission with intensity of 10^{13} Wcm^{-2}. In this way the femtosecond main pulse interacts obliquely with a preformed plasma and the emission of protons at some angle between the target normal and the laser propagation axis is observed. This shift from target normal direction is due to the generation of quasi-static magnetic fields at the rear side after the laser channeling through the plasma target, inducing an asymmetric charge separation induced electrostatic field with respect to the normal. The obtained maximum proton energies ~ 4 MeV are consistent with the values obtained with "ordinary" solid targets at the same intensity (see Sections 2.1.1 and 4.2). More-

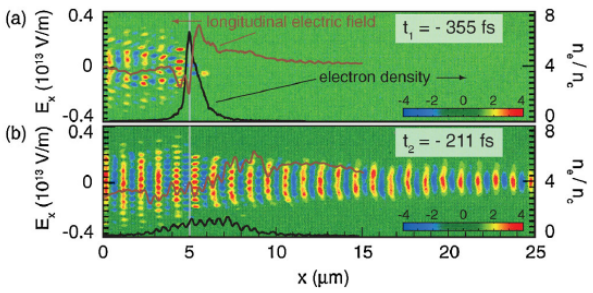

Figure 5.1: *Results from 2D-PIC simulations at two different times, before (a) and after (b) the peak intensity has arrived onto the target. The black curve shows the normalized electron density n_e/n_{cr}, while the longitudinal electric field E_z is marked in red (font [73]).*

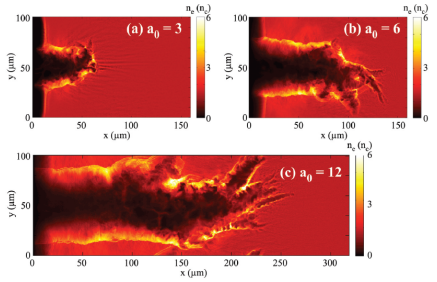

(a) Final electron densities in a $1.5n_{cr}$ plasma at each simulated intensity (a=3,6,12).

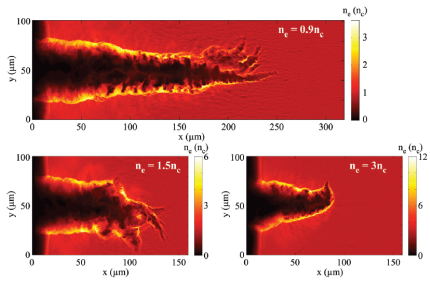

(b) Final electron density at each simulated plasma density (0.9,1.5,3 n_{cr}).

Figure 5.2: *2D-PIC simulations of the density profile in the laser-generated channel during the propagation inside the foam target at varying intensity and plasma density (font [127]).*

over no clear dependence of maximum proton energy on ASE duration is observed, probably because though the pre-pulse control, the near-critical plasma is still longer to be really controlled in density and profile. Henig et al [73] adopted C targets having a thickness comparable with the laser skin depth, so that after few laser cycles from the interaction it expands to thicknesses near the laser wavelength and, taking into account the relativistic effects, it becomes relativistically transparent as shown in Fig. 5.1. A strong volumetric heating of the electrons sets in, driven by the laser pulse penetrating the target, which allows to observe maximum ion energies larger than those observed with the same laser conditions but "ordinary" targets. Jung et al [126] have exploited the same ultrathin target configuration but with laser pulses having one order of magnitude larger intensity and circular polarization, which have allowed to observe a peaked ion spectrum, while the spectra obtained by Henig et al [85] are exponentially distributed with a cutoff ("TNSA-like"). This could be due to the partial suppression of TNSA by the combination of higher intensity and circular polarization (see Section 1.3.2).

The near-critical regime might be achieved also by using a low-density targets, such that the initial bulk density be already of the order of critical density. Low-density materials are often referred to as "foams": in Chapter 6 we will examine in detail the meaning of this term from the material science viewpoint. Li et al [128] have adopted rather thick deuterated polystyrene [$(C_2D_3)_n$] foams (>100 μm) interacting with moderate-intensity ($\sim 10^{19}$ Wcm^{-2}) and long duration (>500 fs) laser

pulses. Here the isotropic acceleration of ions from the bulk in addition to the surface one is observed and the energies are lower than ordinary TNSA even though the number is enhanced. Willingale et al [74, 127] explored the same system by using similar duration laser pulses but with higher intensities ($\sim 10^{21}$ Wcm^{-2}). The laser drills a hole in the foam, whose length depends strongly on intensity and plasma density (see Fig. 5.2). Increasing the intensity protons are observed to increase their number and energy. In particular, at the lowest densities they become very similar to that obtained with solid targets. The maximum energy depends on laser energy absorption, which is higher the longer the channel, hence both at decreasing density and increasing intensity. Most of the above-mentioned studies envision an ion acceleration mechanism which may be considerably different from TNSA. However, as pointed out in the Introduction, TNSA is the most-investigated and "robust" mechanism in experiments. Moreover, features such as broad-spectrum and ultra-low-emittance proton emission make it most suitable for specific important applications such as time-resolved proton radiography. It is thus of interest to couple the potential of low-density targets with the TNSA scheme.

5.2 Ion acceleration with foam-attached targets

Following the discussion in previous Section, a multi-layer target configuration, where a near-critical density layer is attached on the irradiated side of a thin solid foil, can enhance the laser energy absorption and the ion acceleration process. An "advanced" TNSA regime may in principle be obtained. In this Section we will discuss the few relevant numerical works where such a target configuration has been studied. Nakamura et al [129] used 2 dimensional PIC simulations where a normally incident, clean (without pre-pulse), 40 fs pulse is considered (see the initial density distribution in Fig. 5.3(a)). An enhancement of proton acceleration due to the presence of the foam has been shown as a function of its properties. Through a detailed study on field ionization processes occurring inside the foam, particular emphasis is given on the improved laser-to-plasma energy coupling. As can be seen in Fig. 5.3(b), a periodic structure of ion charge density appears. At early time (< 70 fs) after the interaction, the charge density modulation is due to the inhomogeneity of ion charge state resulting from the laser standing pattern, generated by the reflection on the solid after

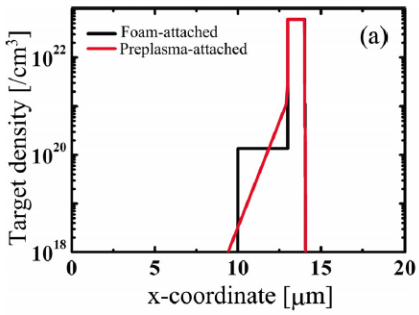

(a) Initial distribution of number density of Al ion for preplasma-attached, and average number of atom SiO_2 for foam-attached targets.

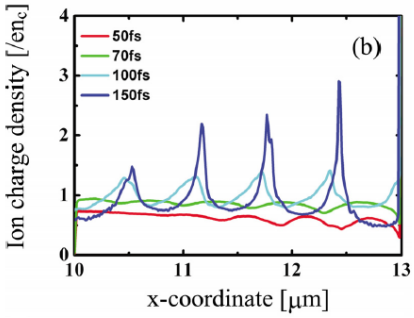

(b) Time evolution of ion charge density during laser irradiation.

Figure 5.3: *2D-PIC simulations results from the work by Nakamura et al [129].*

the propagation through the foam. At later time a concurring cause becomes also the spatial inhomogeneity of the ion number density as a result of their dynamics.

Sgattoni et al [130] extended the investigation of this system in different directions, within the framework of the SULDIS project[1]. Fully three-dimensional (3D) and two-dimensional (2D) simulations with oblique incidence have been run using the PIC code `ALaDyn` [119–121], in order to investigate the dynamics of the laser interaction with the slightly overcritical density plasma and the role of the foam electrons in the rise of the longitudinal electric field which accelerates the protons. The importance of a 3D study lies in the correct quantitative estimation of the maximum values of proton energy and the acceleration dynamics. The simulations led to proton energy spectra with an exponential cutoff typical of the TNSA mechanism. At a laser intensity a=10, corresponding to $\sim 2 \times 10^{20}$ Wcm^{-2}, in the presence of a foam layer, although rather thin (2 μm), the maximum proton energy is much higher than without foam (see Fig. 5.4). The same simulations have been performed also in two dimensions: the cutoff energy of the protons is systematically overestimated (by a factor of ∼2 at time 166 fs) but the ratio $E^{2D}_{max,f}/E^{2D}_{max,b} \simeq E^{3D}_{max,f}/E^{3D}_{max,b} \simeq 2.3$ is preserved. Hence, although it is evident that the 3D analysis is essential to quan-

[1]SULDIS, Superintense Ultrashort Laser-Driven Ion Sources, is a 4-year project, approved and financed by the Italian Ministry for Education, Universities and Research under the program FIRB-Futuro in Ricerca. The work of the present PhD thesis falls into the same research activity (see [131] for more details).

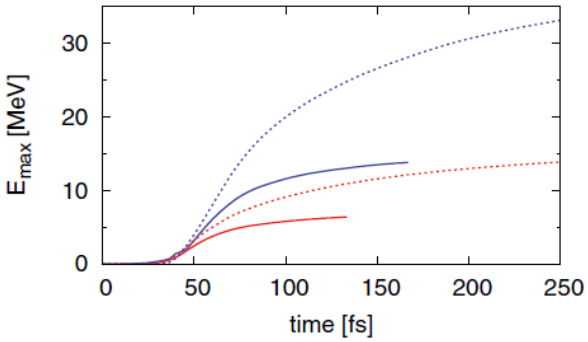

Figure 5.4: *3D simulations results of proton maximum energy evolution with respect to time: comparison of 3D (solid) and 2D (dashed) cases without foam (red, lower lines) and with (blue, upper lines)* n_f*=2*n_{cr}*,* l_f*=2*μ*m,* n_s*=40*n_{cr}*,* a*=10. (font [130]).*

titatively evaluate the maximum ion energy, 2D simulations can be adopted for a more extensive parametric investigation of the system aimed at both showing the existence of an optimal foam thickness as a function of the laser amplitude and angle of incidence, and evidencing features of the electron acceleration and sheath field formation processes. In the 2D parameter scans laser intensity has been varied in the range a=3-20 ($\sim 10^{19}$-10^{21} wcm^{-2}) and the angle of incidence from 0° to 60°. Pulse duration and waist are fixed to 25 fs and 3 μm, respectively and the simulations have been stopped after t=166 fs. The electron density of the foam n_f and its thickness l_f have been varied in the ranges $1n_{cr}$-$8n_{cr}$ and 1-12 μm, respectively. When a low-density foam layer is present, the energy absorption mechanism is different from the case of a highly overdense plasma: in the considered range of parameters the laser propagates through the foam and is not effectively reflected until it reaches the solid layer. During the interaction with the foam, the laser pulse accelerates the electrons to relativistic velocities and its energy is considerably depleted. A minor portion of the laser energy is then also absorbed by the high-density plasma similarly to the case without foam. Fig. 5.5(a) reports a detailed *energy balance* of the kinetic energies belonging to the various species as a function of time with respect to laser energy. When a sufficiently thick foam is present (l_f=4 μm), the electrons gain a notably large fraction of the initial laser energy (up to >50% of the total energy, whereas without foam the corresponding value is ∼5%). The ions slowly gain energy at

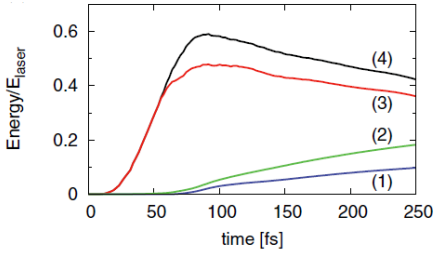

(a) The time evolution of the energy normalized to the initial laser energy of all electrons (black, 4), foam electrons only (red, 3), all ions (green, 2), and contaminant protons only (blue, 1).

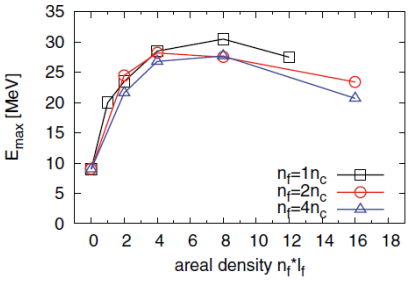

(b) Proton maximum energy for a=10, different foam thicknesses, and foam densities (black squares, n_f=n_{cr}; red circles, n_f=2n_{cr}; blue triangles, n_f=4n_{cr}) as a function of the areal density n_f=4n_{cr}.

Figure 5.5: *2D simulation results from parameter scans (font [130]).*

the expense of both the electron kinetic energy and the electrostatic energy. The protons from the contaminants get ∼50% of the total kinetic energy absorbed by all the ion population of the simulation, accounting for up to 10% of the initial laser energy (to be compared with ∼1% of the corresponding case without foam). As pointed out above the simulated proton spectra are TNSA-like and in Fig. 5.5(b) *maximum proton energy* is reported as a function of the foam areal density (thickness in microns times n_f/n_{cr}). It is noteworthy that the dynamics in 2D simulations is not yet stopped after 166 fs (see Fig. 5.4). This comparison shows how, at a given laser intensity, there is an "optimal" foam thickness for each value of the density (for a=10, 8-12 μm for n_f=n_{cr}, 2-4 μm for n_f=2n_{cr}, and 1-2 μm for n_f=4n_{cr}) and, at least in the range of parameters considered, this corresponds to the same value of the areal density. Moreover at a given laser intensity, an optimal value of the foam areal density can be found and it grows approximately linearly with it. The increased proton energy is a direct consequence of the stronger electric field arising when a foam layer is present. By considering a foam-attached target, the *accelerating field* at the rear side is also due to the highly relativistic electrons generated from the foam and promptly escaping far away from the target, and it is strongly different from the expression that is obtained in the assumption of a Boltzmann equilibrium. In Fig. 5.6 a comparison between the accelerating fields obtained with an ordinary and a foam-attached targets is reported. In the presence of a foam, the longitudinal electric

field exhibits a different shape and a maximum value, after the laser pulse has been reflected by the solid layer (>70 fs), about three times higher if compared to the case of a bare solid foil. A field exponential decrease is accompanied for several microns from the rear surface by a nearly uniform shape. The exponential decrease can be attributed to a hot electron population which expands around the target similarly to the ordinary TNSA case. By decreasing the foam thickness this novel field structure becomes less distinguishable and more similar to the ordinary TNSA fields. The difference in the longitudinal field is

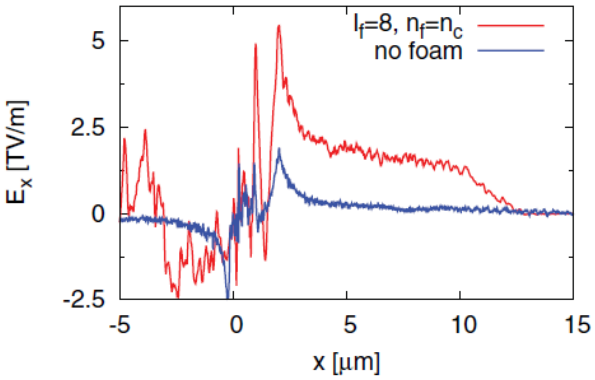

Figure 5.6: *Longitudinal electric field along the focal axis z with a foam layer (n_f=1n_{cr} l_f=8 μm, upper line) and without, for a=10 at t = 100 fs after the interaction's onset. The peak values are $E_{z,max}$=5.4 TV/m and $E_{z,max}$=1.8 TV/m (font [130]).*

due to the additional *electron acceleration mechanism* occurring when a foam layer is present. In fact apart from the dominance of Brunel's mechanism and $\mathbf{j} \wedge \mathbf{B}$ heating in the interaction with the solid foil (explained in Section 1.3.2), a new acceleration process, occurring over the volume of the foam, is observed. The electron cloud expands with a roughly spherical symmetry for several microns and displays regular bunching structures in the longitudinal direction (see Fig. 5.7 for both a 3D (a) and 2D (b) visualization of electron density). These structures and the more efficient coupling for *p*-polarization, combined with the observed penetration and channeling of the laser pulse inside the foam, have suggested that the dominant mechanism of fast electron generation may be similar to that observed in hollow microcone targets, which have allowed to obtain the highest proton cutoff energy experimentally observed to date [132]. The mechanism in the latter case relies on the effective local grazing incidence of the laser pulse

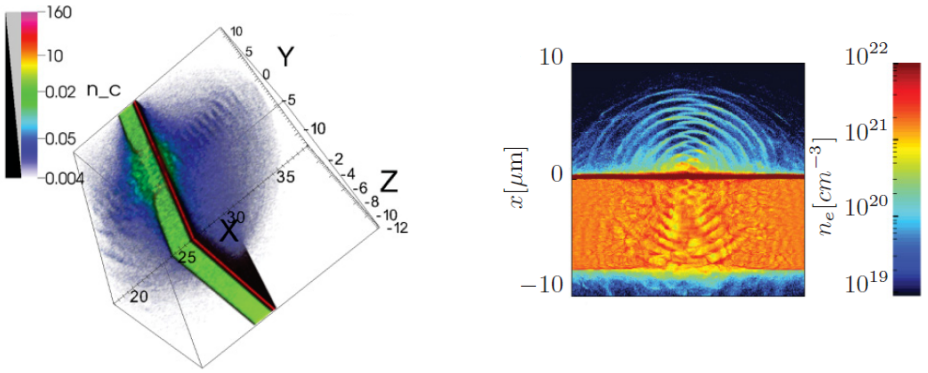

(a) Volume rendering of electron density from 3D simulation.

(b) Electron density from 2D simulation.

Figure 5.7: *Electron density results from 2 and 3 dimensional PIC simulations (font [130]).*

on the microcone walls, where the P component of the electric field extracts electrons which are then accelerated by the combined action of ponderomotive force and self-generated fields, resulting in electron temperature much higher than the ponderomotive scaling (1.35). The penetration of the laser pulse inside the foam effectively yields a "self-generated microcone", providing a similar coupling at grazing incidence with the channel walls. To maximize the efficiency of the process, it is not necessary to reduce the thickness of the solid target to very low values as seen in Section 5.1 ($\sim$ few nm). Moreover additional parameter scans have showed that the proton energy is not strongly affected if the laser irradiates the target at moderate angles ($<30°$), whereas for larger angles the oblique incidence is considerably less efficient in producing high-energy protons. The explorative numerical works by Nakamura et at, Sgattoni et al have showed how the presence of a foam attached to a solid foil might strongly reduce the role played by the areal density of the solid target for the proton acceleration. Moreover a very recent work by Wang et al [133] has reported a 2D-PIC study of proton acceleration using a similar two-layer target by exploiting high intensity values. A gain factor around 3 is found, due to the laser relativistic self-focussing in the near-critical layer where electrons are directly accelerated in the channel and an optimal condition is achieved by choosing a foam layer thickness equal to the laser self-focussing length. On the other hand this concept is actually unexplored experimentally, mainly because such multi-layered targets with foams

having a well controlled adhesion to solid, thickness and density have not been produced yet. The goal of this Part of the thesis is to work on this open point, hence to study a suitable method able to produce this target configuration. To this end in Chapter 6 a review of low-density materials will be presented from the viewpoint of material science, in Chapter 7 the production and characterization of foam-attached targets will be discussed, while in Chapter 8 we are going to present the experimental results coming from an ion acceleration campaign where our foam-attached targets have been tested.

6

Production of foam-attached targets

Since in Chapter 5 we have introduced the near-critical regime of ultraintense laser-matter interaction, we devote the present chapter to a deeper insight in the Material science of low-density media. A quantitative estimate of the mass density corresponding to such a regime might be performed using equation (1.6) and taking into account that ultraintense and ultrashort laser pulses can be achieved within the near-infrared spectral range, i.e. for $\lambda = 0.8 - 1$ μm. It follows that the density regime of interest falls within the mg/cm^3 range, that is to say three orders of magnitude below the typical solid densities. To this end several techniques, either physical or chemical, have been exploited in order to produce materials with such low densities, which own peculiar properties, generally different from the solids. Moreover the lower the density, the less straightforward the characterization, in particular for those applications requiring a fine control of this property. In this Chapter we will first introduce low density materials in Section 6.1, by classifying them according to the spanned density regime ("nanoporous materials" and "foams") and by numbering the various unconventional properties they own, making them attractive for several applications. The several possible production techniques will be also discussed. Afterwards we will cope with the important issue of density measurements. To this end in Section 6.2 the most widely used nuclear density measurement techniques (Nuclear Reaction Analysis and Rutherford Backscattering Spectroscopy) will be gone through. Finally in Section 6.3 we present the methodology to produce and characterize foam-attached targets we have chosen

and followed. In particular in Section 6.3.1 the production with Pulsed Laser Deposition of low-density foams is discussed, while in Sections 6.3.2 and 6.3.3 the two methods we have adopted to characterize foam densities (Quartz-Crystal Microbalance and Energy Dispersive X-ray Spectroscopy, respectively) are introduced and explained. These techniques are definitely less demanding in terms of the measurement apparatus, with respect to the nuclear ones, although there still have few implementations in literature.

6.1 From nanoporous materials to foams

Low-density materials are of great interest both for fundamental material science and in the light of various applications. They belong to the broader class of *nanoporous* (NP) materials which include the well known aerogels [134], generally characterized by unconventional physical properties as for example nanometer-size pores, densities lower than water, within the 100 mg/cm^3 regime, high specific surface areas and high porosity [135]. Their mechanical, thermal and electrical properties are strictly dependent on pore size [136]. Several applications have been explored for these materials, owing to their peculiar and versatile properties. Thanks to the high and tunable porosity Siegal et al [137] have used them as highly-controlled gas adsorbers for microsensor preconcentrators, Turgut at al [138] have studied them to provide artificial bone implantation and Nam et al [139] have been able to fabricate a wide range of temporal tissue scaffolds requiring a specific shape and geometry. Zhang et al [140] have studied NP materials for their application in electrochemical supercapacitors, by exploiting their large surface area. Moglie et al [141] have measured the shielding effectiveness of NP carbon aimed to the development of lightweight microwave shielding structures. For such highly porous materials, density is considered as a mean value over a scale sufficiently larger than the typical microscopic inhomogeneity scale-length [142].
Ultra-low density materials, often referred to as *foams*, span densities in the range 1-100 mg/cm^3. Foams show unique properties, as for example an almost perfect black-body-like attitude observed by Shvedov et al [143] and an anomalous ferromagnetic behavior [144, 145]. Moreover an increased gas and liquid adsorption and storage capability have been measured [146]. Furthermore this is the density range where the near-critical regime of ultraintense laser-matter interaction is

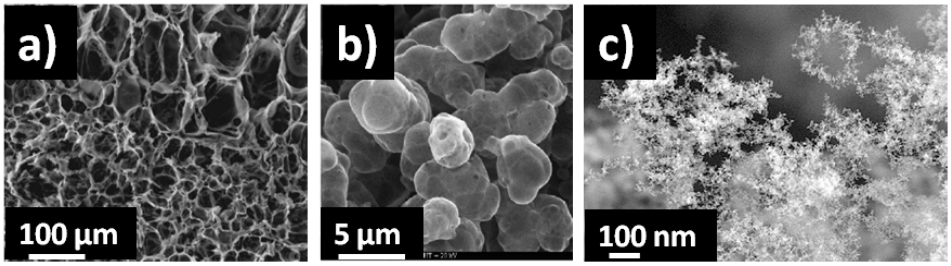

Figure 6.1: *Electron microscopy images of foams produced by different techniques. (a): Melt-mixing of microparticulate composites, then gas-foamed using carbon dioxide [147]. (b): Sol-gel method from pyrogallol-formaldehyde mixtures in water using perchloric acid as catalyst [154]. (c): Carbon nanofoams produced via laser ablation [155].*

concerned, where the electromagnetic energy absorption is observed to increase, as we have discussed in detail in Section **??**. Foams have been so far produced with different materials, like carbon, silicon carbide, silica, aluminum and alumina, and by different techniques. In Fig. 6.1 we have reported illustrative micrographs of foams produced by different fabrication methods. Foaming processes have been adopted with different blowing agents, such as for example carbon dioxide [147], supercritical carbon dioxide [148] and aluminum nitrate [149]. Moreover sol-gel polymerization [150–152] and laser ablation [153] have been exploited. In particular the possibility to produce foams with controlled and reproducible mean density, area and thickness, with a satisfactory adhesion on a solid substrate might be of great importance to achieve desired material properties and/or for specific applications.

6.2 Nuclear-based density measurement techniques

Since the precise characterization of mass density is of paramount importance for the development of carbon foam-attached targets, the present section is devoted to film density measurement methods. The general recipe is to to measure separately its *areal density* $\rho_f z_f$ [g/cm^2] and its *geometrical thickness* z_f [cm]. Usually to determine the areal density of a film, nuclear techniques like the Rutherford Backscattering Spectroscopy (RBS), the Nuclear Reaction Analysis (NRA) and the Elastic Recoil Detection Analysis (ERDA) are used. In this work to measure foam densities, we have adopted two non-nuclear techniques namely the Quartz-Crystal Microbalance (QCM) and the Energy Dis-

persive X-ray Spectroscopy (EDXS), which are less demanding in terms of measurement apparatus and will be discussed in detail further on in Sections 6.3.2-6.3.3. On the other hand the geometrical thickness is usually measured either by the Scanning Electron Microscope (SEM) or by the Transmission Electron Microscope (TEM), depending on the order of magnitude to whom the film thickness belongs. In the following of the present Section, we will review in 6.2.2 the NRA technique and in Section 6.2 the RBS.

6.2.1 Rutherford Backscattering Spectroscopy (RBS)

RBS is a nuclear analysis technique which is widely used in order to get information on the type and distribution of the elements characterizing superficial layers of examined samples. A light ion beam (mainly protons H^+ or helium ions He^+) is boosted to energies up to few Mev (0.5-4 MeV) by a linear Van de Graaf accelerator with a quasi-monochromatic spectrum, a good collimation and a transverse section of ~ 1 mm^2 and is directed onto the sample. Afterwards the ions experience Coulombian-like elastic collisions with the sample's atoms and a part of them is backscattered to a detector which is placed at some angle from the incident beam axis. Ions scattered within the solid angle covered by the detector are counted and discriminated by energy. The typical output of a RBS measurement is the spectral distribution of the backscattered ions. From peak position, height and width one can perform a compositional analysis and measure the film areal density. To better explain a RBS measurement, let us consider first a monoatomic layer having the same content of Cu, Ag and Au. By look-

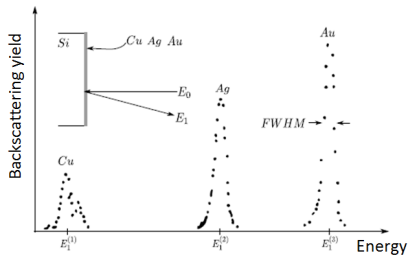

(a) RBS spectrum of a Cu-Ag-Au monolayer.

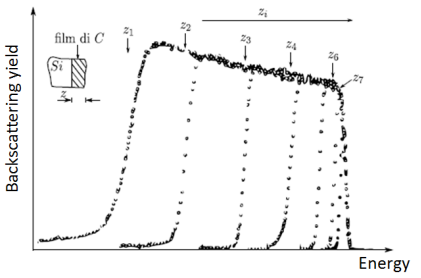

(b) Spectra of monoelemental C films deposited on Si with varying thickness.

Figure 6.2: *Rutherford Backscattering Spectroscopy spectra.*

ing at the spectrum in Fig. 6.2(a), one can state that different atoms give signals at different energies and the larger the atomic mass of the element, the higher the peak energy and height. When a monoelemental film is analyzed its spectrum is a single peak which broadens as a function of its thickness, maintaining as a common feature the high energy tail (see Fig. 6.2(b)). Moreover the width of the energy band corresponding to a film thickness is proportional to its areal density $\rho_f z_f$. Hence RBS constitutes a non-destructive technique able to give a quantitative estimate of the areal density of a sample, without claiming for a reference measurement. Since the Rutherford scattering cross-section increases with the mass of sample atoms, RBS is much more accurate in measuring heavy elements. For light elements a complementary technique might be used, the ERDA, in which the detector records the ions forward scattered, being the most probable process to happen. Compositional analysis and areal density are determined in the same fashion of RBS method.

6.2.2 Nuclear Reaction Analysis (NRA)

NRA is a nuclear analysis technique that adopts ad-hoc nuclear reactions to study quantitatively the composition profiles of a sample. A particle beam is sent onto a sample such that a nuclear reaction between the particles and the sample's atoms will likely take place. The products are then detected by a spectrometer located at an angle from the incident beam. For the case of a carbon film a deuteron beam is adopted in order to induce the following (d, p) reaction:

$$^{12}C + d \rightarrow {}^{13}C + p + Q$$

where Q is the reaction energy. The total number of detected protons N_p coming from a reaction happened at a depth z is proportional to carbon concentration at the same depth in the sample and to the reaction cross-section:

$$N_p = N_C(z) \cdot I_d \cdot \sigma(E_d(z)) \cdot \Delta\Omega \cdot z \tag{6.1}$$

where $N_C(z)$ is the concentration [atoms/cm^3] of carbon atoms at depth z, I_d the incident deuteron number, $\sigma(E_d(z))$ the differential reaction cross-section, $\Delta\Omega$ the detected solid angle. The film areal density $\rho_f z_f = (A/N_{av})N_C(z) \cdot z$, with A atomic mass and N_{av} the Avogadro number, may be quantitatively estimated only if the reaction

cross-section $\sigma(E_d(z))$ is known. This could happen either if the sample concentration profile is given or if the cross section varies slightly with incident particle energy, such that $\sigma(E_d(z)) \simeq \sigma(E_0)$, being E_0 the initial deuteron energy. Nevertheless if the reaction cross-section is unknown one can obtain the areal density as well by introducing a reference sample with known chemical composition. In this way, by using eq. (6.1) for each measurement, the following relation holds:

$$\frac{N_C(z) \cdot z}{N_C(z) \cdot z_{ref}} = \frac{N_p}{N_{p,ref}}. \tag{6.2}$$

6.3 Methods to produce foam-attached targets for laser-ion acceleration

As pointed out in Section 5.2, superintense laser-driven ion acceleration might reach an advanced acceleration scheme in the framework of TNSA by using a novel target design so-called *foam-attached* and composed by a solid foil attached to a foam layer. In this Section we will point out in 6.3.1 the method we have chosen to produce such a target configuration. Afterwards the areal density measurement techniques adopted to characterize the density of the foams will be discussed in 6.3.2 and 6.3.3.

6.3.1 Production of foams by Pulsed Laser Deposition

The foam layer constituting the front surface of a foam-attached target is required to have a controlled thickness and tunable mean density, in order to guarantee a good degree of reproducibility in laser-ion acceleration. Pulsed Laser Deposition (PLD) can represent an ideal solution to obtain a film with such properties, being a widely used material production technique, versatile in a broad range of tunable process parameters and allowing to use virtually every kind of material for both targets and substrates. It guarantees nice adhesion properties since the deposited films are not attached but directly grown on a solid substrate (see Appendix A.1 for more details). Among the other materials (numbered in Section 6.1), carbon represents a particularly suitable choice as foam constituent since, being a light element, it makes it easier to reach the low densities of interest in the light of a foam-attached target configuration and because it can in principle lead to a monoelemental film due to its volatile oxides. The latter is also an important point

for the application in ultraintense laser-ion acceleration, as it makes the estimate of plasma mass density easier, once its ionization degree is known. A very large documentation about carbon based materials produced by PLD within the compact-amorphous regime can be found in literature [156–159]. Porous-amorphous carbon has been investigated using a broad range of PLD parameters reaching in all cases densities typical of NP materials [137, 160–164]. For example Siegal et al [137] has obtained values in the range 100-1000 mg/cm^3. On the other hand, only in the works by Rode et al [155,165,166] the production of carbon foams by PLD has been discussed. There, an unconventional set of deposition parameters, namely high values of fluence ($\sim$120 J/cm^2), Ar pressure ($\sim 10^4$ Pa) and repetition-rate (kHz) have been exploited in the attempt to get a material having a significant sp^3 bonding content and densities around 2-10 mg/cm^3.
In the framework of this PhD work, we have performed depositions of carbon foam films by PLD, aimed to the engineering of foam-attached targets for TNSA enhancement. Our goal has been to gain an effective and independent control of mean density, thickness, surface uniformity and adhesion of foam layers, by exploiting a so far unexplored combination of the most relevant deposition parameters for the production of porous carbon, i.e. fluence, gas type and pressure, and laser repetition rate (see A.1). In particular the second harmonic, λ=532 nm, pulse of a Nd:YAG laser, duration 5-7 ns have been directed on a 2 in. pyrolitic graphite target with 45° angle of incidence (see Fig. 6.3). The ablated carbon species expand from the target to a substrate which have been chosen differently depending the foam was deposited for characterization or for ion acceleration. In Chapter 7 we will present in detail the results we have collected from mean mass density measurements together with both morphological and structural characterizations as a function of the main deposition parameters.

6.3.2 Quartz-Crystal Microbalance (QCM)

The QCM is a mass measurement technique usually adopted to assess the deposition rate in physical vapor deposition facilities, as for example PLD, and it is one of the two techniques adopted to measure foam areal density in this PhD work. QCM consists of a 8 mm diameter oscillating quartz crystal located in the substrate position and gives an *indirect* measurement of the deposited mass for every deposition conditions by transducing the deviations from its natural

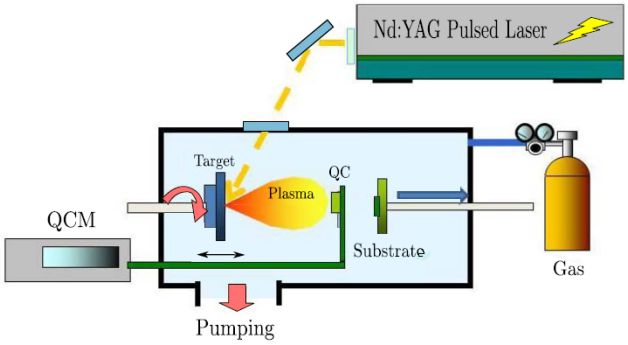

Figure 6.3: *Schematic representation of the PLD apparatus at Department of Energy of Politecnico di Milano, exploited for the foam-attached targets production. For a more detailed explanation of pulsed laser deposition technique we refer to Appendix A.1.*

oscillation frequency f_q due to the increased mass (see Appendix A.1 for more technical details). The typical QCM output is the areal density as a function of deposition time (see Fig. 6.4, which is calculated starting from the measured frequency shift signal $\Delta f/f_q$ and two manual input parameters, namely film density and Z-ratio (i.e. the acoustic impedance matching parameter between the film and the substrate) [167, 168]. In order to extrapolate an areal density measurement, default values for them have to be assumed (ρ_{fict} =1 g/cm^3 and Z_{fict} =1 respectively). Two possibilities may arise, depending on the nature of the analyzed sample. If the film is sufficiently homogeneous, $\Delta f/f_q$ can be assumed proportional to the deposited mass and a constant deposition rate emerges as shown in Fig. 6.4(a). Hence in this scenario a proportionality relation between fictitious and real deposited mass holds:

$$\rho_f z_f = \rho_{fict} z_{fict} \tag{6.3}$$

where z_{fict} is the fictitious film thickness corresponding to the deposition time. Whereas if the film starts to be inhomogeneous, $\Delta f/f_q$ varies nonlinearly with the deposited mass and the QCM response is that of Fig. 6.4(b), where an apparently decreasing deposition rate is observed. This could have been due to two possible effects. A decoupling between quartz crystal and film might have happened at increasing thickness due to the scarce acoustic properties of a foam material [169]. Moreover, taking into account the quartz natural frequency, the deposited film experiences a maximum shear acceleration

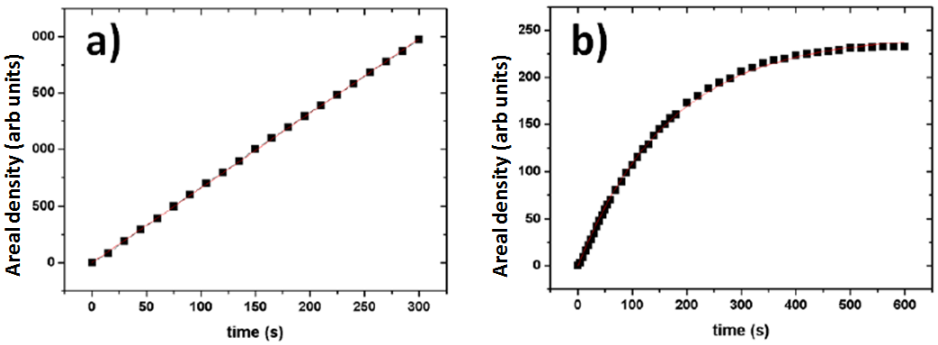

Figure 6.4: *Typical areal density measurements by QCM for homogeneous (a) and inhomogeneous (b) films.*

of the order of $10^4 g$ which might have set up a steady dynamics, where carbon reaching the crystal and carbon blown off by the vibrations have become equal. As far as the deposition rates for mean density estimates are concerned, the linear regions of the measured curves are relevant. These data have been successfully fitted with exponential curves $y = a(1 - \exp(-bx))$, where a and b are fitting parameters such that ab is the required zero slope. This assumption has been found to have some limitations as the deposition ambient pressure increases, especially when very inhomogeneous films are obtained. In these cases a more accurate technique would be required.

6.3.3 Energy Dispersive X-ray Spectroscopy (EDSX)

To support QCM results, in particular dealing with inhomogeneous samples, a novel non-destructive and *direct* method has been developed. It involves the quantitative measurement of K_α peak intensity by means of a micro probe X-ray analysis tool based on EDXS (see Appendix A.1). The X-rays are generated in the sample by an electron beam accelerated in a SEM column. Electron energy is then a crucial control parameter for this technique, since it determines both the interaction volume and the penetration depth of the probe. The first step to build up an interpretative model able to extract the areal density from the K_α intensity of a sample is the modeling of the X-rays emitted intensity of the sample under analysis, which does not correspond to the generated intensity of X-ray, since some effects leading to their attenuation occur. To take into account these effects the Probability Function for X-ray Production (PFXP) $\Phi(\rho z)$ is introduced as

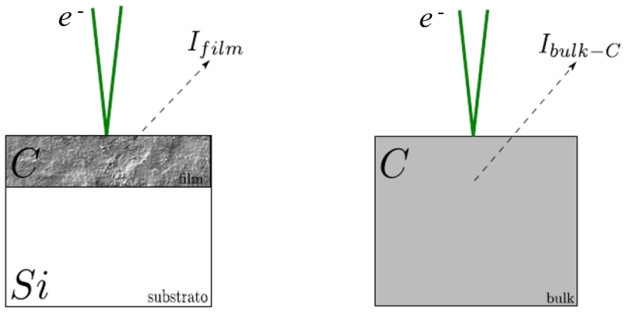

(a) Film/substrate (b) Reference

Figure 6.5: *Methodology proposed by Bishop&Poole.*

a function of the sample areal density crossed by the electrons [170] and depending upon system parameters like the sample atomic number, ionization potential and backscattering coefficient, electron probe and K_α energy and finally the detector geometry. Once the PFXP is known the quantitative estimate of areal density is obtained by comparing the X-ray intensity emitted by the sample with the one emitted by a proper reference. In the following we will consider for simplicity carbon films deposited on silicon substrates. Two different interpretative models of EDXS data have been used: the first exploits K_α signals from the C film (I_{film}) and a reference bulk (I_{bulk-C}) having the same known composition. The experimental setup is shown in Fig. 6.5 and has been proposed for the first time by Bishop&Poole [171]. Areal density $t = \rho_f z_f$ is extracted by numerically inverting the integral

$$k_1 = \frac{I_{film}}{I_{bulk-C}} = \frac{\int_0^t \Phi_C^*(\rho z)\exp(-\chi_c \rho z)\,\mathrm{d}(\rho z)}{\int_0^\infty \Phi_C(\rho z)\exp(-\chi_c \rho z)\,\mathrm{d}(\rho z)}, \tag{6.4}$$

where $\Phi_C(\rho z)$ is the PFXP in the standard reference, while $\Phi_C^*(\rho z)$ is the PFXP in the sample after the correction for the effects of the substrate. In fact, in the calculation of Φ_C^*, an effective backscattering coefficient is computed as a function of substrate and sample coefficients. χ_c is the known X-ray attenuation factor in carbon. The calibration relation of the intensity ratio k_1 as a function of areal density, obtained after the inversion of integral (6.4), is reported in Fig. 6.6(a) and, although the differences between Φ_C and Φ_C^*, by using the

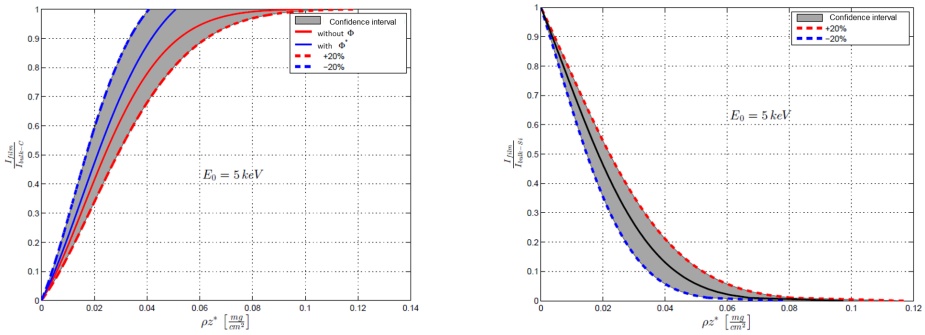

(a) Method by Bishop&Poole

(b) Method by Bentzon&Nielsen

Figure 6.6: *Calibration curve and confidence interval as result of the inversion of integrals* (6.4) *and* (6.5) *in the two interpretative models of EDXS data.*

former without any correction for the substrate effects, one obtains an areal density value within the ±20% uncertainty given already by the calculation of PFXP. In order to obtain areal density values within this confidence interval one has to set an electron accelerating voltage such that k_1 stays between 0.03 and 0.95 [172].
The second interpretation model, proposed for the first time by Bentzon&Nielsen [173], compares the K_α signals from the substrate under the film (I_{sub+C}) and a bulk having the same composition of the substrate ($I_{bulk-Si}$) as shown in Fig. 6.7. The areal density $t = \rho_f z_f$ is extracted by inverting the integral

$$k_2 = \frac{I_{sub+C}}{I_{bulk-Si}} = \frac{\exp(-\chi_c t)\int_t^\infty \Phi^*_{Si}(\rho z)\exp[-\chi_s(\rho z - t)]\,\mathrm{d}(\rho z)}{\int_0^\infty \Phi_{Si}(\rho z)\exp(-\chi_s \rho z)\,\mathrm{d}(\rho z)} \quad (6.5)$$

Here Φ_{Si} is the PFXP of the substrate and Φ^*_{Si} the PFXP corrected for the effects of the C film deposited on the substrate. Nevertheless in this experimental setup the electron energy must be calibrated such that the interaction and X-ray generation takes place essentially in the substrate so that the simplification $\Phi^*_{Si} \simeq \Phi_{Si}$ is well verified. Hence a calibration curve of the intensity ratio k_2 and the film areal density can be obtained by inverting the integral (6.5) and is reported in Fig. 6.6(b) together with the ±20% confidence interval due to the calculation of the PFXP. The working interval for areal density measurement is limited by too small k_2 ratios since the ionization inside the substrate

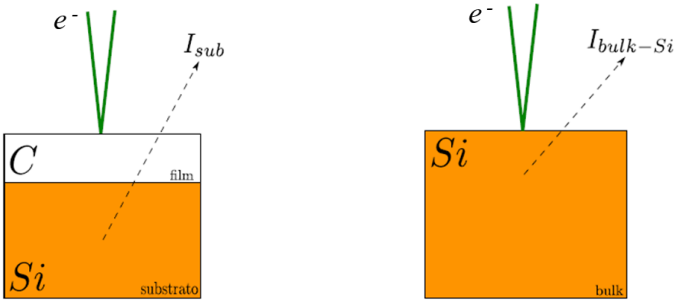

(a) Film/substrate (b) Reference

Figure 6.7: *Methodology proposed by Bentzon&Nielsen.*

is not sufficient either for the large film thickness or for the low electron energy. Hence k_2 must belong indicatively to the range 0.25-0.85 to give an areal density within the $\pm 20\%$ confidence.
The second method presents some advantages with respect to the first one. First of all it does not require the film to contain X-ray emitting elements. Secondly it does not need a reference sample having the same composition of the film. Finally the method by Bentzon&Nielsen is inherently more reliable in measuring areal density of carbon films, since it does not rely on the X-ray emission which is an extremely unfavored process in carbon with respect to other relaxation mechanism.

7 Characterization of foam-attached targets

The present chapter is devoted to the presentation of the results dealing with the characterization of carbon foam layers attached to solid substrates. As already introduced and motivated in Section 6.3.1, the fabrication technique we have adopted to cope with this issue is Pulsed Laser Deposition (PLD), allowing for a fine control of the film nanostructure, a broad range of accessible materials for both film and substrate and an excellent adhesion between them since the former is not attached but directly grown on the latter. In Section 7.1 we will present first the PLD parameters we have exploited to produce the foams. Then in Section 7.2 we will show the characterizations performed on the foam samples: the structural properties, the morphology and the density measurements as a function of process parameters. Afterwards in Section 7.3 the foam-attached target assembling will be discussed.

7.1 Process parameters for foam production

After a series of test depositions, in order to reach highly porous and low density structures, we have arranged the PLD parameters as follows.

- Target-to-substrate distance is fixed at 8.5 cm;
- Laser fluence is fixed at 0.8 J/cm^2 by combining low energy (100 mJ) and defocussed spot on target (12.5 mm^2);

- Two different inert gases to fill the chamber in Fig. 6.3, He and Ar, within a pressure range of 0-1000 Pa;
- Different gas flow conditions have been adopted: (*i*) 0.03 mg/s (1 sccm) with direction transverse to the ablation plume axis; (*ii*) 0.03-3 mg/s (1-100 sccm) having direction parallel to the plume;
- The adopted substrates are different depending the foams are due to either characterization or ion acceleration. In the first case versatile, 500 μm thick Si<100> wafers are used, while in the second case we have deposited on Al foils of different thicknesses: 0.8, 1.5 and 10 μm.

7.2 Results of carbon foams characterizations

To achieve the deposition of highly porous films, we have mainly exploited laser fluence and inert gas pressure in the chamber as the most suitable process parameters to control the energy of the ablated species. We have set the fluence at 0.8 J/cm^2, well below the values exploited so far in literature to obtain porous carbon with PLD, falling in the range 2-120 J/cm^2 [137, 155, 160–166]. We have also adopted two different inert gases, He and Ar, lighter and heavier than carbon respectively. First Raman spectra analysis is presented in Section 7.2.1, morphology measurements are discussed in Section 7.2.2, while mean density measurements will be presented in Section 7.2.3.

7.2.1 Carbon foam structural properties

Raman spectroscopy is one of the most used techniques for the structural characterization of carbon materials. In the case of amorphous carbon (a-C), composed by a mixture of sp, sp^2 and sp^3 phases, the interpretation of Raman data is not straightforward. In fact Raman spectrum is always characterized by the prevalence of the two peaks of sp^2 phase, the G and D peaks, even if sp^2 fraction is low as in diamond-like carbon (DLC). This is due to the large polarizability of the conjugated π bonds at the sp^2 sites [174]. Specifically the G mode, lying in the range 1500-1630 cm^{-1}, is the stretching mode of any sp^2 C-C pair, both in chains and rings. Therefore it does not require a local graphitic order to be visible. On the contrary the dispersive, disorder-activated D peak at about 1355 cm^{-1} (for green excitation) is associated to the breathing mode of aromatic six-fold rings, do that

it is strictly related to the number of these graphitic rings. From the intensity ratio of the two peaks $I(D)/I(G)$ it is possible to determine the coherence length L_a, a measure of the dimension of the ordered graphitic domains. Actually visible Raman spectra are controlled by the order, not by the amount of sp^2 phase and only indirectly by the sp^3 fraction [175]. Raman spectra for a selection of the PLD deposited carbon films are reported in Fig. 7.1(a) and Fig. 7.2(a), for the case of He and Ar pressure, respectively. They present very similar spectra, typical of a-C, with prominent broad G and D peaks. Some differences in peak position and relative intensity are visible, more evident in the case of depositions in He. To quantitatively characterize this behavior, following [175] we have used a fitting procedure involving an asymmetric Breit-Wigner-Fano (BWF) function for the G peak and a Lorentzian function for the D peak. We have extracted the G position (relative to the maximum of the BWF curve) and the ratio of the peak heights $I(D)/I(G)$. Their variation with He and Ar pressure are reported in Fig. 7.1(b,c) and Fig. 7.2(b,c) respectively. Following the interpretation proposed in [175], these data indicate that the deposited material corresponds to a nearly pure sp^2 network of topologically disordered graphitic domains, containing odd-membered rings, with some loss of aromaticity, and few chain-like structures. A lowering of the G position with respect to graphite (1583 cm^{-1}) is observed, due to the

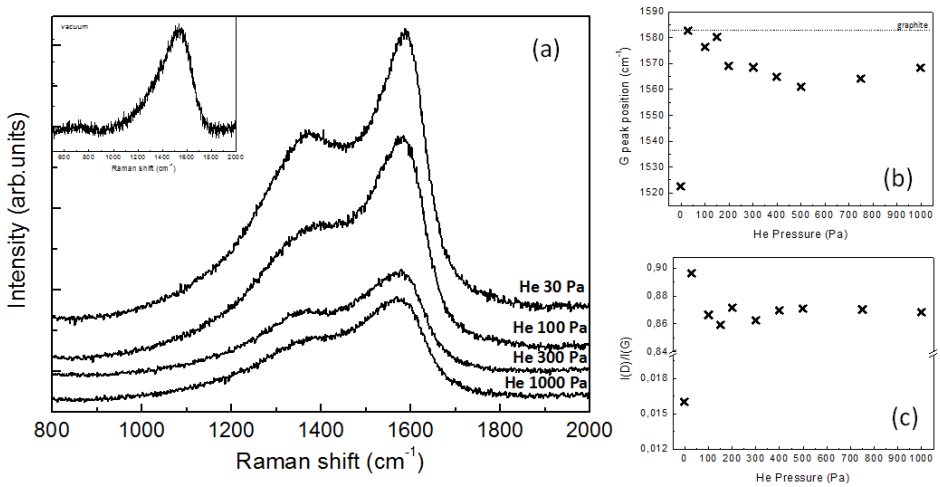

Figure 7.1: *(a) Raman spectra for films deposited in helium at 30, 100, 300, 1000 Pa. In the inset Raman spectrum of the film deposited in vacuum conditions. Variation of the G position (b) and $I(D)/I(G)$ ratio (c) with He pressure.*

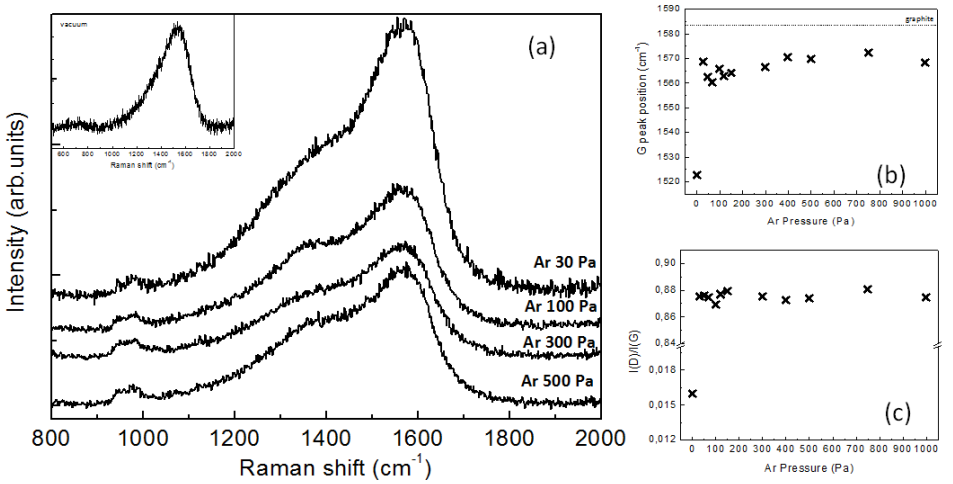

Figure 7.2: *(a) Raman spectra for films deposited in argon at 30, 100, 300, 500 Pa. In the inset Raman spectrum of the film deposited in vacuum conditions. Variation of the G position (b) and $I(D)/I(G)$ ratio (c) with Ar pressure.*

bond weakening in the distorted rings and the consequent softening of the vibrational density of states (VDOS). The relatively low value for $I(D)/I(G)$, about 0.86, corresponding to L_a below 2 nm, confirms this picture. Raman analysis then suggests that a similar structure of nanoparticles is achieved for almost all the deposition conditions, in which similar single nanoparticles may aggregate in the plume if a sufficient gas pressure is present. Only for films deposited at low He pressure Raman spectra show G positions close to the graphite value and a higher $I(D)/I(G)$, suggesting the formation of larger nanocrystalline graphitic domains, probably due to the larger kinetic energy of the nanoparticles arriving onto the substrate. A limit case is the deposition in vacuum conditions giving a compact film (see inset in Figs. 7.1 and 7.2), where the crystalline order is completely lost as indicated by the very low $I(D)/I(G)$ value and the strong G peak softening.

7.2.2 Carbon foam morphology

In Fig. 7.3 top view SEM images of samples at different pressures in He and Ar are presented. For the case of He (Figs. 7.3(a)-(c)) we observe a complete coverage of the surface with a morphology at the mesoscale getting opener with increasing pressure (30, 100 and 500 Pa respectively). In particular, below 100 Pa a cauliflower-like shape is

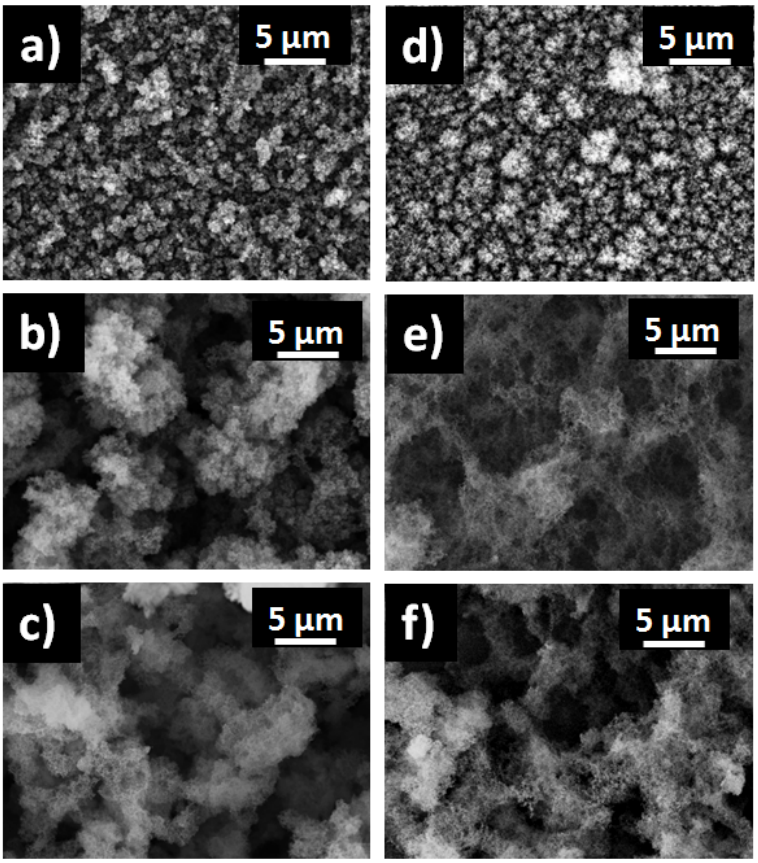

Figure 7.3: *Top-view SEM images of samples in He (left column) and Ar (right column) at different pressures: (a) and (d) 30 Pa, (b) and (e) 100 Pa, (c) and (f) 500 Pa.*

observed, while above 100 Pa a disordered more open morphology appears, which remains qualitatively the same till 1000 Pa (not shown), where a complete coverage of the substrate is still observed. In Fig. 7.4 an illustrative HR-STEM image of the deposits shows the presence of small nanoparticles, having dimensions of the order of ∼10 nm, which represent the elementary constituents of the deposited films if a sufficient gas pressure is present. One can observe that film morphology is due to the aggregation of the elementary nanoparticles in larger particles (see Fig. 7.5), which then assemble with each other giving rise to the observed mesoscale. While below 100 Pa (Fig. 7.5(a)) these particles are compact, at higher pressures (Fig. 7.5(b)) they look more porous and voids-rich, with mean pore size of tens nm. Further details

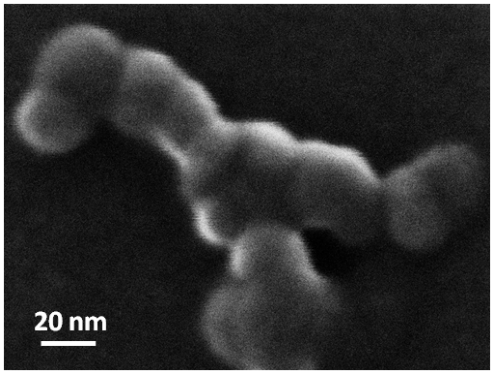

Figure 7.4: *Illustrative HR-STEM image of a foam sample deposited in 200 Pa He atmosphere.*

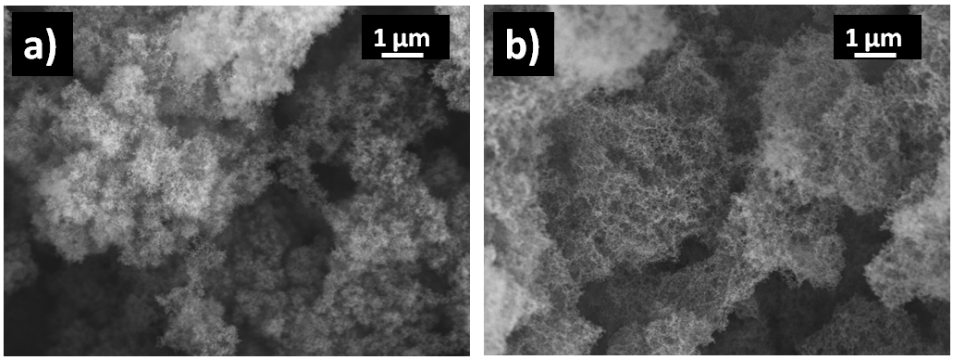

Figure 7.5: *SEM images of mesoaggregates that mediate the morphology on a scalelength between meso and nanoscale in He deposits. (a): 100 Pa. (b): 500 Pa*

on film morphology can be obtained by cross-section SEM images in Figs. 7.6(a)-(c) for the same depositions. Below 100 Pa ((a)-(b)) a cauliflower-like growth is evident, whereas at higher pressure (c) the morphology evolves towards a more disordered configuration.
In Figs. 7.3(d)-(f) plane view SEM images for the case of Ar are reported. We still observe the morphology opening with increasing pressure. In particular one can notice a sharp transition from a cauliflower-like morphology at 30 Pa (d) to a randomly distributed isotropic one (f). An intermediate regime occurs around 100 Pa (e), in which the morphology is already random but connected to form a network. Above 500 Pa the coverage of the substrate starts to be partial. SEM cross-section images (Figs. 7.6(d)-(f)) clearly show a transition at 30 Pa, from an anisotropic morphology to an isotropic one. Compared to

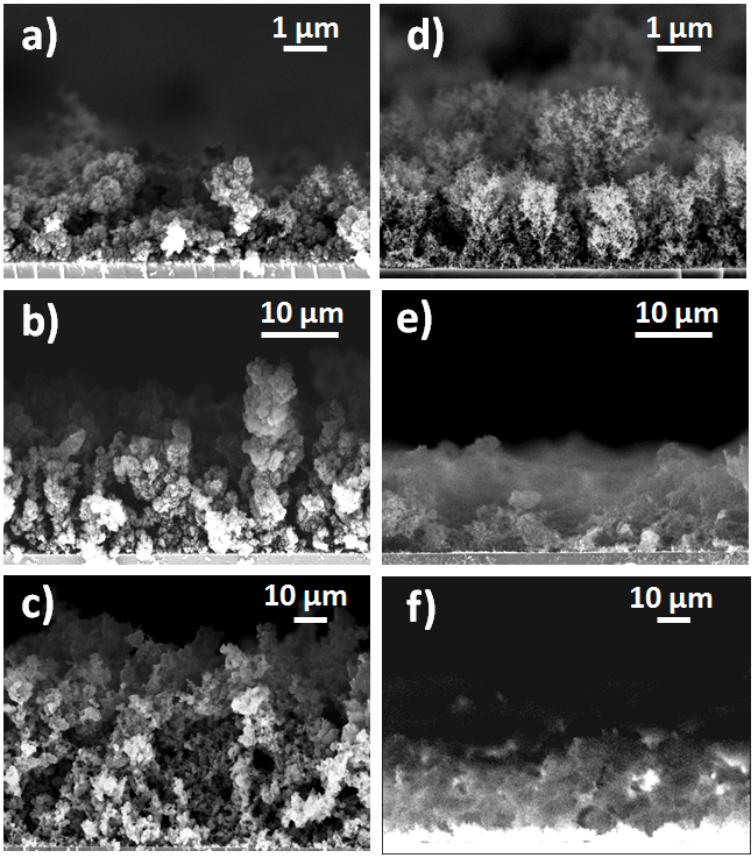

Figure 7.6: *Cross section SEM images of samples in He (left column) and Ar (right column) at different pressures: (a) and (d) 30 Pa, (b) and (e) 100 Pa, (c) and (f) 500 Pa.*

the case of He, the elementary nanoparticles here do not assemble in larger particles but in random chains which crumple self-similarly till the mesoscale.
Hence the deposited foam layers show different properties, depending on the adopted process parameters. As a common feature, at the *nanoscale* ∼10 nm carbon nanoparticles appear to be the elementary constituents (see Fig. 7.4) if a sufficient gas pressure is present. This is in fairly satisfactory agreement with the kinetic theory reported in [176], resulting in an estimate of about 4-5 nm. The small difference is likely to be due to the different laser pulse durations (ps in [176], ns in our experiments). These nanoparticles are likely to be formed by the aggregation in plume of small carbon clusters and atoms ablated by the

laser. Actually it is known that carbon atoms and mainly odd carbon cluster cations, between C_3^+ and C_{15}^+, are formed after graphite ablation using the same wavelength (532 nm) and fluence (<1 J/cm^2) of our depositions [177, 178]. If the chamber is filled with a buffer gas these species may aggregate in larger nanoparticles inside the plume. Films constituted by similar nanoparticles have been observed in literature studies of PLD carbon depositions in gas atmosphere [137,155,179]. As a further support, our Raman spectra in Figs. 7.1 and 7.2 look similar to those reported in [180] where nanoparticle-assembled carbon films, produced with supersonic cluster beam deposition, have been discussed.

While the structure at the nanoscale seems not to be significantly

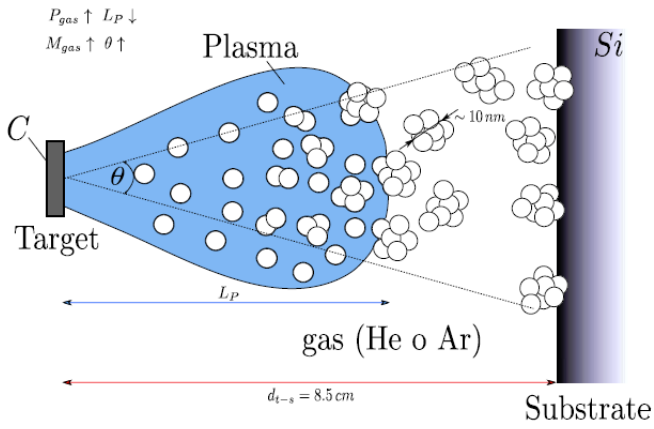

Figure 7.7: *Illustrative picture of the out-of-plume deposition regime adopted in this work.*

affected by the deposition conditions, different aggregations at the *mesoscale* have been observed to occur. This is mainly due to the action of the buffer gas atoms on carbon nanoparticles, as a function of gas type and pressure. These parameters mainly affect the energy of the expanding nanoparticles and their spatial distribution due to scattering processes, which ultimately determine the observed differences in film mean density and morphology. The adopted set of process parameters (i.e fluence, target-to-substrate distance) allows to place our deposition conditions within the so-called "out-of-plume" regime, in which the substrate stands always well outside the ablation plume (see sketch in Fig. 7.7). This configuration leads to the deposition of nanoparticle-assembled films with very open morphology [181]. The

expansion dynamics of the species can be splitted into two stages, inside and outside the plume, both significantly affected by the type of buffer gas. Inside the ablation plume the carbon species expansion can be described as a supersonic hydrodynamic motion [182]. Above 30-50 Pa most gases enter the acoustic regime; here, the shock front velocity in He is larger than in Ar [183], correspondingly influencing the energy of carbon species leaving the plume. As nanoparticles pass beyond the shock front, they lose their kinetic energy by collisions with gas molecules and they are therefore transported by diffusion to the substrate. Due to the difference in mass between Ar and He, the former has a larger stopping power on carbon nanoparticles with respect to the latter. As a result, nanoparticles in Ar arrive onto the substrate having a smaller amount of energy with respect to the case of He. Moreover collisions with Ar atoms lead the expanding nanoparticles to scatter at large angles more likely than in He, making them deposit in a more isotropic fashion, also partially preventing their arrival on the substrate.

From the obtained results, films around 100 Pa in Ar represent an optimal condition for the deposition of a low density foam with isotropic morphology. Starting from this condition, we have investigated the effect of other process parameters, namely the direction and intensity of gas flow in the chamber, on the foam surface uniformity at the mesoscale. Different Ar flows have been considered, namely 0.9, 1.8, 3 mg/s (30, 60, 100 sccm respectively) with direction parallel to the ablation plume axis, instead of 0.03 mg/s (1 sccm) having direction transverse to the plume. In Fig. 7.8 plane view SEM images of two of

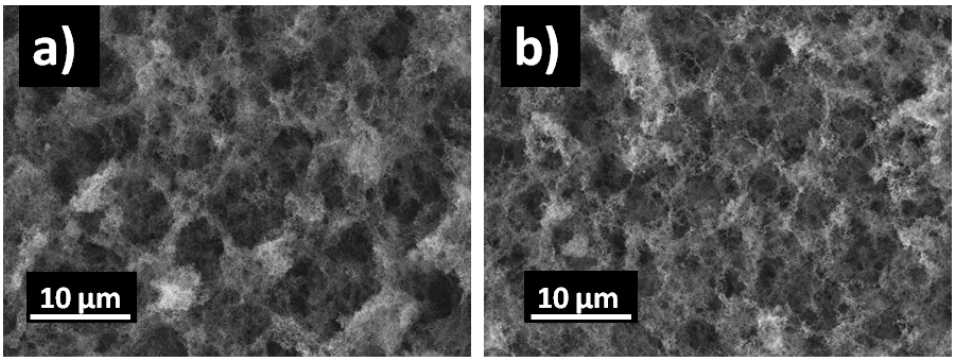

Figure 7.8: *SEM plane view images of foam samples deposited respectively with 0.03 mg/s (1 sccm) (a) and 3 mg/s (100 sccm) (b) longitudinal gas flow.*

these samples are reported: switching from 0.03 mg/s (1 sccm) (a) to 3 mg/s (100 sccm) (b), a significant improvement in surface uniformity is evident. From a rough estimate on the basis of the micrographs in Fig. 7.8, the typical non-uniformities appear to stay within $\sim$1 μm. A more quantitative estimate of the foam inhomogeneity scalelength has been performed by means of the innovative EDXS procedure presented in Section 6.3.3. EDXS scans have been performed on different areas corresponding to different magnifications (see Appendix A for technical details). For each magnification five distinct regions of the sample

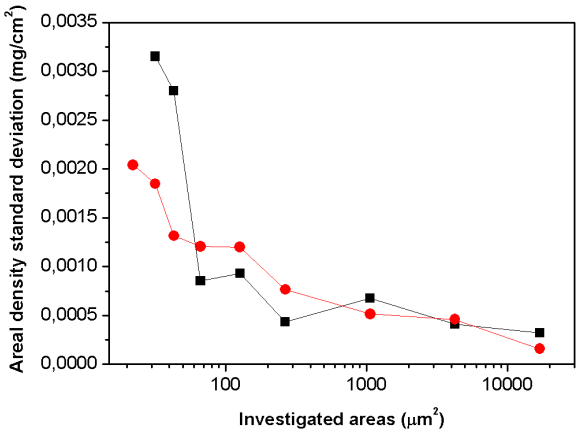

Figure 7.9: *Standard deviations of areal density measurements calculated for each sampled area on foam films deposited in two different configurations of Ar flow: 1 sccm transverse flow in black squares and 100 sccm parallel flow in red dots.*

have been explored. In each one the k_2 ratio has been recorded and an areal density has been calculated through the inversion of integral (6.5), since, as pointed out in Section 6.3.3, the method by Bentzon&Nielsen is inherently more reliable than the one by Bishop&Poole. If the deviation between the different areal density measurements is low, that means the sampled area size exceeds film inhomogeneity scalelength. On the contrary, when measurements start to differ significantly from one another, the sampled area S becomes comparable with the typical scale of inhomogeneity, which can be roughly estimated as $\sqrt{S}$. To this end standard deviations between areal density measurements in these samplings has been calculated and reported in Fig. 7.9 as a function of each sampled area spanning from 20000 down to 20 μm^2. The standard deviation of the measured areal density with respect to

its mean value is below 40% for areas above 65 μm^2 in the 1 sccm flow sample (black squares), while for the 100 sccm sample (red dots) it remains below 40% down to 20 μm^2. In the first case the inhomogeneity scalelength lies around 8 μm, while in the second is <5 μm. This evidence confirms the qualitative statement that by modifying the gas flow configuration, the foam layer becomes more homogeneous.

7.2.3 Carbon foam density measurements

In this Section two kinds of mean density measurements as a function of He and Ar pressure are reported; they both combine areal density and mean thickness estimates (as explained in Section 6.2). The former has been assessed by two different techniques, QCM and EDXS while the latter has been evaluated via a cross-section SEM analysis. The values are compared to the critical density by assuming a completely ionized C plasma (i.e. only C^{6+} species is considered). We start our analysis by reporting separately in Fig. 7.10 thickness and areal density as a function of gases pressure, corresponding to a given 20 min deposition time. Film thicknesses in He increase constantly till 500 Pa, where a $\sim$80 μm saturation value is reached (see Fig. 7.10(a), red squares). The corresponding deposited thicknesses in Ar are reported in Fig. 7.10(a) (black circles). They show a linear increase till 100 Pa with a saturation after this pressure at a value around 20 μm for 20 min depositions. Due to scarce coverage after 500 Pa, no measurements of mean thickness are reported. As a common feature between the two gases, by increasing the deposition time a linear increment of thickness is found for pressures up to 100 Pa, while above this value the film growth rate diminishes, and a calibration curve is then needed in order to correctly extrapolate the film growth. The deposited areal density measurements as a function of gases pressure are reported in Fig. 7.10(b). QCM results for He produced foams (red squares) evidence a slight decrease till 750 Pa, ranging from 0.1 to 0.01 mg/cm^2 and going below the detection limit at 1000 Pa. The corresponding estimates of mean density, reported in Fig. 7.11 (red squares), ranges, according to a power law fit, from 2200 ($\sim$ graphite density) down to few mg/cm^3. QCM results for foams deposited in Ar (black squares in Fig. 7.10(b)) are observed to strongly decrease with Ar pressure. Above 150 Pa the microbalance was not able to recover any signal. Mean density is therefore estimated till 150 Pa reaching a value around 1 mg/cm^3 (see black squares in Fig. 7.11). From these results one can state that QCM rep-

resents a reliable technique to measure film areal density, as long as the film grows sufficiently homogeneous. At increasing porosity these conditions are no longer verified and this is mainly the reason why in Fig. 7.11 QCM measurements drop off after ∼100 Pa in Ar (black dots) and ∼300 Pa in He (red dots), down to nonphysical values (i.e. around and below air density). The physical explanation for this failure lies in the fact that quartz-crystal is located inside the deposition chamber and then the amount of material arriving on it strongly depends on deposition conditions. As we have discussed in Section 7.2.2, at increasing gas pressure, especially with Ar, an increased large angle scattering of the carbon nanoparticles is present. Moreover, as resumed in Section 6.3.2, at increasing film porosity a decoupling between quartz crystal and film may happen. Hence we can state that, at increasing pressure, the material depositing on the quartz represents an progressively less significant statistical sample of the real film.
EDXS areal density measurements, performed by processing the K_α intensities with the more reliable Bentzon&Nielsen method, show a slightly constant trend with pressure. Foams in He (blue triangles in Fig. 7.10(b)) stay around ∼0.06 mg/cm^2, while those in Ar (green triangles in Fig. 7.10(b)) are fixed around ∼0.01 mg/cm^2. This translates into density estimates where the decreasing trend is only due to thickness increase. Hence a density trend saturation is observed around 1 n_c both for He and Ar deposited films, reported in Fig. 7.11 as blue

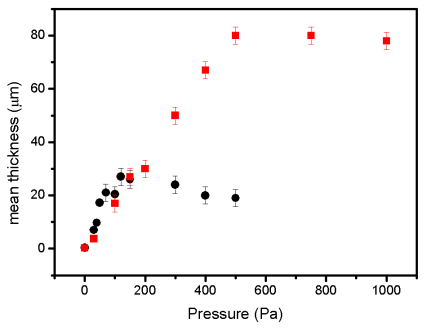

(a) Mean thickness measured by SEM as a function of He (red squares) and Ar (black circles) pressure values after 20 min deposition time.

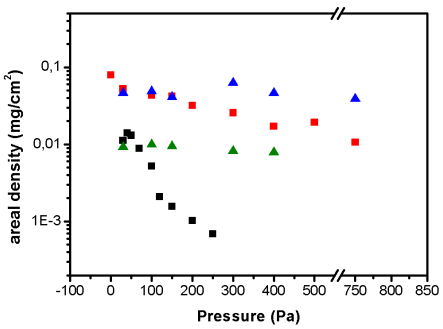

(b) Deposited areal density measured at the same He and Ar pressure values by means of QCM (in red and black squares, respectively) and EDXS (in blue and green triangles, respectively).

Figure 7.10: *Thickness and areal density separated measurements.*

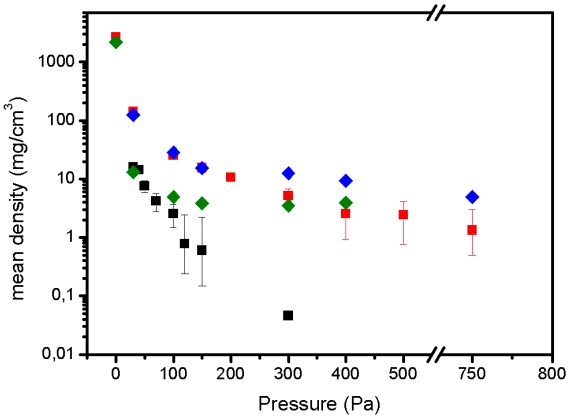

Figure 7.11: *Mean density of the deposits measured at increasing pressures in He and Ar, by means of QCM (in red and black squares, respectively) and EDXS (in blue and green triangles, respectively).*

and green diamonds, respectively. While for pressures below 100 and 300 Pa in Ar and He respectively there is a very good agreement with QCM results. EDXS then is found to be a reliable technique to measure film areal density within 3 orders of magnitude broad range, being not affected by deposition conditions in the chamber as QCM is.

7.3 Foam-attached target assembling

As resumed at the beginning of the Chapter, all the characterizations reported so far have been obtained depositing foams on the versatile model substrate, Si<100>. Nevertheless, samples produced for ultraintense laser ion acceleration need further constraints. The materials used so far for typical TNSA experiments might be metals like e.g Al, Pd or polymers as Mylar or plastics, having thicknesses in the range 100s nm - 10s μm. As discussed in Section 2.1.2, an optimal thickness to accelerate protons has been observed to exist using solid films, according to the particular laser conditions owned by each system. The endorsed facility to carry out the testing of our foam-attached targets is the UHI100 laser system owned by the IRAMIS service at CEA-Saclay (France), for which the ideal conditions of target material/thickness are reached with 1.5 μm thick Al foils. Hence we have arranged foam depositions onto these new substrates, for which mainly two open ques-

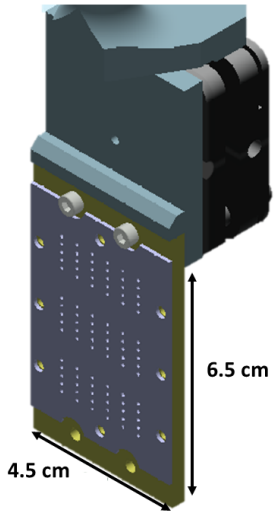

(a) Target holder located in the interaction chamber of UHI100 laser facility at CEA-Saclay.

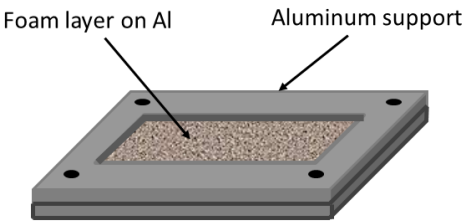

(b) Target support for foam depositions and transport to CEA-Saclay.

Figure 7.12: *Components for foam-attached targets assembling.*

tions have arisen. First of all we have verified by using the EDXS method that changing the substrate material, the foam areal density does not vary significantly. On this basis we have reasonably assumed that the foam thickness remains unchanged switching from Si to Al as well, since a SEM cross-section investigation does not hold for foams on Al, being the latter too fragile to be fractured without affecting the deposits, with respect to 500 μm thick Si wafers. Thus, an accurate density measurement could be achieved on these samples in the same fashion. The second issue has been to project a proper support for Al substrates, to be adopted both during depositions and logistics. Since the target holders for UHI100 are designed as shown in Fig. 7.12(a), where the target must be inserted in between the two plaques, we have engineered our target supports as shown in Fig. 7.12(b). In this way the Al substrate is inserted in the sandwich support and located in the PLD chamber where is covered by the desired foam layer measuring in the central area 4.5×2.5 cm, so to fit in the target holder. Then it can be packed and transported safely to the lab. Different foam-attached target configurations have been produced: we have exploited Al foils of different thicknesses (0.7, 1.5 and 10 μm) and covered by foams with densities and thicknesses ranging between 1-2 n_c and 10-20

μm respectively. The different densities have been achieved by tuning Ar pressure between 50 and 100 Pa, respectively, while the thicknesses have been calibrated with proper deposition times. Furthermore, the modified Ar flow configuration (30 sccm and parallel direction) has been adopted to optimize the surface uniformity in order to achieve an inhomogeneity scalelength <5 μm.

8

Test of foam-attached targets for laser-driven ion acceleration

This Chapter represents the concluding issue of the PhD work reported in the present thesis. Here the results coming from a campaign devoted to the test of foam-attached targets in a laser-ion acceleration experiment are reported. Although the presented results are still under analysis and interpretation, a clear message already emerges, that is the existence of experimental conditions for which the foam-attached targets described in Chapter 7 allow to achieve enhanced maximum proton energies. To clearly identify which are these conditions, in Section 8.1 we first introduce the experimental apparatus and process parameters we have adopted. Then, in Section 8.2, we will show some illustrative experimental results, well summarizing the general outcome of the experimental analysis. Finally, in Section 8.3, a brief insight into the ongoing theoretical interpretation of the results, carried on by means of 2D-PIC simulations, will be presented.

8.1 Experimental setup

To test our foam-attached target, whose production and characterization is discussed in Chapters 6 and 7, an experimental campaign at UHI100 laser facility owned by CEA-Saclay has been conducted. The experiment has been approved and developed within the frame of the "Laserlab-Europe" programme [184]. The laser energy after the am-

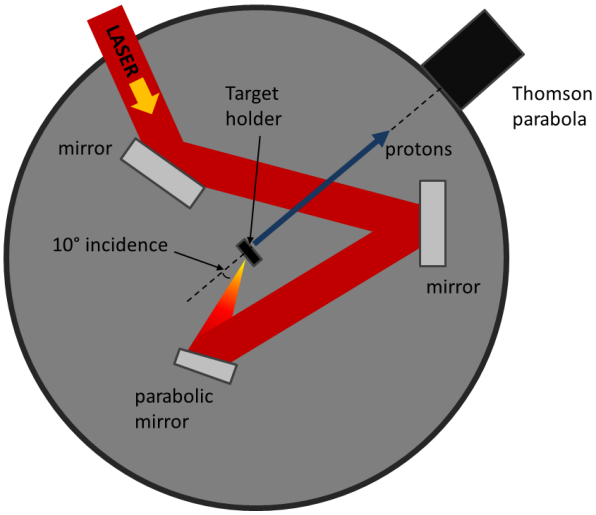

Figure 8.1: *Schematic view of the interaction chamber, showing the adopted experimental setup for 10° incidence.*

plification stages is 2 J, then reduced to 0.7 J, after the optical path to the target. The focalization is achieved by means of a $f/2$ off-axis parabola with focal length of 200 mm. The spot in the focal position is well fitted with a gaussian curve in both transverse directions and has an average FWHM of ~ 3.5 μm, containing approximately 0.5 of total laser energy on target. The pulse duration is of 25 fs and the ASE can be reduced by a factor $\sim 10^{12}$ thanks to a double plasma mirror (see Appendix A.1). The maximum intensity in the focal spot reachable with such a laser system has been estimated to be $\sim 3 \times 10^{19}$ Wcm^{-2}, which corresponds to a normalized vector potential $a \simeq 4.5$. In order to investigate a broad parameter domain and interaction conditions, pulse intensity has been varied within the range $\sim$2$\times$10^{16} - 3$\times$10^{19} W/cm^2. The change in intensity has been achieved either by varying laser energy (0.2 - 2 J), duration (25 - 250 fs) or focal spot ($\sim$ 3.5 - 150 μm FWHM). The angle of incidence has been varied from 45° to 10° (see sketch in Fig. 8.1). A smaller angle of incidence has not been feasible because an even partial back-reflection of the laser pulse would have seriously damaged the optics. To address the possible role played by the laser contrast, both $\sim 10^{12}$ (HC, with DPM installed) and 10^7 (LC, without DPM) setups have been considered. Also depending on this, various target configurations have been adopted, using Al foils, either 1.5 or 0.75 μm thick, and foam attached targets where the Al foils (1.5

or 0.75 μm) are covered with foams having densities and thicknesses ranging between 1-2 n_{cr} and 10-20 μm, respectively (see Section 7.3). In the second configuration thicker Al foils has to be used since the ASE is larger, so is the optimal thickness. Without foam, 5 to 50 μm thick Al foils have been used, while foam-attached targets with 20 μm/1n_{cr} foam deposited on 12 μm Al foils are adopted. The result is a collection of a wide set of maximum proton energy data and in the next section some illustrative results giving the clear message of this experiment will be shown. In particular we are presenting some experimental results of maximum proton energy as a function of laser intensity where the change in intensity has been achieved in different manners, either by changing the focal spot size or by attenuating the laser energy content. Every parameter scan has been performed on both a bare Al target and on a foam-attached one, in order to obtain a comparative study able to discriminate the behavior of laser-driven ion-acceleration in presence of such a multi-layer target configuration. It is worth noting that, for the adopted conditions, the obtained results would fall mostly outside the intensity ranges explored in the PIC simulations by Nakamura et al and Sgattoni et al discussed in Section 5.2.

8.2 Ion acceleration results

In Fig. 8.2 we show in HC configuration the scan of maximum proton energy as a function of laser intensity, obtained by irradiating a 1.5 μm thick Al foil (blue squares) and a foam-attached target with foam thickness and density 12 μm and 1n_{cr} (red circles), respectively. Intensity has been varied by changing the FWHM focal spot in the range $\sim$ 3.5 - 150 μm: dealing with a quasi-gaussian beam (thanks to wavefront corrections, see Appendix A.2), the spot size is symmetrical on the propagation axis with respect to the focal position. In Fig. 8.3 a comparative study between the same targets have been performed in HC configuration, but the intensity has been changed by tuning the energy content of the laser pulse between 0.2 to 2 J, while remaining in the focal position. Finally in Fig. 8.4 a comparative study similar to that of Fig. 8.2 is reported, but obtained in LC configuration, where Al foils are labeled by blue squares and foam-attached targets by red circles. Then the adopted targets are different, in particular the bare Al is 12 μm thick while the multi-layer one has a 1n_{cr}, 22 μm thick

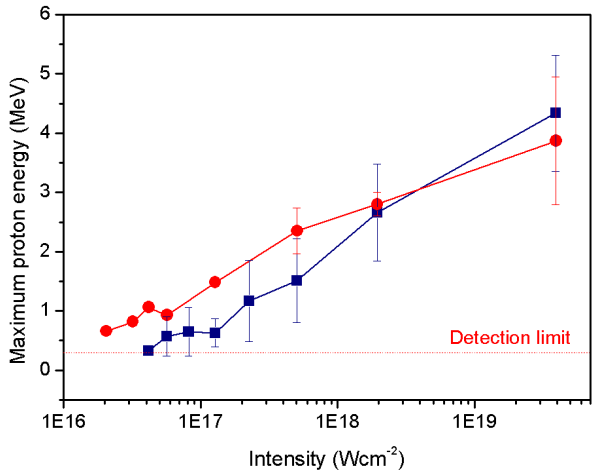

Figure 8.2: *Comparison between ordinary (blue squares) and foam-attached targets (red squares). Maximum proton energy as a function of laser intensity, varied by changing the focal spot size on target. HC configuration.*

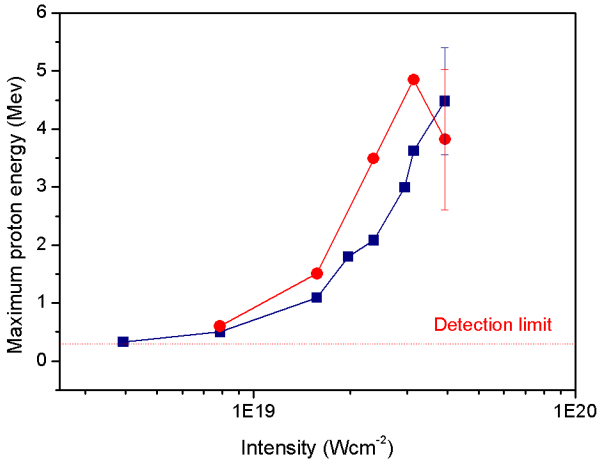

Figure 8.3: *Comparison between ordinary (blue squares) and foam-attached targets (red squares). Maximum proton energy as a function of laser intensity, changed by varying the focal spot size. LC configuration.*

foam attached onto a 12 μm thick Al foil. As a common feature among the different experimental configuration we have explored, we have measured with foam-attached targets proton maximum energies in excess of 1 MeV even at intensities well below 10^{18}W/cm^2. That proves that, while it has been widely reported so far in the literature as the TNSA onset, by exploiting the smart target configuration studied

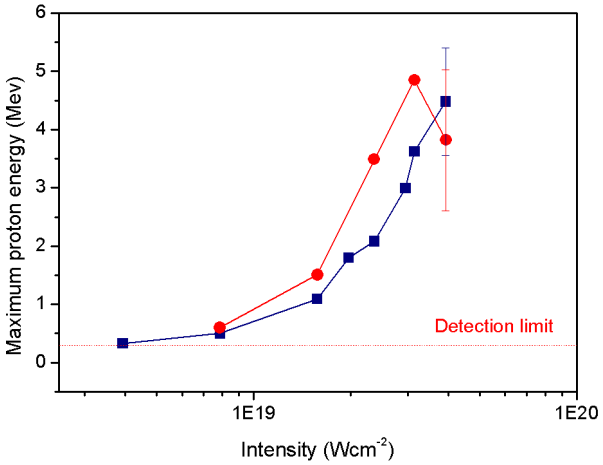

Figure 8.4: *Comparison between ordinary (blue squares) and foam-attached targets (red squares). Maximum proton energy as a function of laser intensity, changed by tuning the energy content. HC configuration.*

and produced as reported in Chapters 6 and 7, MeV protons become accessible already with 10^{16}-10^{17} W/cm^2 laser intensities. In particular, we shall notice for the two defocalization cases in Figs. 8.2 and 8.3 (with HC and LC, respectively) that, from the highest intensity down to $\sim 10^{18}$ Wcm^{-2}, maximum proton energy does not depend only on the adopted target configuration, but on the combination of the various parameters. In fact, within this intensity regime, the measurements with foams might be slightly higher or lower than without. Afterwards, below $\sim 10^{18}$ Wcm^{-2}, a dominance of maximum proton energy obtained with foams attached is observed systematically, where the values obtained with solid targets fall below the detection limit of 300 keV soon after crossing that value. In Fig. 8.4 a narrower intensity range has been explored, since energy attenuation allows only to span the decade 3×10^{18}-3×10^{19} Wcm^{-2}. Here an enhancement of maximum proton energy by using foam-attached targets is more evident. Also at decreasing intensity the same trend of the two previous graphs is observed, although the scan has stopped before the onset value $\sim 10^{18}$ Wcm^{-2}. A remarkable aspect of this analysis is that the enhancement of maximum proton energy at low intensity is observed independently from the laser pre-pulse intensity, i.e. both at low and high-contrast. This can constitute a simplification of the experimental setup.

8.3 Preliminary interpretation of experimental results

The interpretation of the obtained experimental results is still ongoing during the draft of the present thesis. The key point of the physical explanation we are formulating is that at decreasing intensity, the foams are subject to a lower ionization degree. For this reasons we have performed numerical simulations adopting a lower density as the considered intensity falls below 10^{18} Wcm^{-2}. In this way, if at high intensity we have a slightly overdense plasma, as the intensity decreases the same plasma becomes underdense, due to the lower foam ionization. The laser pulse would then propagate through it, allowing for a volume and not surface interaction, which leads to the generation of energetic electrons and TNSA fields also below 10^{18} Wcm^{-2}. In particular we have performed some explorative 2D-PIC simulations using the code `ALaDyn` [119–121], where the laser pulse has λ=0.8 μm, a 25 fs FWHM duration and a gaussian intensity space profile. The normalized vector potential a has been varied between 4 and 0.5, corresponding to an intensity range of 5×10^{17} Wcm^{-2} and 3.5×10^{19}. The foam-attached targets have been designed with 3 layers: foam, solid and contaminants, while the target without foams only have the solid layer. The foam layers are initialized with 25 macro-ions (Z/A=1/3) and macro-electrons per cell, thicknesses 8-12 μm and densities of 2 and 0.66 n_{cr}. The solid foil is simulated with 25 macro-ions (Z/A=1/3) and 49 macro-electron per cell, thickness 0.5 μm and density of $40n_{cr}$. Finally the contaminants layer has 25 macro-protons and 9 macro-electrons per cell, 50 nm thickness and density of $10n_{cr}$. To estimate maximum ion energy the simulations have been stopped after 200 fs. In Fig. 8.5 we present proton maximum energy as a function of laser intensity, which has been varied between 6×10^{18} Wcm^{-2} and 3.5×10^{19} (a=2-4) by a change of focal spot size with energy kept fixed. The foam attached targets have been considered at different thicknesses (8-12 μm) and density of $2n_{cr}$. Here the impossibility to evince different behavior passing from a foam-attached target to a solid one is clear, meaning the maximum proton energy does depend on the particular combination of target and laser parameters. In Fig. 8.6 we have investigated a lower intensity range, i.e. 5×10^{17} Wcm^{-2}-2×10^{18} (a=0.5-1), where the focal spot is fixed and energy content is varied. The foam-attached targets have different thicknesses (8-12 μm) and density of $0.66n_{cr}$, in order to take into account the lower ionization state of the foams at low in-

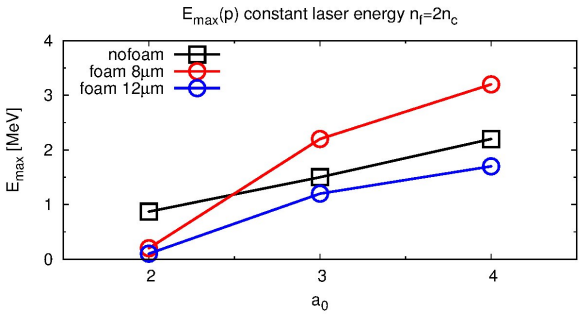

Figure 8.5: *2D-PIC results of maximum proton energy as a function of intensity (a=2-4), which has been varied by means of focal spot (3-12 μm). Foams have density of $2n_{cr}$ and different thicknesses: 8 μm (red circles) and 12 μm (blue circles). In black squares results from solid target are reported.*

tensities. Here a completely different picture is evinced. In fact there

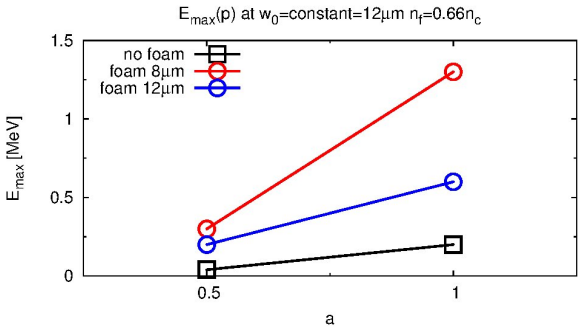

Figure 8.6: *2D-PIC results of maximum proton energy as a function of intensity (a=0.5-1), varied by means of laser energy. Foams have density of $2n_{cr}$ and different thicknesses: 8 μm (red circles) and 12 μm (blue circles). In black squares results from solid target are reported.*

appears a clear enhancement of maximum proton energy in presence of a foam-attached target, where the corresponding values obtained with ordinary solid targets are almost negligible. In this manner we have shown with numerical simulations that, in agreement with the results shown in Section 8.2, two regimes appear at changing laser intensity. Above 10^{18} Wcm^{-2} and up to 3.5×10^{19} no clear distinction between targets with and without foams is observed, while below 10^{18} Wcm^{-2} the foam-attached targets lead to an enhanced proton acceleration regime, with respect to solid ones. The preliminary numerical results confirm the physical explanation, according to which a not com-

plete ionization of the foam as the laser intensity decreases, leads to an effective plasma density lower than the ones estimated assuming a C^{6+} plasma.

9 Conclusions and perspectives

The availability of increasingly higher laser intensities has caused the traditional distinction between disciplines as laser physics, plasma physics and radiation-matter interaction to vanish, giving rise to a new and intriguing research field. Thanks to the development of increasingly more powerful laser facilities, an ultra-relativistic regime of the interaction might be reached nowadays, since the intensities are able to reach values up to 10^{22} Wcm^{-2}. Among the the physics that emerges from such extreme conditions, an important role is played by the so-called laser-plasma "secondary sources", leading to the emission of both radiation and particles as a consequence of the laser-matter interaction. In fact the generation of high-order harmonics of the incident laser light has been observed, as well as the acceleration of electrons and ions up to energies of 1 GeV and tens of MeV, respectively. In particular the latter phenomenon is observed when mainly solid density foils are used as targets, with thicknesses ranging from few tens of nanometers to few tens of microns, and linearly polarized pulses ranging in intensity from 10^{18} to 10^{21} W/cm^2 are exploited. Laser-driven ion acceleration is the leading thread of the present thesis, whose contents have been divided into three parts. In Part I the subject has been resumed by starting in Chapter 1 from a review on the physics of laser-plasma interaction at high intensities. Afterwards in Chapter 2 we have focalized our attention to the experimental evidences coming from laser-ion acceleration experiments. The typical accelerated ion beams have been observed to own peculiar properties as exponential energy spectra with a multi-MeV cutoff,

high beam quality thanks to small transverse and longitudinal emittance, and a high number of ions per bunch. The more robust and experimentally observed acceleration mechanism is the so-called Target Normal Sheath Acceleration (TNSA) which unfolds the process into three main parts. Once the laser pulse impinges onto the target, electrons efficiently absorb electromagnetic field energy and expand, setting up a strong charge separation. The huge electric fields that follow charge separation might be felt by heavier particles such as the ionized contaminants on the non irradiated surface, being then accelerated. Thanks to their properties different promising applications have been studied. Each application requires the optimization of one or more beam parameter and in general these are different passing from one another. To optimize a quantity a general procedure would be to get a fundamental theoretical understanding of the system, combined with novel experimental approaches. In the present work we have focused our attention on one of proton beam parameters, that is to say the maximum energy. The goal has been tackled by a two-steps methodology.

As a first task, in Part II we have studied theoretically the TNSA process, by classifying and implementing several analytical simplified models. In Section 3.1 the fluid, quasi-static and hybrid approaches have been discriminated on the basis of the process time scale considered. The goal has been to compare the predicting capability of these models on the basis of the maximum ion energy in a series of experimental configurations contained in a database from the literature (see Section 3.2). These results can assume a particular interest in the light of the future generation of laser systems [C2,C3]. Since a reliable model may be able to predict the regimes reachable with higher performances lasers. To this end, in Section 4.1, we have further developed an analytical model having shown a suitable predicting capability in the previous comparison [C1]. Thanks to its straightforward implementation, we have extensively investigated the effective dependence of maximum ion energy on laser irradiance, which represents one of the most interesting and challenging issues in TNSA. In particular, an effective almost linear relation is evidenced as characterizing a significant number of results, achieved in various laser facilities (see Section 2.1.1). We have both interpreted experimental data sets and drawn analytical and numerical PIC scaling laws, in order to clarify the role played by laser energy content in the calculation of the intensity. To this end, as shown in Section 4.2, different scalings emerge whether

the energy is varied or kept fixed, linear in the first case, radical in the second [C4]. A deep theoretical knowledge of the maximum energy dependencies might represent a general approach to predict the ion acceleration regimes achievable with a new generation of laser facilities with improved performances.
Part III of this PhD thesis has dealt with the possibility to get a smarter experimental setup to enhance maximum proton energy only by manipulating target properties, without involving an improvement of laser performances. Since the energy gained by TNSA-accelerated ions is inherently limited by the fraction of laser energy absorbed by the target, the road we have followed has been to improve the energy transfer from laser pulse to target electrons, by means of a low-density coverage of the illuminated side of the solid target. In fact a larger EM energy absorption within the so-called "near-critical" regime has been recently demonstrated, that means make the laser pulse to interact with a medium having densities around few mg/cm^3 for incident wavelengths $\lambda \sim 1\mu$m. Hence, we have engineered a multi-layered target configuration composed by an ordinary solid foil covered by a micrometric near-critical layer on the surface illuminated by the laser, in order to enhance the laser absorption, fast electron generation and finally the TNSA accelerating fields. The first stage of the work has been to produce experimentally such a low-density material. In Sections 6 and 7 we have shown the set of parameters we have exploited for the production by means of pulsed laser deposition (PLD), a technique which allows a fine control of density, thickness and adhesion to a solid substrate of the low-density film [C5]. Since density characterization constitutes a crucial point, a new technique exploiting energy dispersive X-ray spectroscopy (EDXS), alternative to the most common one of quartz-crystal microbalance (QCM), has been developed and implemented (see Section 6.3.3). This has allowed to obtain a more reliable estimate of multi-layered targets mean density within the regime of interest. These targets have been tested in the framework of a Laserlab experimental campaign in CEA/SLIC Saclay laser facility, in which clear enhancement of ion acceleration within the explored sub-relativistic intensity range has been revealed [C6]. This part of the work owns a two times original mark, since on one side for the first time we have been able to produce a film material having a tunable mean density within three orders of magnitude. On the other hand the foam-attached targets so obtained have led to a TNSA-like ion acceleration within a so far "inhibited" intensity range, i.e. below

the widely known onset of 10^{18} Wcm^{-2}.
Further developments in this direction would certainly lead to a finer control of foam thickness and density, in order to observe the parametric dependence of maximum proton energy on foam parameters obtained by PIC simulations in Section 5.2. An important future development would be to test our foam-attached targets at the maximum achievable intensities in order to proof the enhancement of the maximum TNSA performances observed so far. Moreover such future experiments would allow to state whether this target configuration constitutes a possible way to reach or not maximum proton energies and conversion efficiencies suitable for the forthcoming applications.

The original contents of this PhD thesis have led to the publication of the following peer-reviewed papers, ordered by year:

[C1] M. Passoni, L. Bertagna, A. Zani "Target normal sheath acceleration: theory, comparison with experiments and future perspectives" *New Journal of Physics* vol. 12, 045012 (2010).

[C2] C. Perego, A. Zani, D. Batani, M. Passoni "Extensive comparison among target normal sheath acceleration theoretical models" *Nuclear Instruments and Methods in Physics Research A* vol. 653, 89-93 (2011).

[C3] C. Perego, D. Batani, A. Zani, M. Passoni "Target normal sheath acceleration analytical modeling: comparative study and developments" *Review of Scientific Instruments* vol. 83, 02B502 (2012).

[C4] A. Zani, A. Sgattoni, M. Passoni "Parametric investigations of target normal sheath acceleration experiments" *Nuclear Instruments and Methods in Physics Research A* vol. 653, 94-97 (2011).

[C5] A. Zani, D. Dellasega, V. Russo, M. Passoni "Ultra-low density carbon foams produced by pulsed laser depositions" *Carbon*, in press (2013).

[C6] M. Passoni, A. Zani, A. Sgattoni, T. Ceccotti, D. Dellasega, V. Floquet, A. Macchi, in preparation.

A

Experimental

In this Appendix we report some more technical details on the experimental techniques and methodologies adopted in this thesis work. First we present in Section A.1 the techniques exploited to produce and characterize carbon foams. Then in Section A.2 we are going to review the instrumentation at the UHI100 laser facility at CEA Saclay.

A.1 foams production and characterization

A.1.1 Pulsed Laser Deposition (PLD)

In Pulsed Laser Deposition (PLD) a target is placed in a vacuum chamber and is ablated by energetic laser pulses. After the interaction with a laser, the surface of the target melts and the ablated particles (molecules, atoms, ions, electrons and small aggregates) expand towards a substrate assuming the classical shape called "plume". The film grows on a substrate, placed in front of the target. The process can occur in vacuum or in presence of an inert or reactive background gas. Films properties might be other than those of the target and they do depend on process parameters, such as buffer gas type and pressure, substrate temperature, laser energy density (fluence) and repetition rate, chemical composition and structure of target and substrate, and target to substrate distance. The principal drawback of this technique concern the the geometry of the substrate; the deposited film has uniform thickness over a small area (few cm^2) and the surface must have a simple geometry. The other disadvantage is the presence of particulates

(micrometer size droplets) on the film surface, that may vary in a non-controllable way the films properties. On the contrary PLD is widely used in basic research field because it allows to study many classes of materials (metals and dielectrics, high- and low-melting, with complex stoichiometry,...) changing deposition parameters in large ranges. In the following we briefly discuss the principal phenomena that occur in PLD process, namely laser-target interaction[1], plasma formation and expansion and film deposition. The laser pulse penetration depth in a material is:

$$l_a = \frac{1}{\mu} \tag{A.1}$$

where μ is the material absorption coefficient which depends on radiation wavelength. The interaction between laser and target induces thermal and non-thermal processes being characterized by different time scales. In particular non-thermal processes (such as electron and phonon excitation) occur in the first stages of interaction. The equilibrium is restored in the material through electron-electron and electron-phonon collisions. Time scale of the former is of the order of 1-100 fs, while in the latter case few order of magnitude larger. When a ns laser is used, these processes occur during pulse duration: it is possible to describe the interaction through a one temperature model and the state of the system is described using the temperature distribution of the material. The heat diffusion depth in a material, considered homogeneous and isotropic, is:

$$l_\tau = 2\sqrt{D \cdot \tau_L} \tag{A.2}$$

where D is the diffusion coefficient and τ_L is the pulse duration. If $l_a > l_\tau$ a congruent ablation[2] takes place, while if $l_a < l_\tau$, such as in the case of metals, the laser energy is transported over the penetration depth through thermal diffusion. In general, for low fluence values, constituent materials are only excited, while for fluence values greater than a threshold value (that depends on the material) plasma formation occurs. The expanding plasma can absorb an amount of laser pulse energy (plasma shielding) due to inverse bremsstrahlung. In this

[1]The intensities are low compared to those discussed in Chapter 1, say in the range 10^9-10^{13} Wcm^{-2}

[2]From the ablation mechanism point of view, the congruent ablation threshold fluence represents the limiting fluence between the thermal evaporation of the material surface to an explosive ablation with an unidirectional expansion of the plume; in the congruent ablation process the relative concentration of species within the plasma plume remains unchanged for successive laser pulses and equal to those of the target.

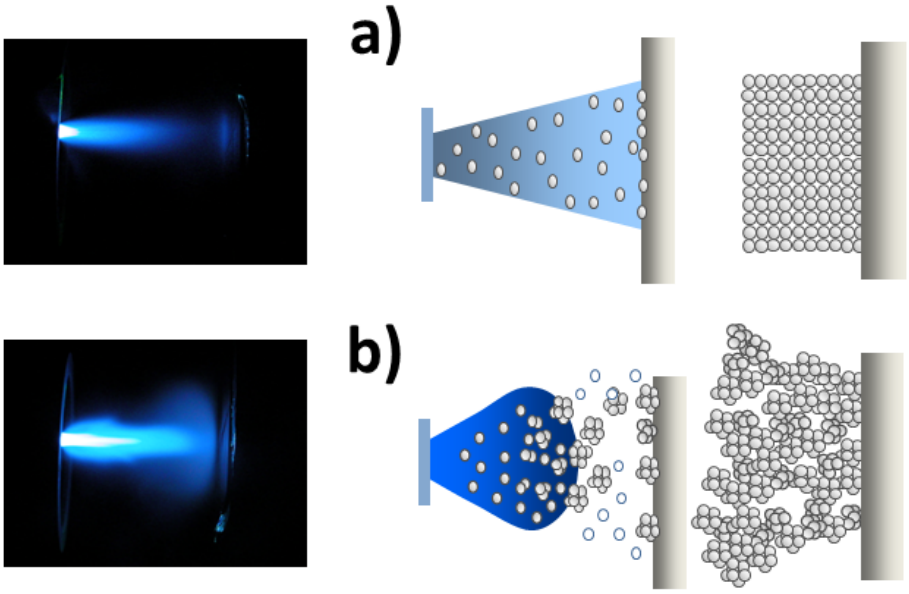

Figure A.1: *Typical ablation plumes of Al:ZnO either in vacuum (a) or in O_2 (b) atmosphere.*

process a photon is absorbed by a free electron under the field of an atom or ion (to preserve momentum conservation). Ionization degree can be calculated using Saha equation. From melted region of the target liquid droplets of different dimension might be ejected due to the recoil pressure. Plume expansion in the vacuum is almost linear (vs. time) and depends only on the velocity of the ablated particles when they escape from the target. The observed fluorescence is weak and it originates from plume inner core; the spatial distribution is strongly forward directed and does not change during plume expansion (see Fig. A.1(a).

The presence in the deposition chamber of a chemically inert gas at a given pressure affects the plume expansion and modifies important process features such as spatial distribution, deposition rate and kinetic energy distribution of the deposited particles. The fraction α of energy loss in a collision between an ablated particle and a buffer gas atom depends on their relative masses, m_1 and m_2:

$$\alpha = \frac{2m_1m_2}{(m_1 + m_2)^2} \tag{A.3}$$

Chemically reactive gases, such as O_2, N_2 and H_2, are employed to deposit oxides, nitrides and hydrides starting from metallic or dielectric target. In general, increasing gas pressure plume fluorescence raises due to particle collisions both in the expansion front and in the body, plume edge is better defined as a result of the presence of a shock wave front, and the plume is slowed down and spatially confined (see Fig. A.1(b)).
Three distinct pressure regimes have been identified, each of which is characterized by a specific behavior of the plume [185]:

1. a low-pressure "vacuum-like" regime with a forward directed flow and a reduced scattering of the ablated species,

2. a transition regime with strong momentum transfer to the background gas and formation of a shock wave, and

3. a regime characterized by diffusion of the ablated particles at high pressure.

Film growth mechanism can be divided in two classes: atom by atom or cluster assembling, depending on collisional phenomena that take place during plume expansion. In the case of atom by atom growth mechanism, the physical modeare those valid for the other deposition technique, such as thermal evaporation and Chemical Vapor Deposition (CVD) (even if kinetic regimes can be different and other phenomena can occur, such as implantation, sputtering). Otherwise, at sufficiently high gas pressure, collisions can lead to cluster aggregation in the plume. In this case film formation is determined by the kinetic energy per atom in the cluster. As a consequence, it is possible to deposit films with different morphologies, from compact to highly porous. In addition to the buffer gas, the most important process parameters are laser pulse characteristics and substrate temperature. Short wavelength pulses deposit larger energy density per volume in the target. High values of fluence induce high ionization degree and energy of the ablated species, but also high ejection of particulate. Generally, depositions are performed using a fluence slightly greater than the threshold. Increasing spot dimension the plume has better directionality, normal to the target, and the expulsion of particulate and solid fragments is reduced, due to smaller boundary effect. The incident angle is generally 45°: it is a good compromise between spot size and plasma shielding process. In this case the plume is not perfectly perpendicular to the target but is slightly tilted in the laser direction. Substrate temper-

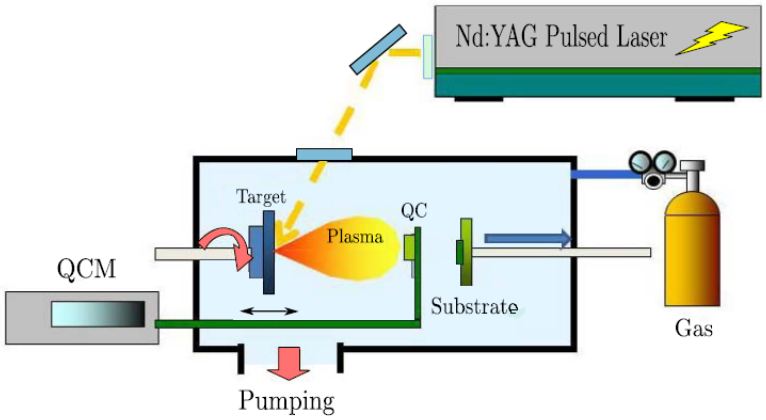

Figure A.2: *Illustrative scheme of the pulsed laser deposition apparatus at NEMAS laboratories - Politecnico di Milano*

ature influences growth mechanism, because a high temperature can favor the diffusion of the species on the substrate. Moreover, substrate heating can lead to crystalline films, due to re-organization of deposited atoms in a most stable structure. An excessive temperature can cause the re-evaporation of the film or of the more volatile elements: the temperature can be a way to select the deposited compounds.
To deposit foam layers it is reasonable to adopt low fluence and high gas pressure. The substrate is placed outside the plume so that the species expansion is diffusion-limited. A sketch of the PLD configuration adopted here is reported in Fig. A.2.

A.1.2 Quartz Crystal Microbalance (QCM)

QCM is a device able to measure the mass attached on the surface of a piezoelectric quartz crystal. The operation of the QCM is based on the inverse piezoelectric effect. A quartz single crystal, properly cut and put in contact with two electrodes, is stimulated by a periodic signal coming from the connected electric circuit. In correspondence to certain frequencies, an electromechanical resonance condition is reached and the whole system behaves like a stable quasi-harmonic oscillator. The proper frequencies of the quartz crystal depend on its shape and size and vary according to the working temperature. The adopted quartz crystals, so-called AT-cut, are thin (thickness less than 1 mm) and disk shaped with a diameter of 0.8 cm. The electrodes are given

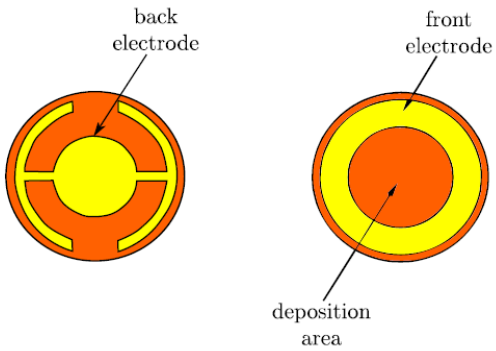

Figure A.3: *Sketch representing a typical AT-cut quartz crystal covered by gold electrodes adopted in the QCM.*

by thin gold films deposited on the parallel faces of the crystal, as shown in Fig. A.3. The quartz crystal is mounted inside a metallic support, through which is connected to the electronic circuit of the microbalance. To perform areal density measurement, the oscillating crystal is placed inside the deposition chamber at the same place usually occupied by the substrate. To reproduce as much better as possible the substrate absolute position, the device can be translated along the target-substrate axis and tilted around it (see Fig. A.2). The mass deposited on the crystal provokes a slightly decrease of the oscillating frequency, which is recorded by the acquisition chain and transduced into a film thickness variation, once the material density and the impedance coupling parameter Z between crystal and film are given as input.

A.1.3 Scanning Electron Microscopy (SEM) and Energy Dispersive X-ray Spectrometer (EDXS)

Description

In the SEM a source of electrons is focused in vacuum into a fine probe that is rastered over the surface of the specimen. As the electrons penetrate the surface, a number of interactions occur and can result in the emission of electrons or photons from the surface. The principal images produced in the SEM are of four types: secondary electron images, (primary) backscattered electron images, transmission electron images and elemental X-ray maps. Secondary and backscattered electrons are conventionally separated according to their energies. These types of

radiation are produced by different mechanisms. When a high-energy primary electron interacts with an atom, it undergoes either inelastic scattering with atomic electrons or elastic scattering with the atomic nucleus. In an *elastic* collision with an electron, some amount of energy is transferred to the other electron. If the transferred energy exceeds the work function of the material, the emitted electron can exit the solid. Secondary electrons have generally energy less than 50 eV. Most of them are produced within the first few nm of the surface, while the few remaining, being produced much deeper inside the material, undergo additional inelastic collisions, which lower their energy and trap them in the solid. Backscattered electrons are primary electrons that have been scattered elastically (with no kinetic energy loss) by the nucleus of an atom, although these collisions may occur after the primary electrons has already lost some of its energy to inelastic scattering. The probability of elastic scattering increases strongly with atomic number, approximately as Z^2, because heavier atoms have a much stronger positive charge on the atomic nucleus, and decreases as the electron energy increases, approximately as $1/E^2$. Therefore, the higher the atomic number of a material, the more likely it is that backscattering will occur. An additional electron interaction in the SEM occurs when the primary electrons collide *inelastically* with an atom which eject a core electron. The excited atom will decay to its ground state by emitting either a characteristic X-ray photon or an Auger electron. The X-ray emission signal can be sorted by energy in an energy dispersive X-ray detector (EDS) or by wavelength with a wavelength spectrometer (WDS). These distributions well characterize the elements they belong to and these signals can be used to produce elemental images that show the spatial distribution of particular elements in the field of view. The primary electrons can travel considerably distances before losing enough energy through collisions to be no longer able to excite X-ray emission. This means that a large volume of the sample will produce X-ray emission for any position of the smaller primary beam (1 nm diameter), and consequently the spatial resolution is about 0.5 μm. The energies used are those relative to the K, L and M electron shells.

Instrumentation

The SEM used during this work is a high resolution FESEM (Filed Emission) Zeiss Supra 40 based on Gemini column, equipped with an

Oxford EDS. The apparatus and the scheme of the column with all the detectors are presented in Figs. A.4(a) and A.4(b), respectively. The main features of the instrument are the electron column containing the electron source (i.e. the gun), the magnetic and electrostatic focusing lenses, the sample vacuum chamber at the bottom of the column and the electronics console. The Gemini column utilises the Schottky thermal field emission source, that is a ZrO/W<100> filament operating at 1800 K. The acceleration voltage is in the range 0.1-30 kV, the specified resolution is 1.3 nm at 15 kV and the specimen stage is connected to five motors (x, y, z, tilt, rotation). The detectors present in the chamber are 5: the first 4 provide different kind os sample imaging, while the last one acquires the X-ray spectra emitted after inelastic collisions of electrons.

- backscattered electrons (BSE) detector for primary electrons: to enhance compositional contrast and crystal orientation (in our case it is an ASB detector-Angle Selected Backscattered); it is placed at the bottom of the gun;
- In-lens detector for secondary electrons: electrons emerging from the sample surface are attracted and accelerated by the positively biased electrode of the beam booster; it produces high resolution morphological images and it is placed in the gun;
- Everhart-Thornley chamber detector for secondary electrons: it collects remaining electrons that are not captured by the beam booster(especially at large working distances) or second generation secondary electrons. It typically depicts compositionally enhanced contrast combined with some surface information and it is placed in the chamber;
- STEM detection system: it comprises two parallel diode detector surfaces (Bright Field BF and Dark Field DF); it provides high-resolution (HR) information concerning the elementary constituents of the carbon foams;
- EDXS detector: it is a Si(Li) detector protected by a Be window. It can work in two modes: "PointID" mode provides point measurements chosen by the user on a given sample area; "Analyzer" mode allows the user to choose an area on a sample, of any size, and to record the mean X-ray signal given by an excitation scan over the given area. Its energy resolution is of the order of 10 eV.

(a) Overview of the SEM-EDS apparatus

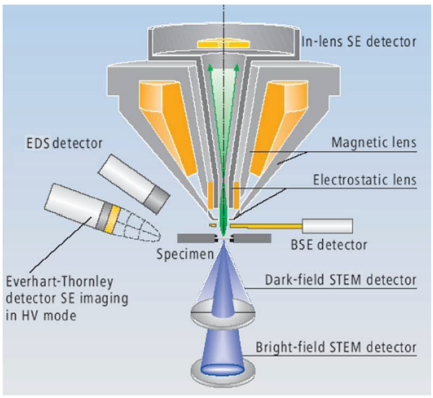

(b) Detailed scheme of the components inside the SEM

Figure A.4: *SEM-EDS instrumentation.*

A.1.4 Raman spectroscopy

Description

When a light beam impinges on a sample it is scattered over the whole solid angle and a small fraction of this radiation has wavelength different from the incident radiation: this was the phenomenon observed in 1928 by C. V. Raman. The essentials of the Raman scattering experiment are very simple. When the spectrum of the radiation scattered by the sample illuminated with monochromatic light of frequency ω_0 is analyzed, it is found that it consists of a very strong line at the frequency ω_0, as well as of a series of much weaker lines with frequencies $\omega_0 \pm \omega_{vib}(\mathbf{q})$, where $\omega_{vib}(\mathbf{q})$ are optical phonon frequencies (see Fig. A.5(a)). The strong line centered at ω_0 is due to *elastic scattering* of photons and is known as *Rayleigh* scattering. The series of weak lines at $\omega_0 \pm \omega_{vib}(\mathbf{q})$ originates from *inelastic scattering* of photons by phonons and constitutes the Raman spectrum. The Raman bands at frequencies $\omega_0 - \omega_{vib}(\mathbf{q})$ are called *Stokes* lines, those $\omega_0 + \omega_{vib}(\mathbf{q})$ are known as *anti-Stokes* lines. In first order Raman scattering only optical phonons with $\mathbf{q} \simeq 0$ are involved; this is a consequence of momentum conservation. The Stokes and anti-Stokes lines have different origin. The electric field of the incident radiation distorts the electron clouds that make up the chemical bonds in the sample, storing some energy (Fig. A.5(b)). The stored energy reradiated at the same frequency forms the Rayleigh peak. A small portion of the stored energy is transferred to

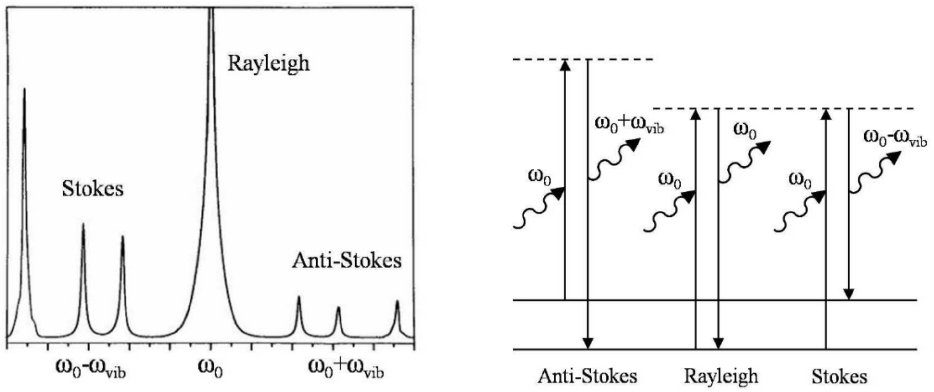

(a) Scheme of the Rayleigh and Raman scattering

(b) Typical Raman spectrum with the Rayleigh peak at the center and the Stokes and Anti-Stokes peaks.

Figure A.5: *Basic features of Raman scattering.*

the sample, exciting the vibrational modes: the emitted Stokes lines are a direct measure of the vibrational frequencies of the sample. The reverse process also occurs: vibrations that have been excited by thermal processes, can be annihilated by coupling with the incident beam and can add their energies to that of the source. This anti-Stokes scattering depends on the existence of thermally activated vibrations and its intensities are strongly temperature dependent. Therefore the Stokes lines are measured, generally by differences with respect to the Rayleigh line (whose frequency is defined as the "zero").

Instrumentation

To analyze the vibrational modes of carbon foams, the InVia Raman spectrometer produced by Renishaw. The exciting radiation is produced by a Ar^+ laser by Laser-Physics, able to emit at different wavelength, namely 514.5, 488 and 457 nm wavelength. The former has been adopted for our measurements. Spectra have been acquired by a 1800 greeds/mm grating, a super-notch filter (cutoff at 100 cm^{-1}) and a Peltier-cooled CCD camera, allowing a spectral resolution of about 3 cm^{-1}. Care has been taken to avoid laser damage of the foams during Raman measurements, by keeping laser power below 1 mW.

A.2 Ion acceleration using foam attached targets

A.2.1 The UHI100 laser facility

CEA Saclay owns a laser installation having 70 TW nominal power and called UHI100. The principal characteristics of this laser chain are resumed in Table A.1. The principal oscillator is a 25 fs Ti:Sa laser,

Table A.1: *Principal characteristics of the UHI100 laser chain.*

Pulse energy content	2 J
Pulse energy on the target	0,72
Pulse duration (FWHM)	25 fs
Intensity on target (theoretical)	1.7×10^{20} Wcm^{-2}
Normalized vector potential (theoretical)	8.9
ASE intensity	1.7×10^{8} Wcm^{-2}
Contrast ratio with DPM	$\sim10^{12}$

which is amplified in between stretching and compression by three stages up to an energy content of 2 J. The contrast-ratio is controlled by means of a double plasma mirror (DPM), whose scheme is reported in Fig. A.6. It allows to obtain a contrast ratio of the order of 10^{12}. A rough estimate of the energy attenuation factor suffered by the beam throughout the whole laser chain can be performed by considering the transmittance of each component. The compressor introduces typically a 20% attenuation, the double plasma mirror 50% and the rest of the optical components 10% overall. Energy and pulse duration might be varied in a pretty simple way by means of an attenuator and a delay line, respectively. The focalization of the laser beam, originally having

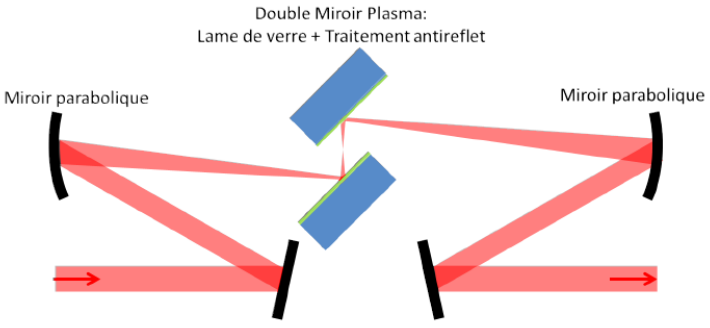

Figure A.6: *Schematic view of the double plasma mirror.*

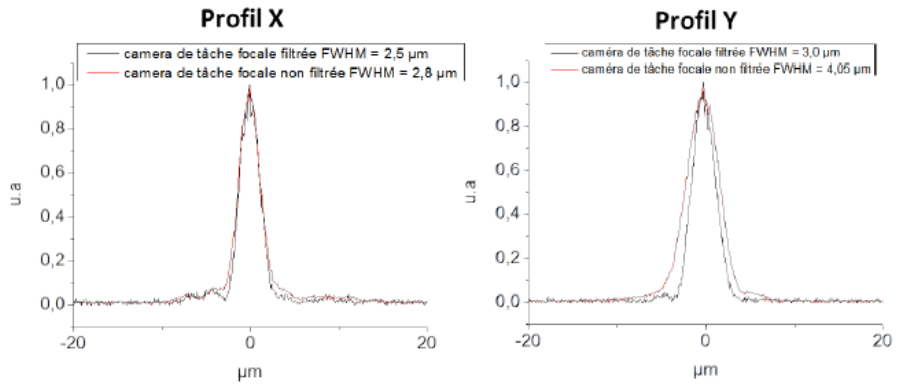

Figure A.7: *Transverse intensity profiles of the focalized pulse intensity.*

a 8 cm diameter, is achieved by means of a $f/2$ off-axis parabolic mirror with a 200 mm focal length. A fine control of the wavefront flatness through a deformable mirror allows to obtain focalizations down to the diffraction limit. To this end Fig. A.7 reports the beam intensity profiles in the focus, which are well fitted with gaussian curves having an average waist w_0 ~3 μm (corresponding to a FWHM=$\sqrt{2\ln 2}$ ~3.5 μm). Since the energy content in the waist is ~40%, we will assume that 50% of energy is contained in the FWHM. In order to perform a scan in focal spot size, an excursion of the target of ±1.2 mm from the focal position has been achieved, and the variation of the spot size far from the focal position $w(z)$ is well fitted (R^2=0.98) with the equation for a gaussian beam propagation:

$$w(z) = w_0\sqrt{1 + M^2\left(\frac{\lambda z}{\pi w_0^2}\right)} \tag{A.4}$$

where M^2 is a figure of merit expressing the ratio between waist and divergence in the real and gaussian beam. By assuming it as free fitting parameter we have obtained a value very similar to that expected for the UHI100 facility (M^2=2.3). In this way we have translated the displacements from focal position into FWHM values, namely 3.5-150 μm. Hence, the investigated intensities range from the highest, 3×10^{19} W/cm^2, down to ~2×10^{16} W/cm^2.

(a) Picture of the interaction chamber interior

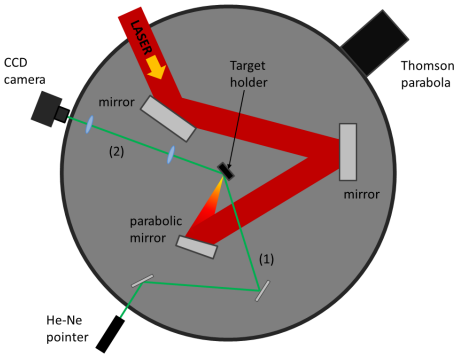

(b) Schematic representation with the diagnostic system inside the chamber

Figure A.8: *The interaction chamber at the end of UHI100 laser chain.*

A.2.2 Diagnostic systems

The diagnostic system inside the interaction chamber is aimed both at detecting protons and monitoring the pointing of the target in each shot. In Fig. A.8(a) we show a picture of the interaction chamber taken during the substitution of the targets. While in Fig. A.8(b) an illustration explaining the diagnostic scheme is presented. Optical line (1) redirects an He-Ne laser pointer on the target in the focal position. The image on the target is recorded both by a optical fiber camera located nearby and by the CCD camera at the end of imaging path (2). These two images of the are taken at different angles from target normal and, if compared, they can give a reliable pointing system. The proton detection is achieved by means of the Thomson parabola which is a mass spectrometer able to deflect a particle after passing through a magnetostatic plus an electrostatic field as shown in Fig. A.9(a) The amplitude of particle deviation from its original trajectory only depends on its energy and charge-to-mass ratio. At the entrance of the parabola a collimator (pinhole) is placed, and the smaller its diameter, the better the resolution in energy of the parabola. A particle deviation from its trajectory is detected by means of two micro-channel plates (MCP) coupled to a phosphore screen. The working principle of a MCP is to create an electronic cascade following the arrival of each ionizing particle. The cascade is amplified passing through the plates, since a high voltage is applied between the two poles. The electrons exiting the MCPs are visualized by a phosphorescent screen converting

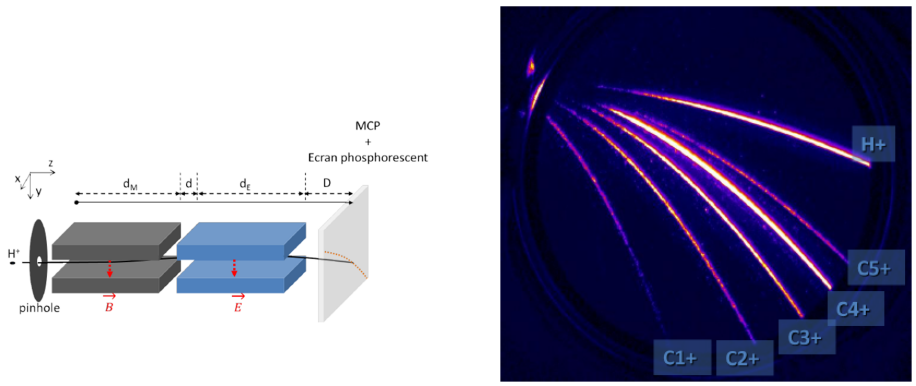

(a) Schematic representation of a Thomson parabola.

(b) Typical traces of different ionic species recorded by a Thomson parabola.

Figure A.9: *Description of a Thomson parabola.*

their energy into visible photons. In Fig. A.9(b) we report the typical ionic traces recorded by a Thomson parabola. The acquisitions of such an image, if followed by a proper comparison with the theoretical traces, gives an optimal estimate of the type and energy spectrum of the accelerated particles.

Bibliography

[1] T. H. Maiman. Stimulated optical radiation in ruby. *Nature*, 187:493–494, 1960.

[2] F.J. McClung and R.W. Hellwarth. Giant optical pulsations from ruby. *Journal of Applied Physics*, 33(3):828–829, 1962.

[3] L.E. Hargrove, R.L. Fork, and M.A. Pollack. Locking of hene laser modes induced by synchronous intracavity modulation. *Applied Physics Letters*, 5(1):4–5, 1964.

[4] Strickland D. and Mourou G. Compression of amplified chirped optical pulses. *Optics Communications*, 56(3):219 – 221, 1985.

[5] http://amplitude-technologies.com.

[6] http://coherent.com.

[7] R. Ganeev. High-order harmonic generation in laser plasma: Recent achievements. *Laser Physics*, 22:1177–1188, 2012. 10.1134/S1054660X12070031.

[8] U. Teubner and P. Gibbon. High-order harmonics from laser-irradiated plasma surfaces. *Review of Modern Physics*, 81:445–479, Apr 2009.

[9] T. Tajima and J. M. Dawson. Laser electron accelerator. *Physical Review Letters*, 43:267–270, Jul 1979.

[10] E. Esarey, C. B. Schroeder, and W. P. Leemans. Physics of laser-driven plasma-based electron accelerators. *Review of Modern Physics*, 81:1229–1285, Aug 2009.

[11] Z. Dangor A.E. Clayton C.E. Marsh K. A. Joshi C. Malka V. Darrow C.B. Danson C. Neely D. Walsh F.N. Modena, A. Najmudin. Electron acceleration from the breaking of relativistic plasma waves. *Nature*, 377:606–608, Oct 1995.

[12] WP Leemans, P Catravas, E Esarey, et al. Electron-yield enhancement in a laser-wakefield accelerator driven by asymmetric laser pulses. *Physical Review Letters*, 89(17), 2002.

[13] V Malka, S Fritzler, E Lefebvre, et al. Electron acceleration by a wake field forced by an intense ultrashort laser pulse. *Science*, 298(5598):1596–1600, 2002.

[14] J Faure, Y Glinec, A Pukhov, et al. A laser-plasma accelerator producing monoenergetic electron beams. *Nature*, 431(7008):541–544, 2004.

[15] CGR Geddes, C Toth, J van Tilborg, et al. High-quality electron beams from a laser wakefield accelerator using plasma-channel guiding. *Nature*, 431(7008):538–541, 2004.

[16] SPD Mangles, CD Murphy, Z Najmudin, et al. Monoenergetic beams of relativistic electrons from intense laser-plasma interactions. *Nature*, 431(7008):535–538, 2004.

[17] W. P. Leemans, B. Nagler, A. J. Gonsalves, et al. GeV electron beams from a centimetre-scale accelerator. *Nature Physics*, 2(10):696–699, 2006.

[18] A. Di Piazza, C. Müller, K. Z. Hatsagortsyan, and C. H. Keitel. Extremely high-intensity laser interactions with fundamental quantum systems. *Review of Modern Physics*, 84:1177–1228, Aug 2012.

[19] A Macchi, M Borghesi, and M Passoni. Ion acceleration by superintense laser-plasma interaction. *Reviews of Modern Physics*, page in press, 2013.

[20] BM Hegelich, BJ Albright, J Cobble, et al. Laser acceleration of quasi-monoenergetic MeV ion beams. *Nature*, 439(7075):441–444, 2006.

[21] M Hegelich, S Karsch, G Pretzler, et al. MeV ion jets from short-pulse-laser interaction with thin foils. *Physical Review Letters*, 89(8), 2002.

[22] P. McKenna, F. Lindau, O. Lundh, et al. Low- and medium-mass ion acceleration driven by petawatt laser plasma interactions. *Plasma Physics and Controlled Fusion*, 49(12B):B223–B231, 2007.

[23] H Schwoerer, S Pfotenhauer, O Jackel, et al. Laser-plasma acceleration of quasi-monoenergetic protons from microstructured targets. *Nature*, 439(7075):445–448, 2006.

[24] RA Snavely, MH Key, SP Hatchett, et al. Intense high-energy proton beams from petawatt-laser irradiation of solids. *Physical Review Letters*, 85(14):2945–2948, 2000.

[25] Koichi Ogura, Mamiko Nishiuchi, Alexander S. Pirozhkov, et al. Proton acceleration to 40 MeV using a high intensity, high contrast optical parametric chirped-pulse amplification/Ti:sapphire hybrid laser system. *Optics Letters*, 37(14):2868–2870, 2012.

[26] TE Cowan, J Fuchs, H Ruhl, et al. Ultralow emittance, multi-MeV proton beams from a laser virtual-cathode plasma accelerator. *Physical Review Letters*, 92(20), 2004.

[27] M Borghesi, A Schiavi, D H Campbell, et al. Proton imaging: a diagnostic for inertial confinement fusion/fast ignitor studies. *Plasma Physics and Controlled Fusion*, 43(12A):A267, 2001.

[28] M Borghesi, DH Campbell, A Schiavi, et al. Electric field detection in laser-plasma interaction experiments via the proton imaging technique. *Physics of Plasmas*, 9(5):2214–2222, MAY 2002.

[29] L. Romagnani, J. Fuchs, M. Borghesi, et al. Dynamics of electric fields driving the laser acceleration of multi-mev protons. *Physical Review Letters*, 95:195001, Oct 2005.

[30] M Borghesi, S Bulanov, DH Campbell, et al. Macroscopic evidence of soliton formation in multiterawatt laser-plasma interaction. *Physical Review Letters*, 88(13), APR 1 2002.

[31] M Borghesi, SV Bulanov, TZ Esirkepov, et al. Plasma ion evolution in the wake of a high-intensity ultrashort laser pulse. *Physical Review Letters*, 94(19), 2005.

[32] L. Romagnani, S. V. Bulanov, M. Borghesi, et al. Observation of collisionless shocks in laser-plasma experiments. *Physical Review Letters*, 101(2), JUL 2008.

[33] J D Lawson. Some criteria for a power producing thermonuclear reactor. *Proceedings of the Physical Society B*, 70(1):6–10, 1957.

[34] https://lasers.llnl.gov/.

[35] M Roth, TE Cowan, MH Key, et al. Fast ignition by intense laser-accelerated proton beams. *Physical Review Letters*, 86(3):436–439, 2001.

[36] M Tabak, J Hammer, ME Glinsky, et al. Ignition and high-gain with ultrapowerful lasers. *Physics of Plasmas*, 1(5, Part 2):1626–1634, 1994.

[37] M. H. Key. Status of and prospects for the fast ignition inertial fusion concept. *Physics of Plasmas*, 14(5), 2007.

[38] J. J. Honrubia, J. C. Fernandez, M. Temporal, B. M. Hegelich, and J. Meyer-ter Vehn. Fast ignition of inertial fusion targets by laser-driven carbon beams. *Physics of Plasmas*, 16(10), 2009.

[39] P. R. Bolton, T. Hori, H. Kiriyama, et al. Toward integrated laser-driven ion accelerator systems at the photo-medical research center in Japan. *Nuclear Instruments & Methods in Physics Research Section A*, 620(1, SI):71–75, 2010.

[40] F Pegoraro, S Atzeni, M Borghesi, et al. Production of ion beams in high-power laser-plasma interactions and their applications. *Laser and Particle Beams*, 22(1):19–24, 2004.

[41] T.J.M Boyd and Sanderson J.J. *The physics of plasmas*. Cambridge University Press, Cambridge, 2003.

[42] P. Gibbon. *Short pulse laser interactions with matter: an introduction*. Imperial College Press, London, 2005.

[43] M Protopapas, C H Keitel, and P L Knight. Atomic physics with super-high intensity lasers. *Reports on Progress in Physics*, 60(4):389, 1997.

[44] AI Akhiezer and RV Polovin. Theory of wave motion of an electron plasma. *Soviet Physics JETP*, 3, 1956.

[45] F Brunel. Not-so-resonant, resonant absorption. *Physical Review Letters*, 59(1):52–55, JUL 6 1987.

[46] P. Gibbon and A. R. Bell. Collisionless absorption in sharp-edged plasmas. *Physical Review Letters*, 68:1535–1538, Mar 1992.

[47] SC Wilks, WL Kruer, M Tabak, and AB Langdon. Absorption of ultra-intense laser-pulses. *Physical Review Letters*, 69(9):1383–1386, AUG 31 1992.

[48] E. L. Clark, K. Krushelnick, J. R. Davies, et al. Measurements of energetic proton transport through magnetized plasma from intense laser interactions with solids. *Physical Review Letters*, 84:670–673, Jan 2000.

[49] Y Murakami, Y Kitagawa, Y Sentoku, et al. Observation of proton rear emission and possible gigagauss scale magnetic fields from ultra-intense laser illuminated plastic target. *Physics of Plasmas*, 8(9):4138–4143, 2001.

[50] E. L. Clark, K. Krushelnick, M. Zepf, et al. Energetic heavy-ion and proton generation from ultraintense laser-plasma interactions with solids. *Physical Review Letters*, 85:1654–1657, Aug 2000.

[51] I. Spencer, K. W. D. Ledingham, P. McKenna, et al. Experimental study of proton emission from 60-fs, 200-mj high-repetition-rate tabletop-laser pulses interacting with solid targets. *Physical Review E*, 67:046402, Apr 2003.

[52] A. J. Mackinnon, M. Borghesi, S. Hatchett, et al. Effect of plasma scale length on multi-mev proton production by intense laser pulses. *Physical Review Letters*, 86:1769–1772, Feb 2001.

[53] Stephen P. Hatchett, Curtis G. Brown, Thomas E. Cowan, et al. Electron, photon, and ion beams from the relativistic interaction of petawatt laser pulses with solid targets. *Physics of Plasmas*, 7(5):2076–2082, 2000.

[54] M. Zepf, E. L. Clark, K. Krushelnick, et al. Fast particle generation and energy transport in laser-solid interactions. *Physics of Plasmas*, 8(5):2323–2330, 2001.

[55] P. McKenna, K. W. D. Ledingham, J. M. Yang, et al. Characterization of proton and heavier ion acceleration in ultrahigh-intensity laser interactions with heated target foils. *Physical Review E*, 70:036405, Sep 2004.

[56] J. Fuchs, Y. Sentoku, S. Karsch, et al. Comparison of laser ion acceleration from the front and rear surfaces of thin foils. *Physical Review Letters*, 94:045004, 2005.

[57] A. J. Mackinnon, Y. Sentoku, P. K. Patel, et al. Enhancement of proton acceleration by hot-electron recirculation in thin foils irradiated by ultraintense laser pulses. *Physical Review Letters*, 88:215006, 2002.

[58] A. Fukumi, M. Nishiuchi, H. Daido, et al. Laser polarization dependence of proton emission from a thin foil target irradiated by a 70 fs, intense laser pulse. *Physics of Plasmas*, 12(10):100701, 2005.

[59] T. Ceccotti, A. Lévy, H. Popescu, et al. Proton acceleration with high-intensity ultrahigh-contrast laser pulses. *Physical Review Letters*, 99:185002, 2007.

[60] Matthew Allen, Pravesh K. Patel, Andrew Mackinnon, et al. Direct experimental evidence of back-surface ion acceleration from laser-irradiated gold foils. *Physical Review Letters*, 93:265004, 2004.

[61] A. Maksimchuk, S. Gu, K. Flippo, D. Umstadter, and V. Yu. Bychenkov. Forward ion acceleration in thin films driven by a high-intensity laser. *Physical Review Letters*, 84:4108–4111, 2000.

[62] L. M. Wickens, J. E. Allen, and P. T. Rumsby. Ion emission from laser-produced plasmas with two electron temperatures. *Physical Review Letters*, 41:243–246, 1978.

[63] K Krushelnick, E L Clark, F N Beg, et al. High intensity laser-plasma sources of ions - physics and future applications. *Plasma Physics and Controlled Fusion*, 47(12B):B451, 2005.

[64] M Borghesi, A Bigongiari, S Kar, et al. Laser-driven proton acceleration: source optimization and radiographic applications. *Plasma Physics and Controlled Fusion*, 50(12):124040, 2008.

[65] L. Robson, P. T. Simpson, R. J. Clarke, et al. Scaling of proton acceleration driven by petawatt-laser-plasma interactions. *Nature Physics*, 3:58–62, 2007.

[66] K Zeil, S D Kraft, S Bock, et al. The scaling of proton energies in ultrashort pulse laser plasma acceleration. *New Journal of Physics*, 12(4):045015, 2010.

[67] Y. Oishi, T. Nayuki, T. Fujii, et al. Dependence on laser intensity and pulse duration in proton acceleration by irradiation of ultrashort laser pulses on a cu foil target. *Physics of Plasmas*, 12(7):073102, 2005.

[68] A. Flacco, F. Sylla, M. Veltcheva, et al. Dependence on pulse duration and foil thickness in high-contrast-laser proton acceleration. *Physical Review E*, 81:036405, Mar 2010.

[69] G.M. Petrov and J. Davis. Laser acceleration of light ions from high-intensity laser-target interactions. *Applied Physics B*, 96:773 – 779, 2009.

[70] M. Kaluza, J. Schreiber, M. I. K. Santala, et al. Influence of the laser prepulse on proton acceleration in thin-foil experiments. *Physical Review Letters*, 93:045003, 2004.

[71] F. N. Beg, M. S. Wei, A. E. Dangor, et al. Target charging effects on proton acceleration during high-intensity short-pulse laser-solid interactions. *Applied Physics Letters*, 84(15):2766–2768, 2004.

[72] J. Fuchs, T. E. Cowan, P. Audebert, et al. Spatial uniformity of laser-accelerated ultrahigh-current mev electron propagation in metals and insulators. *Physical Review Letters*, 91:255002, 2003.

[73] A. Henig, D. Kiefer, K. Markey, et al. Enhanced laser-driven ion acceleration in the relativistic transparency regime. *Physical Review Letters*, 103:045002, 2009.

[74] L. Willingale, S. R. Nagel, A. G. R. Thomas, et al. Characterization of high-intensity laser propagation in the relativistic transparent regime through measurements of energetic proton beams. *Physical Review Letters*, 102:125002, 2009.

[75] S. Buffechoux, J. Psikal, M. Nakatsutsumi, et al. Hot electrons transverse refluxing in ultraintense laser-solid interactions. *Physical Review Letters*, 105:015005, 2010.

[76] S. C. Wilks, A. B. Langdon, T. E. Cowan, et al. Energetic proton generation in ultra-intense laser–solid interactions. *Physics of Plasmas*, 8(2):542–549, 2001.

[77] D. Batani, J. R. Davies, A. Bernardinello, et al. Explanations for the observed increase in fast electron penetration in laser shock compressed materials. *Physical Review E*, 61:5725–5733, 2000.

[78] T. Grismayer and P. Mora. Influence of a finite initial ion density gradient on plasma expansion into a vacuum. *Physics of Plasmas*, 13(3):032103, 2006.

[79] T. Esirkepov, M. Borghesi, S. V. Bulanov, G. Mourou, and T. Tajima. Highly efficient relativistic-ion generation in the laser-piston regime. *Physical Review Letters*, 92:175003, 2004.

[80] T. Esirkepov, M. Yamagiwa, and T. Tajima. Laser ion-acceleration scaling laws seen in multiparametric particle-in-cell simulations. *Physical Review Letters*, 96:105001, 2006.

[81] Andrea Macchi, Federica Cattani, Tatiana V. Liseykina, and Fulvio Cornolti. Laser acceleration of ion bunches at the front surface of overdense plasmas. *Physical Review Letters*, 94:165003, 2005.

[82] Andrea Macchi, Tatiana V. Liseikina, Sara Tuveri, and Silvia Veghini. Theory and simulation of ion acceleration with circularly polarized laser pulses. *Comptes Rendus Physique*, 10:207 – 215, 2009.

[83] A P L Robinson, P Gibbon, M Zepf, et al. Relativistically correct hole-boring and ion acceleration by circularly polarized laser pulses. *Plasma Physics and Controlled Fusion*, 51(2):024004, 2009.

[84] G. Marx. Interstellar vehicle propelled by terrestrial laser beam. *Nature*, 211:22–23, 1966.

[85] A. Henig, S. Steinke, M. Schnürer, et al. Radiation-pressure acceleration of ion beams driven by circularly polarized laser pulses. *Physical Review Letters*, 103:245003, Dec 2009.

[86] Charlotte A. J. Palmer, N. P. Dover, I. Pogorelsky, et al. Monoenergetic proton beams accelerated by a radiation pressure driven shock. *Physical Review Letters*, 106:014801, Jan 2011.

[87] C.K. Birdsall and A.B. Langdon. *Plasma physics via computer simulation*. McGraw-Hill, New York, 1985.

[88] Claudio Perego, Alessandro Zani, Dimitri Batani, and Matteo Passoni. Extensive comparison among target normal sheath acceleration theoretical models. *Nuclear Instruments and Methods in Physics Research Section A*, 653(1):89 – 93, 2011.

[89] C. Perego, D. Batani, A. Zani, and M. Passoni. Target normal sheath acceleration analytical modeling, comparative study and developments. *Review of Scientific Instruments*, 83(2):02B502, 2012.

[90] P. Mora. Plasma expansion into a vacuum. *Physical Review Letters*, 90:185002, May 2003.

[91] J Fuchs, P. Antici, E. d/'Humieres, et al. Laser-driven proton scaling laws and new paths towards energy increase. *Nature Physics*, 2:48–54, 2006.

[92] P. Antici. *Energetic protons generated by ultrahigh contrast laser pulses interacting with ultra-thin targets*. PhD thesis, Università La Sapienza, Rome, 2007.

[93] P. Mora. Thin-foil expansion into a vacuum. *Physical Review E*, 72:056401, Nov 2005.

[94] S Betti, F Ceccherini, F Cornolti, and F Pegoraro. Expansion of a finite-size plasma in vacuum. *Plasma Physics and Controlled Fusion*, 47(3):521, 2005.

[95] J. Schreiber, F. Bell, F. Grüner, et al. Analytical model for ion acceleration by high-intensity laser pulses. *Physical Review Letters*, 97:045005, Jul 2006.

[96] M. Passoni and M. Lontano. Theory of light-ion acceleration driven by a strong charge separation. *Physical Review Letters*, 101:115001, Sep 2008.

[97] S. Kar, M. Borghesi, S. V. Bulanov, et al. Plasma jets driven by ultraintense-laser interaction with thin foils. *Physical Review Letters*, 100:225004, Jun 2008.

[98] K. Quinn, P. A. Wilson, C. A. Cecchetti, et al. Laser-driven ultrafast field propagation on solid surfaces. *Physical Review Letters*, 102:194801, May 2009.

[99] Maurizio Lontano and Matteo Passoni. Electrostatic field distribution at the sharp interface between high density matter and vacuum. *Physics of Plasmas*, 13(4):042102, 2006.

[100] B. J. Albright, L. Yin, B. M. Hegelich, et al. Theory of laser acceleration of light-ion beams from interaction of ultrahigh-intensity lasers with layered targets. *Physical Review Letters*, 97:115002, Sep 2006.

[101] A. P. L Robinson, A. R. Bell, and R. J. Kingham. Effect of target composition on proton energy spectra in ultraintense laser-solid interactions. *Physical Reiew Letters*, 96:035005, Jan 2006.

[102] J. Yu, Z. Jiang, J. C. Kieffer, and A. Krol. Hard x-ray emission in high intensity femtosecond laser–target interaction. *Physics of Plasmas*, 6(4):1318–1322, 1999.

[103] M. Roth, A. Blazevic, M. Geissel, et al. Energetic ions generated by laser pulses: A detailed study on target properties. *Physical Review Special Topics Accelators and Beams*, 5:061301, 2002.

[104] M. Nishiuchi, H. Daido, A. Yogo, et al. Efficient production of a collimated mev proton beam from a polyimide target driven by an intense femtosecond laser pulse. *Physics of Plasmas*, 15(5):053104, 2008.

[105] S. Fritzler, V. Malka, G. Grillon, et al. Proton beams generated with high-intensity lasers: Applications to medical isotope production. *Applied Physics Letters*, 83(15):3039–3041, 2003.

[106] M. Nishiuchi, A. Fukumi, H. Daido, et al. The laser proton acceleration in the strong charge separation regime. *Physics Letters A*, 357(4-5):339 – 344, 2006.

[107] Takashi Fujii, Yuji Oishi, Takuya Nayuki, et al. Mev-order proton and carbon ion acceleration by irradiation of 60 fs tw laser pulses on thin copper tape. *Applied Physics Letters*, 83(8):1524–1526, 2003.

[108] M. Borghesi, T. Toncian, J. Fuchs, et al. Laser-driven proton acceleration and applications: Recent results. *The European Physical Journal Special Topics*, 175:105–110, 2009.

[109] Julien Fuchs, Patrick Audebert, Marco Borghesi, Henri Papin, and Oswald Willi. Laser acceleration of low emittance, high energy ions and applications. *Comptes Rendus Physique*, 10(2-3):176 – 187, 2009.

[110] D. I. Dzavakhishvili and N. L. Tsintsadze. Transport phenomena in a completely ionized ultrarelativistic plasma. *Zhurnal Eksperimentalnoi i Teoreticheskoi Fiziki*, 64:1314–1325, 1973.

[111] J. S. Green, V. M. Ovchinnikov, R. G. Evans, et al. Effect of laser intensity on fast-electron-beam divergence in solid-density plasmas. *Physical Review Letters*, 100:015003, Jan 2008.

[112] M. Passoni, V. T. Tikhonchuk, M. Lontano, and V. Yu. Bychenkov. Charge separation effects in solid targets and ion acceleration with a two-temperature electron distribution. *Physical Review E*, 69:026411, Feb 2004.

[113] C. Cercignani and G.M. Kremer. *The relativistic Boltzmann equation: theory and applications*, volume 22 of *Progress in mathematical physics*. Birkhäuser Verlag, Basel-Boston-Berlin, 2002.

[114] M. Passoni, L. Bertagna, and A. Zani. Target normal sheath acceleration: theory, comparison with experiments and future perspectives. *New Journal of Physics*, 12(4):045012, 2010.

[115] A. Zani. Master's thesis, Politecnico di Milano, Italy, 2009.

[116] M. Passoni, L. Bertagna, T. Ceccotti, and P. Martin. Proton maximum energy cutoff scaling laws for bulk targets. *AIP Conference Proceedings*, 1153(1):159–163, 2009.

[117] M. Borghesi, J. Fuchs, S.V. Bulanov, et al. Fast ion generation by high-intensity laser irradiation of solid targets and applications. *Fusion Science And Technology*, 49:412–439, 2006.

[118] A. Zani, A. Sgattoni, and M. Passoni. Parametric investigations of target normal sheath acceleration experiments. *Nuclear Instruments and Methods in Physics Research Section A*, 653(1):94 – 97, 2011.

[119] C. Benedetti, A. Sgattoni, G. Turchetti, and P. Londrillo. Aladyn: A high-accuracy pic code for the maxwell-vlasov equations. *IEEE transactions on plasma science*, 36(4):1790–1798, 2008.

[120] C. Benedetti, P. Londrillo, V. Petrillo, et al. Pic simulations of the production of high-quality electron beams via laser–plasma interaction. *Nuclear Instruments and Methods in Physics Research Section A*, 608(1):S94–S98, 2009.

[121] P. Londrillo, C. Benedetti, A. Sgattoni, and G. Turchetti. Charge preserving high order pic schemes. *Nuclear Instruments and Methods in Physics Research Section A: Accelerators*, 620(1):28 – 35, 2010.

[122] L. Willingale, S. P. D. Mangles, P. M. Nilson, et al. Collimated multi-mev ion beams from high-intensity laser interactions with underdense plasma. *Physical Review Letters*, 96:245002, Jun 2006.

[123] S. V. Bulanov and T. Zh. Esirkepov. Comment on "collimated multi-mev ion beams from high-intensity laser interactions with underdense plasma". *Physical Review Letters*, 98:049503, Jan 2007.

[124] Stepan S. Bulanov, Valery Yu, Vladimir Chvykov, et al. Generation of GeV protons from 1 PW laser interaction with near critical density targets. *Physics of Plasmas*, 17(4):043105, 2010.

[125] A. Yogo, H. Daido, S. V. Bulanov, et al. Laser ion acceleration via control of the near-critical density target. *Physical Review E*, 77:016401, Jan 2008.

[126] D. Jung, L. Yin, B. J. Albright, et al. Monoenergetic ion beam generation by driving ion solitary waves with circularly polarized laser light. *Physical Review Letters*, 107:115002, Sep 2011.

[127] L. Willingale, P. M. Nilson, A. G. R. Thomas, et al. High-power, kilojoule laser interactions with near-critical density plasma. *Physics of Plasmas*, 18(5):056706, may 2011.

[128] Y. T. Li, Z. M. Sheng, Y. Y. Ma, et al. Demonstration of bulk acceleration of ions in ultraintense laser interactions with low-density foams. *Physical Review E*, 72:066404, Dec 2005.

[129] Tatsufumi Nakamura, Motonobu Tampo, Rryosuke Kodama, Sergei V. Bulanov, and Masaki Kando. Interaction of high contrast laser pulse with foam-attached target. *Physics of Plasmas*, 17(11):113107, 2010.

[130] A. Sgattoni, P. Londrillo, A. Macchi, and M. Passoni. Laser ion acceleration using a solid target coupled with a low-density layer. *Physical Review E*, 85:036405, Mar 2012.

[131] http://www.suldis.org.

[132] S. A. Gaillard, T. Kluge, K. A. Flippo, et al. Increased laser-accelerated proton energies via direct laser-light-pressure acceleration of electrons in microcone targets. *Physics of Plasmas*, 18(5), 2011.

[133] HY Wang, XQ Yan, JE Chen, et al. Efficient and stable proton acceleration by irradiating a two-layer target with a linearly polarized laser pulse. *Physics of Plasmas*, 20:013101, 2013.

[134] M. J. Burchell, G. Graham, and A. Kearsley. Cosmic Dust Collection in Aerogel. *Annual Review of Earth and Planetary Sciences*, 34:385–418, May 2006.

[135] María J. López, Iván Cabria, and Julio A. Alonso. Simulated porosity and electronic structure of nanoporous carbons. *The Journal of Chemical Physics*, 135(10):104706, 2011.

[136] LJ Gibson and MF. Ashby. *Cellular solids: structure and properties*. Cambridge University Press, London, 2nd edition, 1997.

[137] M. P. Siegal, D. L. Overmyer, R. J. Kottenstette, D. R. Tallant, and W. G. Yelton. Nanoporous-carbon films for microsensor preconcentrators. *Applied Physics Letters*, 80(21):3940–3942, 2002.

[138] Gursel Turgut, Ayhan Eksilioglu, Nagehan Gencay, et al. Pore structure engineering for carbon foams as possible bone implant material. *Journal of Biomedical Materials Research Part A*, 85A(3):588–596, 2008.

[139] Yoon Sung Nam, Jun Jin Yoon, and Tae Gwan Park. A novel fabrication method of macroporous biodegradable polymer scaffolds using gas foaming salt as a porogen additive. *Journal of Biomedical Materials Research*, 53:1–7, 2000.

[140] Qing wu Zhang, Xiao Zhou, and Hong sheng Yang. Capacitance properties of composite electrodes prepared by electrochemical polymerization of pyrrole on carbon foam in aqueous solution. *Journal of Power Sources*, 125(1):141 – 147, 2004.

[141] F. Moglie, D. Micheli, S. Laurenzi, M. Marchetti, and V. Mariani Primiani. Electromagnetic shielding performance of carbon foams. *Carbon*, 50(5):1972 – 1980, 2012.

[142] A. Zani, D. Dellasega, V. Russo, and M. Passoni. Ultra-low density carbon foams produced by pulsed laser deposition. *Carbon*, (in press):–, 2013.

[143] Vladlen G. Shvedov, Andrei V. Rode, Yana V. Izdebskaya, et al. Giant optical manipulation. *Physical Review Letters*, 105:118103, Sep 2010.

[144] A. V. Rode, E. G. Gamaly, A. G. Christy, et al. Unconventional magnetism in all-carbon nanofoam. *Physical Review B*, 70:054407, Aug 2004.

[145] D. Arčon, Z. Jagličič, A. Zorko, et al. Origin of magnetic moments in carbon nanofoam. *Physical Review B*, 74:014438, Jul 2006.

[146] Qin Yue, Yuanzhi Li, Ming Kong, et al. Ultralow density, hollow silica foams produced through interfacial reaction and their exceptional properties for environmental and energy applications. *J. Mater. Chem.*, 21:12041–12046, 2011.

[147] Aurelio Salerno, Salvatore Iannace, and Paolo A. Netti. Open-pore biodegradable foams prepared via gas foaming and microparticulate templating. *Macromolecular Bioscience*, 8(7):655–664, 2008.

[148] Leon J. M. Jacobs, Stan A. M. Hurkens, Maartje F. Kemmere, and Jos T. F. Keurentjes. Porous cellulose acetate butyrate foams with a tunable bimodality in foam morphology produced with supercritical carbon dioxide. *Macromolecular Materials and Engineering*, 293(4):298–302, 2008.

[149] R. Narasimman and K. Prabhakaran. Preparation of low density carbon foams by foaming molten sucrose using an aluminium nitrate blowing agent. *Carbon*, 50(5):1999 – 2009, 2012.

[150] R. Fu, B. Zheng, J. Liu, et al. The fabrication and characterization of carbon aerogels by gelation and supercritical drying in isopropanol. *Advanced Functional Materials*, 13(7):558–562, 2003.

[151] Xiao-Hong Chen, Shuang-Xi Yang, and Huai-He Song. Preparation and characterization of RF/SiO2 hybrid aerogel by sol-gel method. 11-12:619–622, 2006. Asian International Conference on Advanced Materials, Beijing, PEOPLES R CHINA, NOV 03-05, 2005.

[152] J. W. Falconer, W. Nazarov, and C. J. Horsfield. In situ production of very low density microporous polymeric foams. *Journal of Vacuum Science Technology A: Vacuum, Surfaces, and Films*, 13(4):1941 –1944, jul 1995.

[153] EG Gamaly and AV Rode. Nanostructures created by lasers. *Encyclopedia of Nanoscience and Nanotechnology*, 7(1):783–809, 2004.

[154] L. El Mir, S. Kraiem, M. Bengagi, et al. Synthesis and characterization of electrical conducting nanoporous carbon structures. *Physica B: Condensed Matter*, 395(1-2):104 – 110, 2007.

[155] A.V. Rode, S.T. Hyde, E.G. Gamaly, et al. Structural analysis of a carbon foam formed by high pulse-rate laser ablation. *Applied Physics A*, 69:S755–S758, 1999.

[156] David L. Pappas, Katherine L. Saenger, John Bruley, et al. Pulsed laser deposition of diamond-like carbon films. *Journal of Applied Physics*, 71(11):5675 –5684, jun 1992.

[157] A.A. Voevodin and M.S. Donley. Preparation of amorphous diamond-like carbon by pulsed laser deposition: a critical review. *Surface and Coatings Technology*, 82(3):199 – 213, 1996.

[158] M. P. Siegal, D. R. Tallant, L. J. Martinez-Miranda, et al. Nanostructural characterization of amorphous diamondlike carbon films. *Physical Review B*, 61:10451–10462, Apr 2000.

[159] M. Bonelli, A.C. Ferrari, A. Fioravanti, et al. Structure and mechanical properties of low stress tetrahedral amorphous carbon films prepared by pulsed laser deposition. *The European Physical Journal B - Condensed Matter and Complex Systems*, 25:269–280, 2002.

[160] M Rusop, T Soga, T Jimbo, and M Umeno. Physical and structural properties of carbon thin films deposited in two inert gases ambient by pulsed laser ablation using camphoric carbon target. *Applied Surface Science*, 197–198(0):426 – 431, 2002. ¡ce:title¿COLA'01 SI¡/ce:title¿.

[161] S. J. Henley, J. D. Carey, and S. R. P. Silva. Room temperature photoluminescence from nanostructured amorphous carbon. *Applied Physics Letters*, 85(25):6236–6238, 2004.

[162] S.J. Henley, S.R.P. Silva, and J.D. Carey. Surface morphology and evolution of amorphous carbon thin films. *Diamond and Related Materials*, 16(10):1777 – 1781, 2007. ¡ce:title¿Proceedings of the 6th Specialists Meeting in Amorphous Carbon¡/ce:title¿.

[163] Zs. Geretovszky, T. Haraszti, T. Szörènyic, F. Antoni, and E. Fogarassy. Morphological study of pld grown carbon films. *Applied Surface Science*, 208–209:566 – 574, 2003. ¡ce:title¿Physics and Chemistry of Advanced Laser Materials Processing¡/ce:title¿.

[164] P.M. Ossi, C.E. Bottani, and A. Miotello. Pulsed-laser deposition of carbon: from dlc to cluster-assembled films. *Thin Solid Films*, 482(1–2):2 – 8, 2005. ¡ce:title¿EMRS 2004, Symposium J¡/ce:title¿ ¡xocs:full-name¿Proceedings of Symposium J on Synthesis, Characterisation and Advanced Applications of Amorphous Carbon Films, EMRS 2004 Conference¡/xocs:full-name¿.

[165] A.V. Rode, E.G. Gamaly, and B. Luther-Davies. Formation of cluster-assembled carbon nano-foam by high-repetition-rate laser ablation. *Applied Physics A*, 70:135–144, 2000.

[166] E.G. Gamaly, A.V. Rode, and B. Luther-Davies. Formation of diamond-like carbon films and carbon foam by ultrafast laser ablation. *Laser and Particle Beams*, 18:245–254, 3 2000.

[167] J. G. Miller and D. I. Bolef. Acoustic wave analysis of the operation of quartz-crystal film-thickness monitors. *Journal of Applied Physics*, 39(12):5815–5816, 1968.

[168] Chih-Shun Lu and Owen Lewis. Investigation of film-thickness determination by oscillating quartz resonators with large mass load. *Journal of Applied Physics*, 43(11):4385–4390, 1972.

[169] K. Keiji Kanazawa and Joseph G. Gordon. Frequency of a quartz microbalance in contact with liquid. *Analytical Chemistry*, 57(8):1770–1771, 1985.

[170] Yu. G. Lavrentev, V. N. Korolyuk, and L. V. Usova. Second generation of correction methods in electron probe x-ray microanalysis: Approximation models for emission depth distribution functions. *Journal of Analytical Chemistry*, 59(7):600–616, 2004.

[171] H E Bishop and D M Poole. A simple method of thin film analysis in the electron probe microanalyser. *Journal of Physics D: Applied Physics*, 6(9):1142, 1973.

[172] G. Stenberg and M. Boman. Thickness measurement of light elemental films. *Diamond and Related Materials*, 5(12):1444 – 1449, 1996.

[173] M.D. Bentzon, P.S. Nielsen, and S.S. Eskildsen. A simple and sensitive way to determine carbon film thickness. *Diamond and Related Materials*, 2(5–7):893 – 897, 1993. ¡ce:title¿Diamond 1992 ¡/ce:title¿.

[174] J. Robertson. Diamond-like amorphous carbon. *Materials Science and Engineering: R: Reports*, 37(4–6):129 – 281, 2002.

[175] A. C. Ferrari and J. Robertson. Interpretation of raman spectra of disordered and amorphous carbon. *Physical Review B*, 61:14095–14107, May 2000.

[176] E. G. Gamaly, N. R. Madsen, D. Golberg, and A. V. Rode. Expansion-limited aggregation of nanoclusters in a single-pulse laser-produced plume. *Physical Review B*, 80:184113, Nov 2009.

[177] Ming Y. Chen and P. Terrence Murray. Carbon nitride thin-film growth by pulsed laser deposition. *Journal of Vacuum Science & Technology A: Vacuum, Surfaces, and Films*, 16(4):2093–2098, 1998.

[178] YM Koo, YK Choi, KH Lee, and KW Jung. Mass spectrometric study of carbon cluster formation in laser ablation of graphite at 355 nm. *Bullettin of the Korean Chemical Society*, 23(2):309–314, FEB 20 2002.

[179] P.M. Ossi and A. Bailini. Effect of ambient gas ionisation on the morphology of a pulsed laser deposited carbon film. *Carbon*, 44(14):3049 – 3052, 2006.

[180] C. S. Casari, A. Li Bassi, L. Ravagnan, et al. Chemical and thermal stability of carbyne-like structures in cluster-assembled carbon films. *Physical Review B*, 69:075422, Feb 2004.

[181] D. Dellasega, A. Facibeni, F. Di Fonzo, et al. Nanostructured high valence silver oxide produced by pulsed laser deposition. *Applied Surface Science*, 255(10):5248 – 5251, 2009.

[182] Salvatore Amoruso, Riccardo Bruzzese, Nicola Spinelli, et al. Dynamics of laser-ablated mgb_2 plasma expanding in argon probed by optical emission spectroscopy. *Physical Review B*, 67:224503, Jun 2003.

[183] Hye Sun Park, Sang Hwan Nam, and Seung Min Park. Time-resolved optical emission studies on the laser ablation of a graphite target: The effects of ambient gases. *Journal of Applied Physics*, 97(11):113103, 2005.

[184] http://www.laserlab-europe.net.

[185] Salvatore Amoruso, Bo Toftmann, and Jørgen Schou. Thermalization of a uv laser ablation plume in a background gas: From a directed to a diffusionlike flow. *Physical Review E*, 69:056403, May 2004.